Universidade de Santiago de Compostela
Departamento de Física de Partículas

PRODUCTION AND β DECAY HALF-LIVES OF HEAVY NEUTRON-RICH NUCLEI APPROACHING THE STELLAR NUCLEOSYNTHESIS R-PROCESS PATH AROUND A=195

Teresa Kurtukian Nieto
under the supervision of
José Benlliure Anaya

January 2007

UNIVERSIDADE DE SANTIAGO DE COMPOSTELA

FACULTAD DE FÍSICA

DEPARTAMENTO DE FÍSICA DE PARTÍCULAS

Production and β decay half-lives of heavy neutron-rich nuclei approaching the stellar nucleosynthesis r-process path around A=195

Memoria presentada por:
Teresa Kurtukian Nieto
como requisito para optar al
Título de Doctor
Ph.D. Thesis

18 de Enero 2007

José F. Benlliure Anaya, Profesor Titular
de la **Universidad de Santiago de Compostela**,

CERTIFICO: que la memoria titulada **Production and β decay half-lives of heavy neutron-rich nuclei approaching the stellar nucleosynthesis r-process path around A=195**, ha sido realizada por **Teresa Kurtukian Nieto** bajo mi dirección en el **Departamento de Física de Partículas** de esta Universidad, y constituye la Tesis que presenta para optar al grado de **Doctor en Física**.

Santiago de Compostela, 18 de enero de 2007

Prof. José F. Benlliure Anaya **Teresa Kurtukian Nieto**

The examination board was composed by:

Dr. Karl-Heinz Schmidt (President)
Gesellschaft für Schwerionenforschung (GSI), Darmstadt, Germany
Prof. Dr. Karlheinz Langanke
Gesellschaft für Schwerionenforschung (GSI), Darmstadt, Germany
Prof. Dr. Betram Blank
Centre d'Etudes Nucléaires de Bordeaux-Gradignan, France
Dra. María José García Borge
Instituto Estructura de la Materia CSIC, Madrid, Spain
Prof. Dr. Ignacio Durán Escribano
Universidad de Santiago de Compostela, Spain

Understanding the universe is a fascinating challenge. We can not understand the universe without understanding the nucleus. This dissertation represents my two cents.

A mi madre, Maria, y a la memoria de mi padre, Shavarsh

"Quiero hacerme sabio pero la sabiduría
está lejos de mi. Lejos se queda
lo que estaba lejos, y profundo,
lo profundo. ¿Quién lo alcanzará?."
Eclesiastés 7: 23-27

Contents

List of Figures

List of Tables

Introduction

One of the major challenges of nuclear astrophysics is to explain how the heavy elements are created in the Universe. The rapid neutron-capture process (r-process) [1,2] of nucleosynthesis is thought to be responsible for the creation of half of the elements heavier than iron.

Starting with a seed nucleus, neutron-rich nuclides are produced via a series of neutron captures until a point is reached where an equilibrium is established between the neutron-capture and photo-disintegration reactions. Here, the r-process essentially stalls until this "waiting-point" nucleus undergoes a β-decay, and the capture of neutrons can then continue until another equilibrium is established. Once neutron-capture ceases, the unstable nuclides β-decay towards the valley of stability, forming the r-process nuclei.

Already in 1957, Burdbidge et al. [1] pointed out that the r-process passes through neutron-magic nuclei around A $\simeq$ 80, 130 and 195 which have longer-than-average β-decay half-lives. Besides this basic understanding, the astrophysical scenarios in which an r-process may occur are still matter of debate, due to the high density of free neutrons required per seed nucleus to run this process through far-unstable nuclei, such as $^{80}Zn_{50}$, $^{130}Cd_{82}$ and $^{195}Tm_{126}$, up to the heaviest elements in nature. The main candidate environments of this process are neutrino-heated ejecta from core-collapse supernovae [3–6] and decompressed ejecta from neutron star mergers [7–9] which may provide the required conditions.

Experimental studies of very neutron-rich nuclides lying in and near the r-process path provide direct data for use in r-process nucleosynthesis calculations and to test current theories from which nuclear properties of far-unstable isotopes are derived [10].

In the mid-80's, the area of experiments *in the r-process path* started with the identification of the first two classical, neutron-magic "waiting-point" isotopes: $^{80}Zn_{50}$, situated 10 mass units away

from stability, at the fission-product mass separators OSIRIS [11] and TRISTAN [12] and $^{130}Cd_{82}$, 16 units below the stable isotope ^{114}Cd, at CERN/ISOLDE [13].

This success strongly motivated further experimental and theoretical nuclear-structure investigations, as well as astrophysical r-process studies [14]. Nevertheless, even today, the vast majority of very neutron-rich r-process nuclei is not experimentally accessible, and in particular, the waiting-point around N=126, in the heavy neutron-rich region, remain as an unexplored territory [15]. Therefore, a general understanding of their nuclear properties remains to be obtained only through theoretical models. However, the possibility of accelerating heavy ions at relativistic energies made it possible to investigate, during the last years, reaction mechanisms leading to the production of heavy neutron-rich nuclei, such as cold-fragmentation reactions [16].

The interpretation of the observed r-process abundances requires detailed knowledge on the structure and gross properties of the involved nuclei. In particular masses, β half-lives and neutron-capture cross-sections are relevant. In this work, we concentrate on the measurement of β half-lives of heavy neutron-rich nuclei, close to the neutron closed shell N=126. β-decay half-lives are of interest not only because they play an important role in the understanding of the progress and time scale of the stellar nucleosynthesis processes, and consequently in the final abundance patterns, but also because they can be used to benchmark nuclear models far from stability.

The experimental data shown in the present dissertation corresponds to an experiment performed in 2003 at the Gesellschaft für Schwerionenforschung (GSI), located in Darmstadt, Germany, in collaboration with the Institute de Physique Nuclèaire IPN (Orsay, France), Centre d'Etudes Nuclèaires de Bordeaux Gradignan CENBG (Bordeaux, France), Grand Accélérateur National d'Ions Lourds GANIL (Caen, France), and Universidad de Santiago de Compostela USC (Santiago de Compostela, Spain). The aim of this work is to explore the production and β-decay half-lives of heavy neutron-rich nuclei approaching the "waiting-point" A=195. The beam used was ^{208}Pb at 1 A GeV impinging on a beryllium target. When using a ^{208}Pb beam, the cold-fragmentation reaction mechanism allows to produce heavy neutron-rich nuclei along the closed shell N=126.

The GSI Fragment Separator (FRS) [17] is a two-stage magnetic spectrometer that allows us to identify in-flight the isotopic species produced, by determining both the atomic number Z and the mass-over-charge ratio A/Z of each fragment passing through the FRS by measuring

their magnetic rigidities, time-of-flight (ToF) and energy loss. In order to separate different elements with enough resolution and to disentangle the different ionic charge states, the degrader energy-loss method [18] is used, which takes into account the difference in magnetic rigidity between the two sections of the FRS.

In order to measure the half-lives, the nuclei of interest were implanted into an active stopper. Half-lives were deduced from position-time correlations between the implanted fragments and the subsequent β-decays. The beam extracted from SIS [19] has a spill structure, with a typical spill length of 2 s and a repetition cycle of 10 s. Due to the pulsed structure of the beam, the rates of implantation and decay events were modulated with a periodic time structure. In addition, we had to face a beam-induced background contamination in the recorded decay curves, coming from the time structure of the previously implanted nuclei and δ or atomic electrons produced during the beam spill.

The very complex background conditions found in the present work cannot be easily modelled theoretically. We propose a new method to determine the β-decay half-lives by fitting the experimental data to a numerical function (rather than an analytical function), obtained from Monte-Carlo simulations of time correlations between implantations and β-like events, which allow us to evaluate and disentangle the background from the real decays.

The dissertation is organised as follows: Chapter 1 gives a general discussion about the nucleosynthesis of the heavy nuclei, the physics of the β-decay, the reaction mechanism that allows the production of such nuclei, and the experimental techniques to measure β-decay half-lives. Chapter 2 includes the description of the experimental setup and a detailed discussion of the identification procedure. Chapter 3 is dedicated to the production cross-sections. Chapter 4 shows the implantation technique and chapter 5 is dedicated to the determination of the β-decay half-lives. Finally, the main conclusions and perspectives of this work are presented.

Chapter 1

β-decay of heavy neutron-rich nuclei and the r-process

1.1 Nucleosynthesis of heavy elements: the r-process

In a compilation of data related to the mass abundances in the solar system and meteorites, Suess and Urey [20] observed for the first time the existence of double peaks in the abundance curve (see figure 1.1) at A = 80 and 90, 130 and 138, and at 195 and 208. Based on the shell model and the existence of the "magic numbers", proposed by M. Goeppert-Mayer and J. Jensen, W. Fowler had the idea of relating the existence of these peaks to the neutron shell closures at N = 50, 82 and 126.

In the very early evolution of the Universe, H, He, and traces of other light elements such as D and Li were created. When H condensed and formed stars, it ignited in thermo-nuclear fusion reactions which produce most of the energy radiated by stars. During their normal life-cycle, stars process their initial H as fuel toward heavier elements, starting with He and proceeding over all elements up to iron. The temperature is adjusted so that the outflow of energy through the star is balanced by nuclear energy generation. When the fuel becomes exhausted, the temperature rises until the next nuclear fuel comes into operation. The automatic temperature rise is brought about in each case by the conversion of gravitational energy into thermal energy [1].

Because iron lies at the peak of the curve of nuclear binding energy, the fusion process ends at iron and the star dies. The iron isotopes ^{56}Fe and

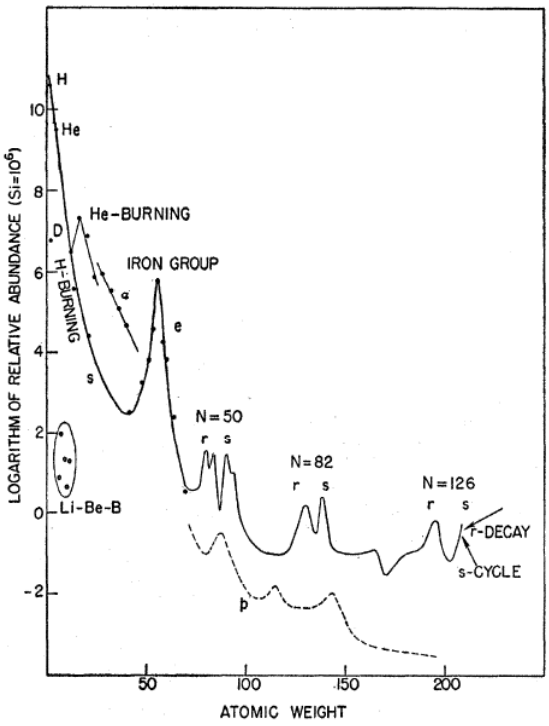

Figure 1.1: *Curve of atomic abundances in relation to the atomic weight based on the data of Suess and Urey, reported in [1]*

^{58}Fe, the most tightly bound nuclei of the chart of nuclides, represent the ashes of the fusion reactions. Beyond A $\approx$ 60 (in the Fe/Ni mass region), no further fusion processes can take place, due to the extremely high Coulomb barrier of involved nuclei and the endothermic character of the reactions. Therefore, the production of most heavier nuclei is mainly due to neutron-capture reactions, because neutrons do not suffer the Coulomb barrier, and therefore these mechanisms are not affected by it.

The existence of double peaks above A = 60 demonstrates that there are two regimens. They are known as the slow process of neutron capture (*s-process*) and the rapid neutron-capture process (*r-process*). These two processes differ in the neutron density. Typically the s-process takes place in environments with a density of 10^8 neutrons cm^{-3} while the r-process requires a density 10^{20} neutrons cm^{-3}, which represents a difference of 12 orders of magnitude.

In the s-process the neutron capture with the emission of gamma radiation (n, γ) takes place on a long time-scale, ranging from $\approx$ 100 years

to 10^5 years for each neutron capture [1]. The neutron captures occur at a slow rate compared to the intervening β-decays. The s-process produces the abundance peaks at A = 90, 128 and 208.

During the latter stages of a stars life the element formation occurs. Low-mass stars, similar to the Sun, which live for billions of years and end their lives as red giants and planetary nebulae are responsible for producing most of the s-process elements, which are then ejected into the interstellar medium as part of the dying stars [21].

In the r-process the neutron capture occurs in a very short time-scale, $\approx$ 0.01-10 s. Thus the neutron capture rate is rapid compared to the β-decays. An equilibrium is maintained in $(n,\gamma) \longleftrightarrow (\gamma,n)$ reactions. This equilibrium, referred to as *waiting-point approximation*, determines the abundances of different isotopes of the same element. The rate of nucleosynthesis is controlled by the β-decay rate. When the neutron flux is exhausted (referred to as freeze-out), the nuclei in the r-process path decay back to stability through a series of β-decays.

The abundance of nuclei present in the solar system related to the r-process is obtained by the natural abundance observed in our solar system, based on the s-process abundance pattern, following the work of Käppeler et al. [22]. It is fascinating that the r-process abundance pattern in very old stars, as can be seen in figure 1.2, is very similar to that of the solar system. This implies that there might be one dominant source for the r-process and that this source has not changed significantly over cosmic history.

Connecting the abundance maxima in the isotopic chains defines the so-called r-process path. From the observed r-process abundances peaks, the r-process path probably passes through the neutron closed shells N = 50, 82 and 126, at A $\approx$ 80, 130 and 195 (see figure 1.3). The so-called bottle-neck nuclei, which have particularly long half-lives, are typically located at shell closures where the sudden drop in the neutron separation energy makes photo-disintegration more favourable, while the capture process remains inhibited. Hence the abundances of these nuclei will build up as they "wait" to decay. The limit is attained when there is equilibrium between the reaction rates

$$ {}^{A}_{Z}X_N(n,\gamma)^{A+1}_{Z}Y_{N+1} \longleftrightarrow {}^{A+1}_{Z}Y_{N+1}(\gamma,n)^{A}_{Z}X_N \tag{1.1} $$

As a first approximation we can state that the knowledge of neutron separation energies (or equivalently nuclear masses) determines the r-process path, while the knowledge of β-decay half-lives determines the shape of the abundance curve [15, 25].

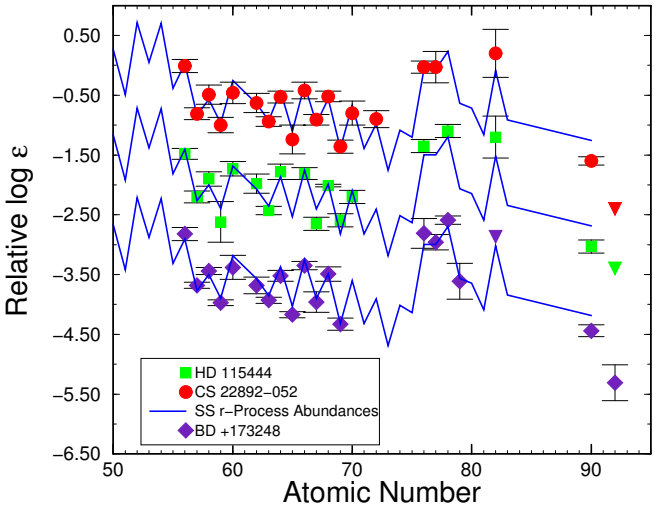

Figure 1.2: *Comparison of observed abundances in the three stars CS 22892-052, HD 115444 and BD +17° 3248 [23] with a solar system r-process elemental abundances. Upper limits are indicated by inverted triangles.*

Theoretical neutron separation energies calculated using a mass model that includes a quenching of shell gaps far from stability (Extended Thomas-Fermi approach + Strutinsky Integral, with shell quenching (ETFSI-Q) [26]), predict a smaller neutron separation energy for the most neutron-rich isotopes than the corresponding ones using the ETFSI-1 mass formula [27]. This reduction has an effect on the final abundance pattern, because the material that has been waiting to β-decay during the freeze-out would decay to different stable nuclides, depending on which mass model is used [24].

The r-process is one of the least understood nucleosynthesis processes because it involves extremely neutron-rich nuclei which are extremely difficult to study experimentally, if not impossible at present, and because it requires the most extreme astrophysical conditions. Any calculation on the r-process has to rely on theoretical models that are based on our knowledge of nuclear-structure properties of known nuclei. How nuclear-structure properties change from nuclei close to stability to extremely neutron-rich nuclei is not well understood.

Furthermore, the astrophysical scenarios in which an r-process may occur are still a matter of debate. Possible sites where the r-process may happen require a high density of free neutrons. The critical parameter that

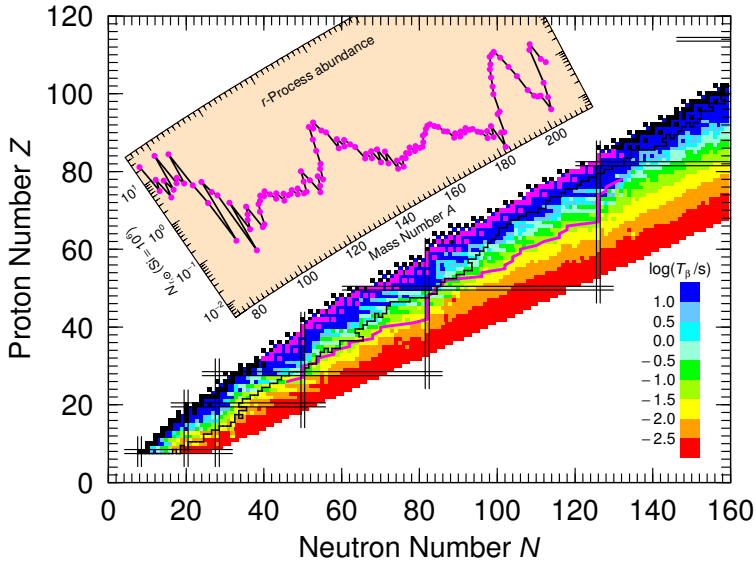

Figure 1.3: *Chart of nuclides taken from Ref [24]. The stable nuclides are marked by black boxes. The jagged diagonal black line represents the limit of experimentally determined properties of nuclei and the magenta line the r-process "path". Vertical and horizontal black lines represent closed neutron or proton shells, sometimes referred to as magic numbers. Colour-shading denotes the different (log) timescales for beta-decay.*

determines whether the r-process occurs is the number of neutrons per seed nucleus [25]. If starting with a seed distribution somewhere around A = 50-80 before rapid neutron capture sets in, the operation of an r-process requires 10 to 150 neutrons per seed nucleus to form all heavier r-nuclei [15]. The question is which kind of environment can provide such a supply of neutrons to act before the β-decay. This condition is satisfied in Type II supernovae (SNII) and neutron star mergers, which are the most accepted candidates for possible sites. Although the general picture of element formation is understood, many questions about the nuclear physics processes and particularly the details of the supernova explosion mechanism remain to be answered [25, 28].

Modellers of r-process nucleosynthesis find the entropy of the expanding matter and the overall neutron/proton ratio to be more useful parameters than temperature and neutron density [25]. In a very neutron-rich environment such as a neutron star, the r-process could occur even at

low entropy [29]. But even a small excess of neutrons over protons can sustain the r-process if the entropy is high enough [5, 6].

Progress in the modelling of type-II supernovae has caused a lot of excitement about the so-called neutrino-driven wind model [30]. Neutrino interaction can result in emission of neutrons [31]. However, until now no r-process can be simulated ab initio without having to call for an arbitrary modification of the model parameters, leading quite often to physically unrealistic scenarios [32]. With regards to neutron-star ejecta (NS), which do not require high entropies [33], the large amount of free neutrons (up to $10^{32} cm^{-3}$) available in such scenario leads to the build-up of the heaviest elements and also to fission within very short timescales. This in turn leads to a recycling of fission products back to the heaviest nuclei via subsequent neutron captures [34, 35].

Observations of low metallicity[1] stars, indicating the history of early galactic evolution, should help to explore the question of whether a superposition of a series of such events with different environmental conditions led to the present solar system r-process composition, or alternatively that a single scenario occurring each time with the same environment conditions is its origin [15, 36–39].

The experimental study of the r-process requires knowledge of the properties of a wide range of isotopes along and near the r-process path, but the vast majority of the r-process nuclei are extremely neutron rich and until now have not been accessible experimentally. However, the next-generation facilities planned worldwide, (e.g RIA [40], FAIR [41] or EURISOL [42]), will produce exotic nuclei in regions of the chart of nuclides that could not be studied until now, and the experimental nuclear-structure studies of such nuclei will become feasible.

1.2 Production of heavy neutron-rich nuclei

As discussed above, radioactive nuclei play an important role in many cosmic phenomena, and the information on these nuclei is particularly important to improve our understanding of the processes that shape our Universe.

The production of heavy neutron-rich in the laboratory nuclei has been a challenging problem in the last decades. Very neutron-rich nuclei are unstable and the more exotic they are, the shorter their half-lives. The battle which faces the physicists is thus the need for high enough yields of

[1] Astronomers use the term metallicity to mean the abundances of all elements heavier than hydrogen, but specially iron

such unstable nuclei, despite their generally low production cross-sections and extremely short half-lives.

Neutron-rich nuclei can be produced by several physical processes such as fusion, quasi-elastic or deep inelastic transfer of some nucleons, fragmentation, and fission. However, fusion, deep inelastic or multi-nucleon transfer can only be applied with thin targets limiting the final production rates [43]. Fragmentation seems to be a better-suited reaction mechanism which allows a large variety of neutron-rich nuclei to be produced. The present dissertation is focused on the production of heavy neutron-rich nuclei by projectile fragmentation, and in particular in cold-fragmentation reactions [16]. These are projectile fragmentation reactions at relativistic energies where mostly protons are abraded from the projectile, while the excitation energy induced is below the particle evaporation threshold. Therefore, these collisions lead to final residues with the same neutron number as the projectile but smaller atomic number. Cold-fragmentation seems to be a well suited reaction mechanism for producing very heavy neutron-rich nuclides which cannot be obtained by fission. When using a ^{208}Pb beam, this reaction mechanism allows to produce heavy neutron-rich nuclei along the closed shell N=126.

There are two main methods for the production and separation of exotic nuclei at present facilities over the world:

- the ISOL(isotope separation on-line) [44] approach, where the exotic nuclei are created by a light ion beam impinging on a thick target and later extracted, ionised and accelerated.

- the in-flight [45] separation, where a beam of energetic heavy ions impinges on a target and the reaction products are carried forward by the kinematics and separated in-flight.

In-flight and ISOL facilities are complementary in many respects. As far as secondary beam-intensities are concerned, the ISOL method appears to be superior for isotopes of selected elements, i.e. those that are quickly and efficiently released from the target-ion source system. In-flight separation, on the other hand, is independent of chemical properties, and thus yields high secondary beam intensities for all elements. The ISOL method suffers from decay losses and is thus in many cases restricted to nuclides with half-lives of a few seconds or more. In contrast, the in-flight method gives access to very short-lived species with half-lives down to the sub-microsecond region.

Recently, a combination of these two methods has been proposed. In this new hybrid scheme, the exotic species are produced by projectile

fragmentation or projectile fission and separated in-flight. They are then stopped in a gas cell, extracted and re-accelerated to energies in the range of tens of MeV/u. The idea of combining the ISOL and in-flight techniques is to get the best out of each method.

1.2.1 General aspects of the projectile fragmentation reactions

The collision of a heavy-ion projectile with a target can be described, as a first approximation, from geometrical parameters. According to the impact parameter of the collision, it will be central or peripheral. In the first case, the collision leads to process such as fusion and multi-fragmentation. The second one leads to the formation of fragments with masses close to the projectile and can be schematically represented as follows: in the instant of the collision, the compressed nucleons in the volume covered by both nuclei, the projectile and the target, are stripped off by friction (abrasion). They constitute a hot region referred to as *participants* and the other nucleons are called *spectators*. A fragment with a mass close to the one of the projectile is produced (See figure 1.4).

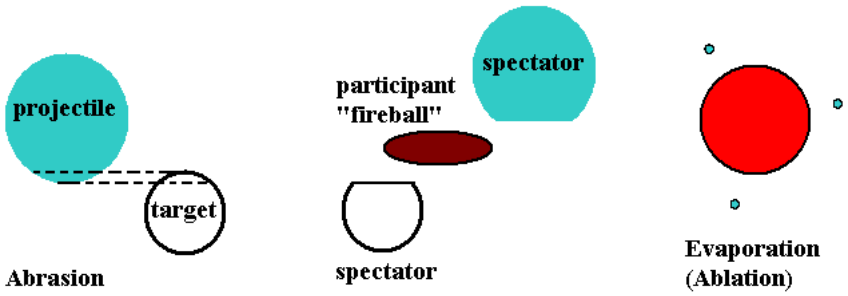

Figure 1.4: *Simplified representation of the abrasion-evaporation process in a peripheral collision.*

The description of the reaction by a two-step process was proposed for the first time by Serber [46]. The first step corresponds to the initial collision between the constituents of the target and projectile nucleus and occurs rapidly, with a characteristic time of $10^{-23}s$. It is necessary to distinguish the fragment finally observed from the *pre-fragment* formed in this first step. It has an important excitation energy proportional, in a first approximation, to the number of nucleons abraded.

In the second step, the pre-fragment is thermalised and it de-excitates by the evaporation of nucleons and the emission of gammas. The

evaporated nucleons are mainly neutrons until the emission probability of neutrons and protons reaches equilibrium, thus de-excitation proceeds by a random emission of either neutrons or protons.

However, it has recently been shown that fragmentation reactions at relativistic energies present large fluctuations in the N/Z distribution of the final fragments and in its excitation-energy distribution [43]. The extreme case of a relatively cold fragmentation, where only protons are abraded from the projectile, while the induced excitation energy is below the particle-emission threshold, has been investigated in cold-fragmentation reactions [16].

In order to estimate the number of fragments produced, computer codes of model descriptions of the fragmentation process in the two-step reaction scheme have been developed. Among them we can highlight EPAX v.2 [47], a semi-empirical parametrisation of the fragmentation cross-section, ABRABLA [48], a Monte Carlo simulation code of the nuclear reaction model describing the nuclear-collision process for energies well above the Fermi energy, and the COFRA [16] code, a simplified analytical version of ABRABLA.

EPAX is an empirical parameterisation of the fragmentation cross-sections based on experimental data. The first version of EPAX [49] was derived using proton-induced spallation cross-sections measured in the GeV energy range. A decade later, when more experimental data from relativistic heavy-ion-induced fragmentation reactions of medium- to heavy-mass projectiles became available, the parameterisation was refined [47] to include new features not observed in the proton-induced reactions, getting a better overall representation of the shapes of the isotope distributions, which leads to better predictions for heavy fragments, for fragments close to the projectile, and for very neutron-deficient medium-mass nuclei.

The EPAX parameterisation is valid only in the *limiting-fragmentation regime* [50], where the fragmentation yields no longer depend on the projectile energy. This regime corresponds to energies well above the Fermi energy ($\approx$ 40 A MeV), where the assumption of the *limiting fragmentation* is valid. According to EPAX, the final residues in the vicinity of the projectile keep a memory of its isotopic composition. This memory is considered to gradually decrease as the fragments further away from the projectile are produced. This constitutes what has been termed the "residue corridor" and is related to the fact that the isotope distributions are mainly governed by statistical evaporation from highly-excited pre-fragments produced in collisions between relativistic heavy ions.

The abrasion-ablation model ABRABLA [48] is based on the participant-

spectator picture. For a given mass loss, the protons and neutrons are assumed to be removed randomly from the projectile. As the spatial distributions of protons and neutrons are very similar, the mean value of the N-over-Z ratio of the pre-fragments is close to that of the projectile. However, the hyper-geometrical distribution predicts an important fluctuation [51]. The excitation energy is mainly given by the energies of the holes in the single-particle level scheme of the projectile after the collision [48]. Most of the pre-fragments are highly excited. They predominantly evaporate neutrons and thus lose part of their neutron excess. Extremely neutron-rich nuclides are produced if only protons are removed. Only in a cold-fragmentation process, which populates the low-energy tail of the excitation-energy distribution, the proton-removal channels survive, and the excitation energies of the pre-fragments are formed below the neutron separation energy [52]. The probability of this extreme case decreases strongly with increasing mass loss.

The COFRA code is an analytical formulation of the abrasion-ablation model [48], where the first stage of the reaction leads to the formation of a pre-fragment whose size depends on the impact parameter, and the excitation energy on the number of nucleons abraded from the nucleon Fermi distribution of the projectile. After thermalisation this pre-fragment is de-excites by nucleon and cluster evaporation, leading to the final residual nucleus. As COFRA only considers neutron evaporation from the pre-fragments formed in the abrasion step, it is limited to areas where the neutron evaporation is more probable than the proton evaporation, thus it is only valid for very neutron-rich nuclei.

In the present dissertation, the cross-sections of heavy neutron-rich nuclei measured in the experiment are going to be systematically compared with the results of EPAX and COFRA. As COFRA only considers neutron evaporation from the pre-fragments, it is fully analytical and thus much faster than ABRABLA. For this reason it can be used to compute very small cross-sections without the need for too much computer time.

1.3 Description β-decay properties

As mentioned in section 1.1, the location of the r-process abundance peaks depends on the underlying nuclear-structure properties of the nuclei involved in the r-process path. The region around N=126 is responsible for the formation of the A $\approx$ 195 peak in the r-process abundance pattern. Knowledge of nuclear properties of heavy neutron-rich nuclei far from stability is needed to correctly model the r-process in this mass region.

In order to predict the decay properties of nuclei far from stability, it is essential to understand their nuclear structure and bulk properties. However, this represents a challenge for heavy neutron-rich nuclei, for which most of the information on their structure has been attained through the extrapolation of experimentally-derived measurements of nuclei close to stability.

A theory on β-decay was developed by Fermi in 1934 [53]. During the process of β decay, two particles, an electron and a neutrino are emitted from the nucleus. β-decay half-lives depend on the differences in spin, parity and energy of the initial and final states to which the mother decays. Each particle (electron and neutrino), has a spin of 1/2 and can carry orbital angular momentum. If their spins are anti-parallel, the nuclear system will undergo a Fermi decay [54]. In an allowed/favoured Fermi decay, the electron and neutrino are emitted with zero units of orbital angular momentum. Thus, there will be no change in the nuclear spin, $\Delta J = |J_i - J_j| = 0$.

If the electron and neutrino have their spins aligned parallel to one another, then the system may experience a Gamow-Teller decay (GT). For an allowed Gamow-Teller decay, the electron and neutrino carry a total angular momentum of 1 unit, and thus J_i and J_j must be coupled through a vector of length 1: $\overrightarrow{J_i} = \overrightarrow{J_j} + \overrightarrow{1}$. This is only possible if $\Delta J = 0$ or 1 (except for $J_i = 0$ and $J_j = 0$, in which case only Fermi transition can contribute [54]). As for allowed Fermi decays, the initial and final states following an allowed Gamow-Teller decay will have the same parity, following the condition $\Delta\pi = (-1)^{\ell}$, where π is the parity of the system and ℓ the angular momentum.

Allowed β-decay transitions are among the fastest. However, it is also possible to undergo β transitions in which $\Delta J > 1$ and/or the initial and final states have opposite parities. These transitions are classified as forbidden. To accomplish the change in parity, the electron and neutrino must be emitted with an odd value of the orbital angular momentum relative to the nucleus. The forbidden decays with $\ell = 1$ are called first-forbidden decays(ff), and like the allowed decays, they have Fermi-type

decays, with the electron and the neutrino spin anti-parallel to one another (S=0), and Gamow-Teller-type decays, with the spin parallel (S=1). The selection rules for first-forbidden decays are $\Delta J = 0, 1, 2$ and $\Delta\pi =$ yes.

To compare the half-lives of different β-transitions, we must first correct the variation in the β-decay probability that results from differences in the daughter atomic number Z' or in the endpoint energy ε_0. This is done through the Fermi Function $f(Z', \varepsilon_0)$, which has been discussed and tabulated in Refs. [55] and [56]. The product $ft_{1/2}$ is the *comparative half-life* or ft value, which is usually given as $log_{10}ft$, where $t_{1/2}$ is always in seconds. Most of the allowed decays have $logft$ values in the range of 3.5 to 7.5, and first-forbidden decays generally fall into the range of 6.0 to 9.0 [54].

According to Fermi's golden rule, the β-decay half-life can be expressed in terms of the so-called β-strength function ($S_\beta(E) \approx \mid M_{fi} \mid^2$, where $\mid M_{fi} \mid^2$ is the nuclear matrix element) as follows [57]

$$1/T_{1/2} = \sum_{E_i \geq 0}^{E_i \leq Q_\beta} S_\beta(E_i) \times f(Z, Q_\beta - E_i) \tag{1.2}$$

where Q_β is the maximum β-decay energy (or the isobaric mass difference) and $f(Z, Q_\beta - E_i)$ the Fermi function.

At high excitation energies and for heavier nuclei, the forbidden transitions dominate [57]. The existence of very fast, first-forbidden transitions in the region of ^{208}Pb is well known [58]. In contrast to the relative simplicity of allowed decays, there are six different matrix elements for first-forbidden decays, and the analysis of decay rates becomes very complicated.

Although the β-decay mechanism is in principle understood, it is difficult to produce a satisfactory quantitative description of the β-decay, because the nucleus is a complex system comprised of many particles, in which residual interactions of various types may lead to collective excitations, which can have an important effect on the β-decay properties.

Solving the quantum many-body problem remains a challenge in all areas of physics. Nevertheless, great progress has been made using the concepts of the so-called mean field theory (also known as self consistent field theory). Most of the formal development of the mean field theory and its extensions can be found in the book by Ring and Schuck [59]. In general, the models for global calculations of β-decay rates developed in the last decades can be divided in microscopic models with empirical mean field potentials, and self-consistent mean field models. An overview of the different theoretical approaches is given in the reviews of Grotz and

Klapdor [60], B. Pfeiffer et al. [61], J. Engel [62] and the most recent by I. Borzov [63].

1.4 Experimental techniques for measuring β-decay half-lives

The technique of choice for measuring $T_{1/2}$ will depend on the lifetimes themselves and on the production technique of the nuclei investigated. There are essentially two methods for measuring half-lives:

Measurement of the variation of the population of a sample of nuclei over time:

A straightforward technique to measure nuclear lifetimes is to perform a direct measurement of the exponential decay of the activity of a sample of nuclei over time [64]. The fitting of the decay curve by an exponential function gives the decay constant λ directly, and thus $T_{1/2}$.

In order to use this technique it is first necessary to produce a sufficient amount of nuclei in a given period of time (shorter than the expected half-life of the nuclei) and then measure the activity of the sample at successive intervals over a time range comparable to the half-life [65]. As a consequence this technique is limited to nuclei with half-lives ranging from few seconds to a few years. If there is more than one activity present in the sample, the decay constants can be resolved by a statistical analysis of the contributions of the exponential terms of the different decay chains.

For nuclear species with extremely long half-lives, the decay rate is essentially constant with time so that λ can be obtained directly from the ratio of the number of detected particles per unit time over the total number of atoms in the sample.

Ion-cooler rings and ion traps allow the preparation and preservation of β-unstable atoms in well-defined, high atomic charge states and the precise determination of their lifetime [66–69]. Each ion of a certain m/q circulating in a storage ring induces a signal at each passage with a well-defined frequency. Recording the number of circulating ion species over time allows us to determine their lifetimes. Depending on the nuclear half-life, two methods are employed: the Schotty Mass Spectrometry (SMS), using cooled ion beams, and the Isochronous Mass Spectrometry (IMS), without electron cooling. More details of these methods can be found in Ref. [70–72]. This is a powerful, but limited technique, due to the injection efficiency of the exotic nuclei in the ring, and the half-lives of the nuclei

which range from a few ms to some 100 years. Due to these limitations, this technique cannot be used for very exotic nuclei with low production rates and lifetimes shorter than a few ms.

Ion traps store an ensemble of ions using time-dependent electromagnetic fields. If the ions are neutralised they are no longer influenced by the electric fields and are emitted along the axis of the trap. If they are neutralised in the field free region, the neutrals are energetic and can be detected by a channel electron multiplier. The neutral signal is proportional to the number of ions in the trap and hence can be used to measure lifetimes. Also open traps make efficient detection of the decay products possible. The magnetic field of the Penning traps can be used to guide the β-particles to their detectors.

Delayed-coincidence technique:

Half-lives from few nanoseconds up to few seconds can be measured electronically in coincidence experiments. The nuclei produced may be deposited either into a catcher or on rotating drums or moving tapes, with detectors positioned along the travel path. β-decay lifetimes are determined by the time-delayed correlations between the detection of a nucleus implanted and the subsequent β-decay events. The time-difference distribution depends on the decay constant λ of the implanted nucleus, the detection efficiency, the daughter decay half-life and the background rate.

In time-correlation analysis, all correlations which are not affiliated with the nucleus under study constitute the background. The background found in the detection systems depends heavily on the method used for the production of the nuclei, and also will depend on the beam purity, the production rate and the lifetimes of the nuclei.

In the technique of delayed coincidences, there are two questions to be taken into account to establish the significance of the existence of a 'true' correlation: (i) consideration of the possibility that the random background of uncorrelated events could simulate a correlation, and (ii) whether the data are compatible with the assumption that the measured time values originate from the decay of a given radioactive species.

In experiments performed using the ISOL technique, the nuclei produced undergo mass-separation and are delivered to the measuring station. The activity is accumulated on a moving-tape device or rotating drums for a given time, and then moved into the detection setup for the half-life measurement. During the measurement of the bulk activity, the beam is deflected far away from the collection point, and after a given time, a new cycle is started with a new accumulation. This technique

has been widely used in different laboratories over the world, e.g. GSI [73–75], ISOLDE [76–78], LISOL [79], TRIUMF [80]. Examples of half-life measurements using thermal fission at ILL can be found in Ref. [81, 82].

Although measurements at ISOL facilities have proven to be quite successful in determining the β-decay information for radioactive species, it has some shortcomings:

- ISOL production suffers the general difficulty of not achieving high beam purity due to the many isobars of different elements produced simultaneously within the target. These contaminants may alter the observed half-life significantly, unless the radioactive decay is characterised by the energy of a γ-transition or α-decay, since in this technique the bulk activity of the implanted species is monitored, rather than monitoring the activity on a nuclide-by-nuclide basis. Furthermore, refractory elements are generally difficult to produce due to the high temperatures required to make them volatile.

- The low rates for the production of very neutron-rich radioactive beams makes impractical bulk activity measurement where the beam is cycled on and off.

- The ISOL method is also limited by the diffusion time and release efficiency of the target ion-source system, and is thus in many cases restricted to nuclides with half-lives longer than a few milliseconds.

Fast beams from projectile fragmentation offer a means by which some of these challenges can be overcome:

- Highest selectivity and sensitivity is achieved by in-flight separation and event-by-event identification, allowing for decay studies at the extreme limits and half-life measurements with a reduced background.

- Low beam losses due to the fast (sub-microsecond) and chemically-independent separation and transport to the experiment.

However, in projectile fragmentation, the interaction of the heavy-ion beams at relativistic energies with matter causes electromagnetic radiation of atomic origin. Depending on the projectile energy, the atomic background can extend up to several hundred keV. Projectile fragmentation also suffers from low intensities and low beam quality.

Time-delayed coincidences using projectile fragmentation for the production of the nuclei can be performed either using a pulsed or a continuous beam. In the pulsed-beam approach, a radioactive beam is

implanted within a collection target for a given implantation time. The beam is then inhibited for a period of time, when the activity of the implants is monitored. β-decay half-lives are determined by measurements of the absolute time of detection for a given parent nucleus and the subsequent β events during the beam-off period. The technique, first used by Murphy et al. [83] is capable of measuring lifetimes as short as few milliseconds.

In order to avoid beam losses, a device for β-decay studies using a beam continuously implanted into an active catcher detector is preferable, eliminating the need for cycling the beam on and off. Double-sided silicon strip detectors (DSSD) have been extensively used due to their high pixelation, which allows establishing the continuous implantation of short-lived nuclei and allows the correlation of an implantation and subsequent β-decays on an event-by-event basis.

The technique of measuring half-lives using in-flight separation has been extensively applied and refined over the years at different facilities, as for example at GSI [84–87], MSU [88–91], GANIL [92–97], LAMPF [98], RIKEN [99].

β-delayed neutron emission [88, 97, 98] and β-delayed γ spectroscopy [73–76, 78–80, 94, 96, 100–103] allow high-resolution experiments to be performed, in which not only half-lives but also neutron-emission probabilities and detailed information on the structure of the nuclei can be obtained.

1.5 Mathematical methods to determine half-lives

The density distribution of radioactive decays of one species of nuclei is given by

$$|dn/dt| = \lambda n_0 exp(-\lambda t) \tag{1.3}$$

The statistical analysis to deduce the decay constant λ may be complicated by the fact that the radioactive decays can only be observed in a limited time range, and in addition, events of other species which decay with different decay constants or background events may be mixed in. Also if daughter nuclei produced in the primary decay are also radioactive, an even more complex situation appears.

Elaborated methods have been developed to determine half-lives of radioactive species and their statistical uncertainties (see, e.g. Ref [104] and references therein). In the following subsections a brief review on some

methods is presented.

First moment of the decay times

If the sample under study contains only one species of radioactive nuclei and any background is excluded, the first moment or average of the measured decay times is an estimate of the inverse of the decay constant, $1/\lambda$. In order to be able to apply this method, the full time range must be covered by the measurement, that is, t_{min} must be very small and t_{max} must be very large compared to $1/\lambda$.

$$\bar{t} = \frac{\sum_{i=0}^{n} t_i}{n} = \frac{1}{\lambda} = \tau = T_{1/2}/ln2 \tag{1.4}$$

Exponential decay curve

In the conventional analysis of radioactive-decay data, the individual decay times are sorted into a spectrum with time intervals of constant width Δt. The statistical analysis of the number of observed counts in a certain time bin may rely on the assumption of an underlying normal distribution. The mathematically correct distribution is Poisson but for larger number of counts it can well be approximated by a Gaussian.

The expected shape of the time-interval spectrum is given by the density distribution shown in eq. 1.3. This spectrum has the shape of an exponential function and the decay constant can be determined by a fit. A least-squares fit is restricted to large event numbers, while the maximum-likelihood method can also be applied in the case of poor statistics [105]. Contributions of another radioactive species and of background events can be recognised and extracted by using a more complex fit function.

Logarithmic time scale

An unusual representation of decay-time and time-interval spectra in logarithmic time bins, proposed in Refs. [106] and [107] gives a better visualisation of the data and can be applied to few-event statistics. This method consists of sorting the individual decay times into a spectrum with time intervals Δt which have a width that is proportional to the time t, that means $\Delta t/t =$ constant.

The corresponding density distribution is a bell-shaped, slightly asymmetric curve given by [104]

$$\frac{dn}{d(lnt)} = n_0 \; exp(lnt + ln\lambda) \cdot exp(-exp(lnt + ln\lambda)) \tag{1.5}$$

The maximum of this function is located at $ln\frac{1}{\lambda}$. Even though this logarithmic time-bin representation does not influence the information of the data, it facilitates the visualisation of the decay spectra with very low counting rates and allows to store the relevant information of decay times over a large range with a moderate number of channels.

In the present dissertation, a new technique has been developed to measure the β-decay half-lives of exotic nuclei in complex background conditions, using position and time correlations between the implantation of a given fragment and the subsequent β-decay.

The rather complex background conditions found in this piece of work cannot be easily modelled with an analytical function, and thus we propose to determine the half-lives by applying the least-squares method using a numerical function to calculate the number of events per time interval. This work represents a first step towards a new and promising set of experiments, which focus on nuclear-structure studies of exotic nuclei at GSI in Germany.

Chapter 2

Production and identification of heavy ions: experimental technique

The experimental technique used for the production of heavy neutron-rich nuclei is the in-flight fragmentation of relativistic heavy projectiles. The beam used was ^{208}Pb at 1 GeV per nucleon impinging on a beryllium target. The experiment requires the use of a heavy-ion accelerator to provide the relativistic primary beam and a high-resolution magnetic spectrometer equipped with different detectors to avoid any ambiguity when identifying the projectile residues produced in the reaction. The SIS/FRS [17] facility of the Gesellschaft für Schwerionenforschung (GSI) is the best suited for this kind of experiment. In this chapter the experimental devices used for the beam delivery and for the production and identification of heavy neutron-rich nuclei will be described.

2.1 The GSI experimental facility

2.1.1 Accelerator system

The GSI accelerator complex facility located in Darmstadt, Germany, is one of the leading facilities for relativistic heavy-ion nuclear research. A schematic view of the GSI facility is shown in figure 2.1. The beams are extracted from the ion source, pre-accelerated and then injected into the Universal Linear Accelerator (UNILAC), which accelerates primary beams up to 12 A MeV. The ions are then injected into the *SchwerIonen Synchrotron* (SIS) [108] where they are further accelerated. A thin carbon

foil at the entrance of the SIS is used to increase the charge state of the ions of interest and to be able to reach the desired final energy. The maximum energies achieved by SIS are determined by its maximum magnetic bending power, 18 Tm. Depending on the injected charge state and the N/Z ratio, the maximum energies vary from 1 to 4.5 GeV per nucleon. Our experiment was performed with a ^{208}Pb beam, at 1 A GeV. The ionic charge of the beam at the exit of the SIS was q = + 67. SIS was operated in slow-extraction mode. The beam cycle was about 10 s long and the beam was extracted with a spill length of about 1.5 s. The beam intensity was varied between 10^5 and 10^7 ions/s, according to our needs. After acceleration, the beam was driven to the Fragment Separator (FRS) experimental area through the extraction beam line.

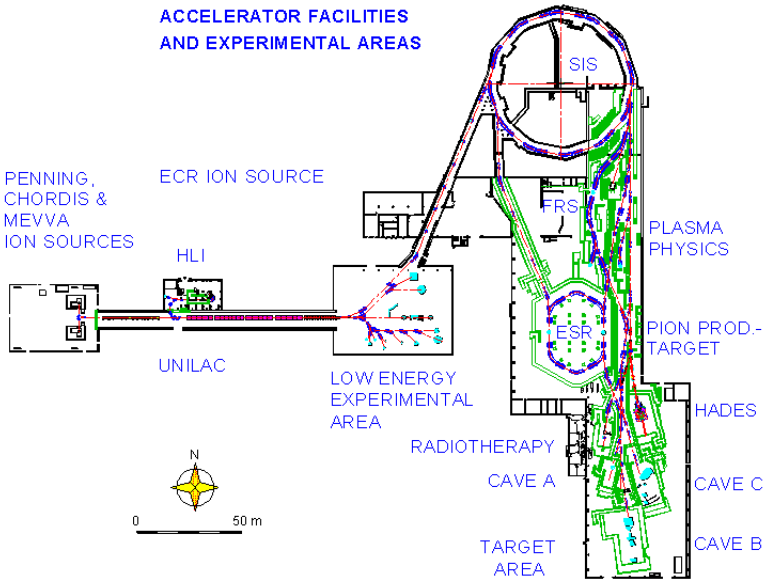

Figure 2.1: *Schematic view of the GSI accelerator facilities and experimental areas [109]*

2.1.2 Beam-profile monitoring

In order to measure the spatial distributions and to centre the beam precisely on the production target, beam-profile monitors, so-called *current grids*, with gas amplification and current readout are installed at the entrance of the FRS. In order to measure the horizontal x and vertical y

intensity beam distributions, two planes of parallel wires mounted between metal-foil cathodes in a P10 gas chamber are used [110]. By tuning the magnets on the path from SIS to the target area, it is possible to correct any angle or offset of the beam using the measured x and y beam position profile.

2.1.3 Beam-current monitor

A Secondary Electron Transmission Monitor (SEETRAM) was developed at GSI [111] to survey the heavy-ion beam intensities. SEETRAM and the associated equipment installed at the FRS target station provide valuable information on spill structure and the extraction efficiency. The SEETRAM also serves for normalisation of the production cross-sections. For most experiments it is important that the primary-beam intensity is distributed as homogeneously as possible over the extraction time in order to avoid unnecessary pile-up rates and dead-time losses. A fast monitoring of the beam intensity over the extraction time allows the extraction profile to be determined. This information on the spill structure helps us to find the optimum tuning of the SIS extraction which is most suited to the experimental requirements of a given experiment. To measure absolute production cross-sections, it is necessary to determine the total number of impinging projectiles. Thus, the SEETRAM registers the beam intensity continuously during the whole experiment.

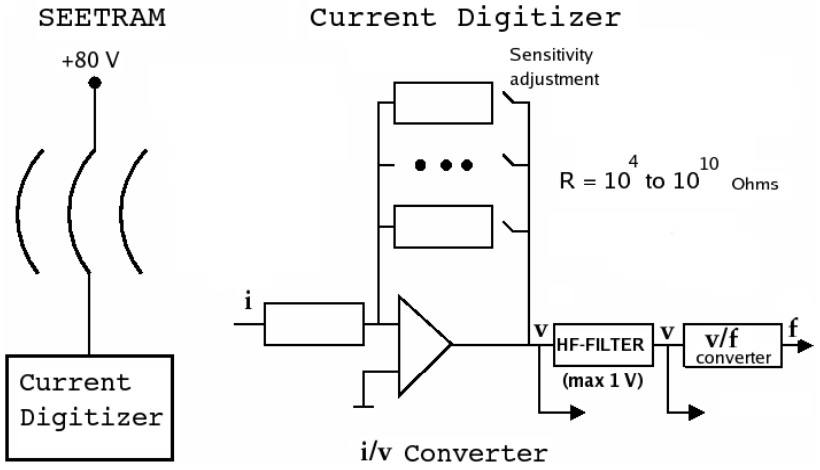

Figure 2.2: *Left: Diagram of the beam monitor SEETRAM . Right: the current digitiser. Adapted from [112]*

SEETRAM operation is based on the emission of secondary electrons from thin metal foils by the passage of the ions. It consists of three aluminium foils, each of 10 μm thickness, placed in a vacuum, parallel to each other and orthogonal to the beam direction. The outer foils are connected to a positive voltage (+80 V), and the inner foil is insulated from the rest of the detector and connected to the ground via a current integrator. When the beam passes through the SEETRAM, electrons close to the surface leave the inner foil, thus generating a positive current in the central layer which is measured by a current digitiser. The current digitiser consist of several stages: First, the input current (i) is transformed into a voltage (v). The fast analogue output of this signal can be used as a monitor for measuring the extraction profile. Secondly, the signal passes a filter with a time constant of 1 s. The analogue output of this signal is also available. Finally, the signal is digitised. The resulting quantity is proportional to the number of incoming particles. By changing a resistance of the i/v converter in the current digitiser from 10^4 to 10^{10} Ω, the sensitivity of the SEETRAM can be changed from 10^{-4} to 10^{-10} A, allowing seven levels of sensitivity. The current digitiser produces an adjustable constant offset current which allows us to identify any unwanted noise signals produced. Such background signals have to be subtracted from the number of counts in a spill in order to obtain the actual number of SEETRAM units produced by the passage of the beam particles.

The SEETRAM yield depends not only on the ion species and the beam energy but is also sensitive to surface impurities. Long irradiations lead to a reduction of the secondary-electron yield in the region around the beam position. Therefore, the SEETRAM calibration has to be performed for every experiment (See section 3.1).

The SEETRAM thickness is 8.9 mg/cm^2 Al and the nuclear reaction probability is less than 0.1% for a ^{208}Pb beam at 1 A GeV. This makes it a very efficient beam monitor that has almost no influence on the beam quality and does not disturb the cross-section measurements.

2.1.4 The production target

The nature and thickness of the production target was chosen as a compromise between a maximised production of fragments and a low secondary reaction rate. We used two different ^9Be targets, with thickness of 1023 $\pm$ 3 mg/cm^2 for measuring the heavy fragments and 2526 $\pm$ 1 mg/cm^2 for the lighter ones, both of them having a 221 mg/cm^2 Nb stripping backing. The thickness of the targets represents $\approx$ 10-20 % of the range of the projectile, which provides the highest rate of projectile

fragments [18]. The effect of the stripper backing the target, is that the charge distribution of the residues at the FRS entrance results in a large fraction of bare, and small contributions of hydrogen-like or helium-like nuclei. The expected number of nuclear reactions in these targets, and the resulting charge-state distributions (as predicted with the code AMADEUS [113]), are summarised in Table 2.1 .

Table 2.1: *Probabilities of nuclear reactions and ionic charge states for the targets used in the experiment as predicted by AMADEUS*

$Thickness\ mg/cm^2$	nucl. react (%)	0e	1e	2e
1023	19.6	0.915	0.083	0.002
2526	41.6	0.894	0.103	0.003

2.1.5 The fragment separator

The Fragment Separator (FRS) [17] is an achromatic high-resolution forward magnetic spectrometer, designed for research studies using relativistic heavy ions. The momentum resolving power is 1500 for an emittance of 20 π mm mrad. Heavy-ion beams with magnetic rigidities ranging from 5 to 18 Tm can be analysed using this spectrometer.

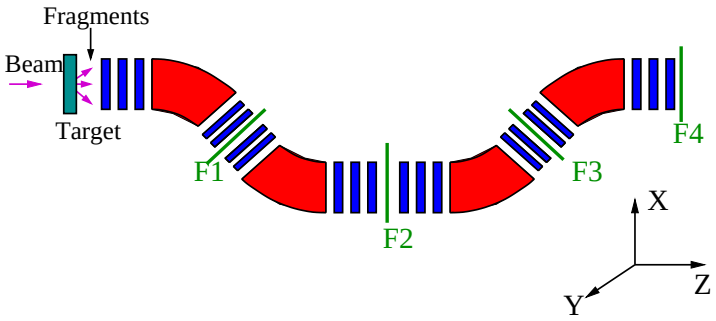

Figure 2.3: *Layout of the FRS at the GSI facility adapted from [114]. Quadrupoles placed before and after each dipole fulfil first-order focusing conditions. Sextupoles placed in front and behind each dipole, not shown in the figure, correct second-order aberrations.*

The FRS has four stages, each one consisting of a 30° dipole magnet and a set of quadrupoles and sextupoles, before and after the dipole, to fulfil first-order focusing and correct second-order optical aberrations. (See figure 2.3). A vacuum line, separated by a Ti window from the SIS high

vacuum, traverses the FRS from the entrance to the exit along a distance of approximately 70 m. The acceptance of the device is limited to ± 1.5 % in momentum and 15 mrad in angle around the beam axis. The dipole magnets can be operated up to a maximum magnetic field of 1.6 T and are controlled by calibrated Hall probes that make it possible to measure the magnetic fields inside the dipoles with a relative uncertainty of 10^{-4}. The nominal curvature radius of 11.25m of the 30° dipoles constrains the maximum magnetic rigidity accepted by the FRS up to 18 Tm.

The FRS, being a magnetic spectrometer, separates the fragments according to the ratio of mass number over the ionic charge, and velocity according to the magnetic rigidity

$$B\rho = \frac{A}{Q} \cdot \beta\gamma \cdot \frac{uc}{e} \tag{2.1}$$

where B is the magnetic field (uniform and transversal to the particle trajectory), ρ is the deflection radius, A is the mass number , Q is the ionic charge, e is the electron charge, c is the speed of light, u is the mass unit and $\beta\gamma$ is the reduced momentum from the relativistic parameters with $\beta = v/c$, where v is the velocity of the ion.

Since the magnetic field of the dipoles is homogeneous, two fragments with different magnetic rigidities and the same velocity will follow trajectories with different radii and will reach F2 and F4 at different positions. The difference between these two positions and the magnetic rigidities is related to the dispersions in the two sections of the FRS as follows:

$$B\rho_2 = (B\rho_0)_2(1 + \frac{x_2}{D_2}) \tag{2.2}$$

$$B\rho_4 = (B\rho_0)_4(1 + \frac{x_4 - M \cdot x_2}{D_4}) \tag{2.3}$$

where $(B\rho_0)_2$ and $(B\rho_0)_4$ are the magnetic rigidities of the fragment on the central trajectory with the radius $(\rho_0)_2$ and $(\rho_0)_4$ at F2 and F4 respectively, D_2 and D_4 are the dispersions at each section of the FRS, M is the magnification between the intermediate F2 and the final F4 focal planes, and x_2 and x_4 their respective positions.

Since the system is achromatic, the magnification is related to the dispersions as follows:

$$M = \frac{D_4}{D_2} \tag{2.4}$$

The FRS can be operated either in achromatic or energy-loss mode [17]. In the achromatic mode of operation point-to-point images in the x-direction are required at all four focal planes. In order for the achromatic condition at the final focal plane to be achieved, the image size and the angular divergence should be independent from the momentum spread of the incident beam. The difference between the achromatic mode and the energy-loss mode of operation is that in the latter the target is placed in the central focal plane, and precise measurements of the energy transfers in nuclear reactions become possible [17, 115, 116] independently from the momentum spread of the incident projectile beam.

The first magnetic selection

The first step in the separation is achieved by the first two dipoles. Since the reaction mechanism approximately conserves the velocity, this selection is mainly sensitive to A/Q. The magnetic fields of the first two dipoles can be opportunely tuned so that a selected nucleus transverses the FRS with a momentum p_1 following the central trajectory. If all ions passing through the separator are fully-stripped, the first stage selects a band of isotopes along the line $A/Z \approx$ constant, the width of which is determined by the velocity spread of the fragments [117] and the acceptance of the spectrometer ($\pm 1.5\%$).

A considerable number of fragments, in the vicinity of the reference A/Z, are also transmitted at the same time as the ones that have been selected, and as a consequence, a second selection is needed.

The energy loss in the intermediate degrader and the second selection in $B\rho$

At the intermediate focal plane of the FRS a velocity degrader is placed, that is, a layer of material designed to slow down the ions [18]. Similarly to the differential energy loss dE/dx one can define the specific momentum loss $d\beta/dx$, being β the relativistic velocity parameter which is proportional to the momentum per rest mass. At relativistic energies the differential energy loss scales with $dE/dx \approx Z^2$ whereas $d\beta/dx \approx Z^2/A$ [18]. The energy loss in a thick layer is in between these two extremes.

The fragments transmitted by the first two dipoles with close values of A/Z, will have different p_2 momentum values after the reduction of their velocity, according to the energy loss in the degrader. Then, they can be separated in the second stage of the FRS by a new selection in magnetic rigidity $B\rho_2$.

The magnetic fields of the last two dipoles have to be adjusted according to

$$\frac{B\rho_2}{B\rho_1} = \frac{p_2}{p_1} \tag{2.5}$$

in order to select the fragment with momentum p_2 that we finally want to transmit.

If we represent the effect of the first selection ($B\rho_1$) as a band in the nuclear chart, the second selection can be described by a band secant to the first one (see figure 2.4). Due to the momentum acceptance of the FRS all the fragments in the overlap zone of the two bands are transmitted. The position of the second selection over the first band depends on the value p_2/p_1 of the momenta, that is, of the $B\rho_2$ value.

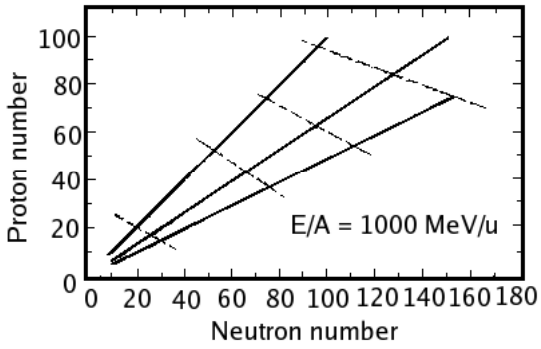

Figure 2.4: *Selection criteria, presented in the chart of the nuclides. The region covered by the first selection (band defined by two consecutive solid lines) depends on the magnetic rigidity set in the first section of the FRS. The second selection (area defined by two consecutive dashed lines) varies with the ratio of the magnetic rigidities of the 1st and 2nd sections of the FRS, and with the thickness of the degrader. Simulation taken from [18]. The curves are calculated for a 1000 MeV/u ^{238}U beam impinging on a beryllium target with a constant thickness $t/r_p = 0.15$ and an aluminium intermediate degrader with $d/r_f = 0.5$, being t and d the target and degrader thickness respectively and r_p and r_f the range of the projectiles and fragments respectively.*

In general it is considered that the separation after the second selection is optimal using a degrader with a thickness equivalent to half of the range of the fragments [18].

For a given isotope, the degrader can be opportunely shaped in such a way that the momentum dispersion behind the first dipole group (1st

and 2nd dipole) is compensated by the second dipole group (3rd and 4th dipole). Thus the system is achromatic for this particular isotope [18]. A special case is the monoenergetic degrader which bunches the momentum width in a way that the momentum at the exit is independent from the position at the intermediate focal plane. In the following sections, these two types of degraders used in the FRS are described in more detail.

2.1.6 The different FRS degraders

The achromatic degrader

The FRS degrader system can be profiled in such a way that the position of the image is independent from the momentum of the ions. If there is no matter in the beam line, this achromaticity property is represented by:

$$D_2 = -D_1 V_2 \tag{2.6}$$

where D_1 and D_2 are the dispersions of the 1^{st} and 2^{nd} group of magnets respectively, and V_2 is the magnification of the second group. When an homogeneous layer of matter is placed in the beam line, this property no longer exits.

Lets consider two ions with momentums p_0 and $p_1 = p_0 + \Delta p$. Their images in the intermediate focal plane will be separated by

$$\Delta x = D_1 \frac{\Delta p}{p_0} \tag{2.7}$$

In the degrader, these ions lose $-\delta p_0$ and $-\delta p_1$ of their momentum respectively. The degrader slope along the dispersive x-direction can be adjusted with two wedge-shaped discs [17] in such a way that a focus in the x-direction is achieved, and thus,

$$\frac{p_1 + \delta p_1}{p_0 + \delta p_0} = \frac{p_1}{p_0} \tag{2.8}$$

or

$$\frac{\delta p_1}{p_1} = \frac{\delta p_o}{p_o} \tag{2.9}$$

The gradient thickness $\frac{\Delta e}{\Delta x}$ required to shape an achromatic degrader can be obtained with the help of the analytical expressions for the range of a particular isotope in a layer of matter.

For a given isotope with momentum p, mass number A and atomic number Z, the range in a layer of matter can be written in a first-order approximation as follows [118]

$$R \approx k\frac{A}{Z^2}p^{\lambda} \tag{2.10}$$

and

$$\frac{\delta R}{R} \approx \lambda\frac{\delta p}{p} \tag{2.11}$$

The parameters k and λ depend on the stopping material. According to Ref. [118]

$$k = k_o\frac{A_d}{Z_d} \tag{2.12}$$

$$k_o = 42.3 + 0.22Z_d(g/cm^2) \tag{2.13}$$

$$\lambda = \lambda_0 + \lambda_1\frac{E}{A} \tag{2.14}$$

$$\lambda_0 = 2.88 - 1.38 \cdot 10^{-3}Z_d \tag{2.15}$$

$$\lambda_1 = -4.62 \cdot 10^{-4} + 3.81 \cdot 10^{-7}Z_d(MeV/u)^{-1} \tag{2.16}$$

Z_d and A_d are respectively the atomic number and the mass number of the layer of matter. The parameter λ has a small dependence on the energy E/A, but it will be considered as a constant.

Lets consider e_0 and e_1 the thickness which traverses the ions with momentum p_0 and p_1 respectively, being $e_{0,1} = -\delta R_{0,1}$, then

$$-e_0 \approx k\frac{A}{Z^2}p_0^{\lambda}\lambda\frac{\delta p_0}{p_0} \tag{2.17}$$

and

$$-e_1 \approx k\frac{A}{Z^2}p_1^{\lambda}\lambda\frac{\delta p_1}{p_1} \tag{2.18}$$

Thus, the corresponding angle for an achromatic degrader can be approximated by [119]

$$tan\theta_a = \frac{\Delta e}{\Delta x} = \frac{e_1 - e_0}{\Delta x} \approx \lambda\frac{e_0}{D_1} \tag{2.19}$$

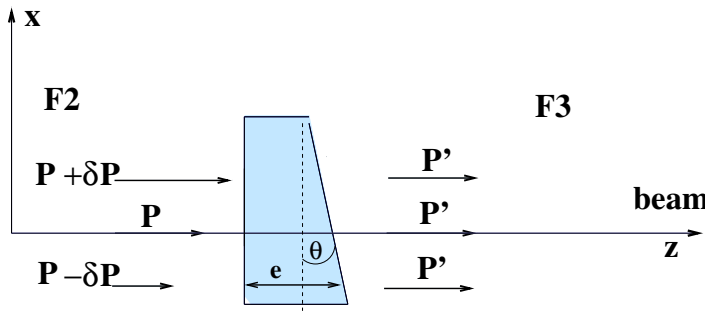

Figure 2.5: *Effect of the angle of the intermediate monoenergetic degrader.*

The monoenergetic degrader

The energy loss of a fragment after traversing an intermediate monoenergetic degrader, does not depend on its position at the intermediate focal plane.

In the intermediate focal plane ions of a given type arrive with different momenta p_0 and $p_1(1 + \Delta x/D_1)$ (D_1 is the dispersion of the first group of magnets) and ranges R_0 and $R_0 + \Delta R$.

Using equations 2.7 and 2.11 we can approximate the range difference as follows

$$\Delta R \approx \lambda \frac{\Delta p}{p} R_0 \tag{2.20}$$

$$\Delta R = \lambda \frac{\Delta x}{D_1} R_0 \tag{2.21}$$

As the relative momentum widths are reciprocal to the corresponding residual ranges, the difference in momentum (and therefore in energy) of fragments can be compensated by introducing a gradient thickness $\Delta e = \Delta R$, and thus,

$$tan\theta_m = \frac{\Delta e}{\Delta x}$$

$$tan\theta_m \approx \lambda \frac{R_0}{D_1} \tag{2.22}$$

The relation between the achromatic and monoenergetic slopes of the intermediate degrader is given by

$$\frac{\theta_a}{\theta_m} = \frac{e_0}{R_0} \tag{2.23}$$

As the angle of the wedge is increased to compensate the momentum spread of the fragment of interest (see figure 2.5), the different energies are bunched up independent of the position they had in the intermediate focal plane F2.

Figure 2.6 shows an example of the phase-space imaging taken from Ref. [117]. The degrader slope was changed in such a way so that a focus in x-direction, (achromatic degrader, upper panel) or energy bunching (monoenergetic degrader, lower panel) were achieved. As can be seen, an increase in the degrader angle would bunch the momentum distribution of the beam, until an optimum value is reached, where the momentum spread of the particles is only determined by the separator resolution and the energy straggling in the degrader.

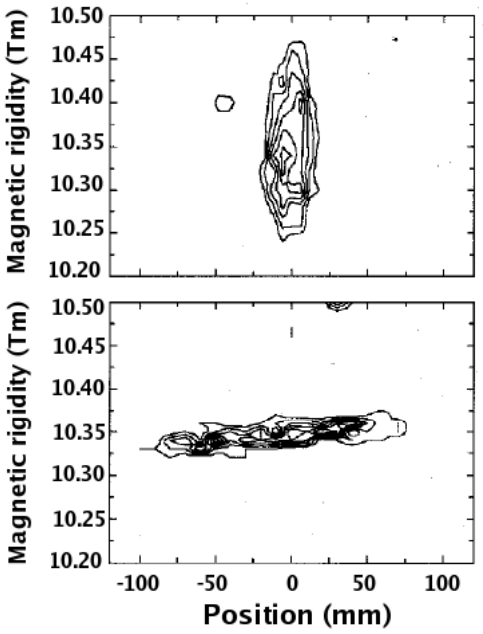

Figure 2.6: *Contour plots of the particle distributions at the final focal plane of the FRS for an achromatic (upper panel) and an (almost) monoenergetic (lower panel) degrader. The coordinates are position (mm) and magnetic beam rigidity (Tm). Figure taken from Ref. [117]*

2.2 Detection equipment

Figure 2.7 shows the FRS detection equipment used in the present experiment. The working principles of the different detectors are described in the following sections.

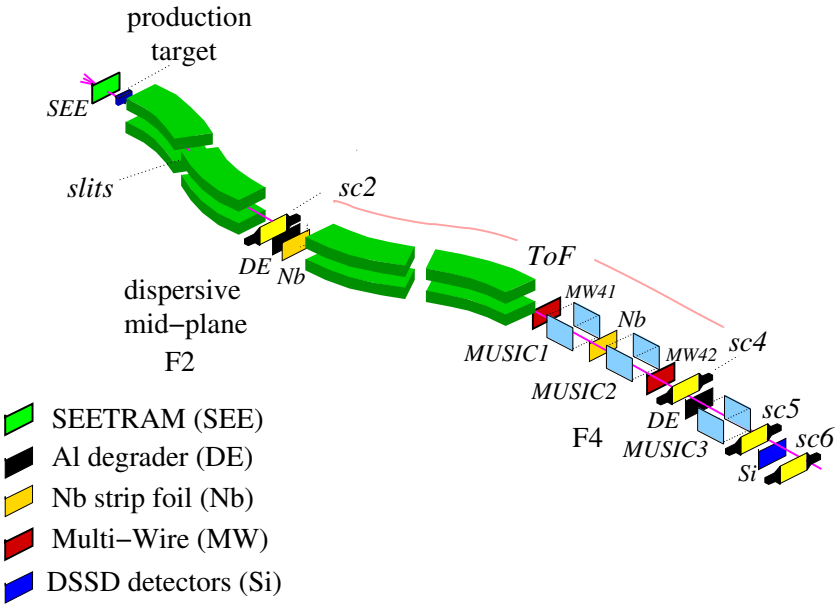

Figure 2.7: *Schematic view of the FRS experimental setup used in the present experiment*

2.2.1 The plastic scintillators

Two plastic scintillation detectors, SC2 and SC4, were used to determine the horizontal positions of the fragments at the intermediate and final focal plane (x_2,x_4) by the time difference of the signals arriving at the two photo-multipliers (Hamamatsu HM2431), mounted at the left-hand and at the right-hand side.

The scintillators are made of Bicron BC420, a special kind of plastic characterised by a high efficiency in the production of light, and by a fast time-response of ≈ 5 ns. The sensitive area of the scintillators is 210 mm x 80 mm for SC2 and 200 mm x 80 mm for SC4. The intrinsic time resolution of these detectors is $\Delta t = 40$ ps (FWHM) [120]. Therefore the position resolution $\Delta x = c_{scint} \cdot \Delta t/2$ is $\Delta x = 4$ mm, being the effective speed of light inside the scintillator approximately $c_{scint} = 20\ cm/ns$.

The signals from SC2 and SC4 were also used to measure the time-of-flight (TOF) of the fragment, according to the scheme illustrated in the figure 2.8.

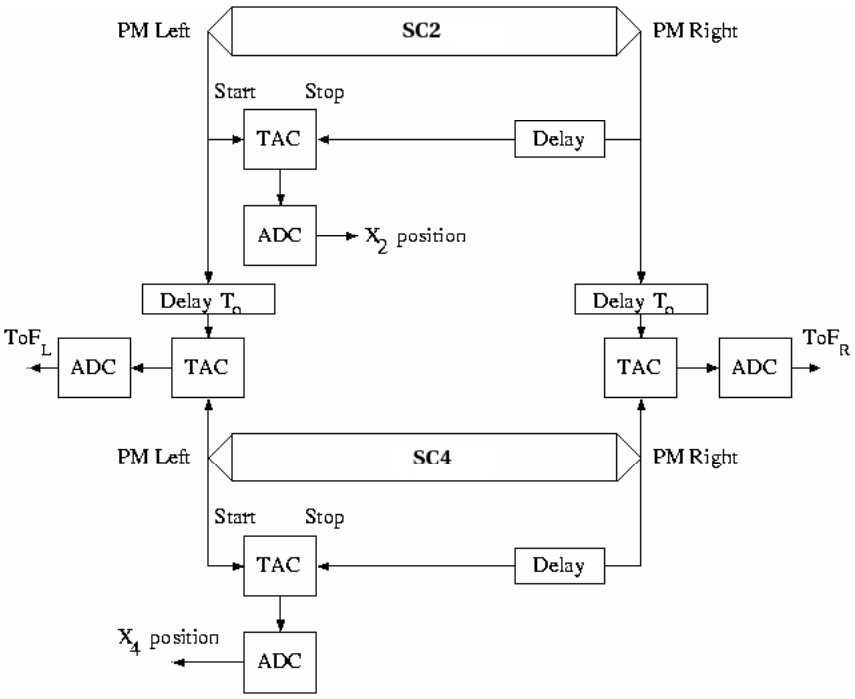

Figure 2.8: *Electronic diagram [114] for the measurement of the x-positions at the focal planes and the time-of-flight using the plastic scintillators*

The signals coming from the photo-multipliers were used as the start and stop of a time-to-amplitude-converter(TAC). The analog output of the TAC was then read by an analog-to-digital-converter(ADC). The ion passes through SC2 at time T_2 and through SC4 at time T_4, but before the signals arrive at the TAC, the output of the photo-multipliers at SC2 have to travel through a longer cable, so that the arrival times of all signals at the TAC are rather close. A time delay T_0 is chosen in such a way that $T_2 + T_0 > T_4$.

The measured time-of-flight, ToF^*, is the average of the right and left signals, ToF^*_R and ToF^*_L, opportunely transformed from amplitude to nanoseconds through the calibration factors α_R and α_L so that:

$$ToF^* = \frac{ToF^*_L \cdot \alpha_L + ToF^*_R \cdot \alpha_R}{2} = T_2 + T_0 - T_4 \qquad (2.24)$$

The actual time-of-flight, ToF, is :

$$ToF = \frac{d_0}{v} = T_4 - T_2 \tag{2.25}$$

where d_0 is the flight path and v is the velocity of the ion.

The time-of-flight is then given by:

$$ToF = T_0 - ToF^* = \frac{d_0}{v} \tag{2.26}$$

or in terms of d_0 and T_0:

$$\frac{1}{v} = \frac{T_0}{d_0} - \frac{ToF^*}{d_0} \tag{2.27}$$

Details on the calibration of the positions and the time-of-flight signals will be discussed in section 2.3.1.

2.2.2 Multi-sampling ionisation chambers

At the exit of the FRS two Multiple-Sampling Ionisation Chambers (MUSIC) [121] are installed. They are used to determine the atomic number and the trajectory of the fragments passing through. Figure 2.9 shows a schematic view of the MUSIC detector. An ionisation chamber is essentially a gas-filled container with an anode and a cathode that are kept at a given working voltage. An incident particle generates a cloud of gas ions and free electrons that depend on the speed of the incoming particle and is proportional to the square of its charge.

The MUSIC is a 600mm-long chamber of 276 x 150 mm^2 active area. The entrance and exit windows are made of thin kapton (C22-H10-O5-N2) foils each of 25μm to minimise the secondary interactions of the traversing fragments. The chamber is filled with P10 gas (90% Ar, 10% CH4) under atmospheric pressure at room temperature. The gas is continuously flowing through the chamber in order to preserve the detection qualities.

Although the anode is segmented into six parts, only the middle four are used for actual measurements, and the outer two are used to assure the homogeneity of the electric field. Each of the four anodes is 100mm long. A Frisch grid is placed 23 mm in front of the anodes in order to assure the independence of the signal induced by the electrons on the presence of the positive ions and on the distance of the fragment trajectory from the anodes.

Fragments passing through the MUSIC in different horizontal positions will induce signals on the anodes at different times. The determination

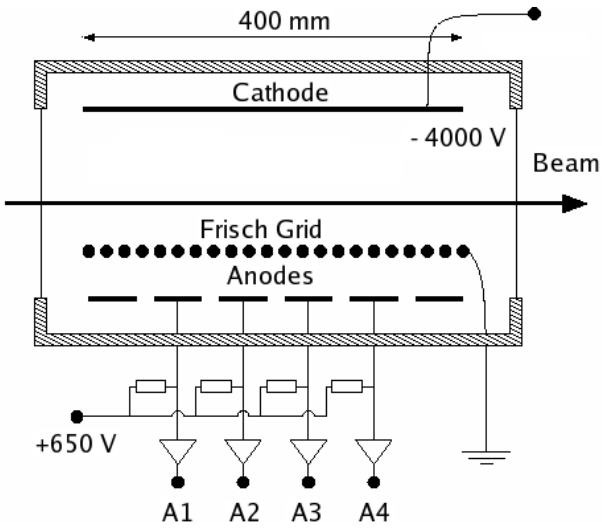

Figure 2.9: *Schematic drawing of the MUSIC used in the experiment adapted from Ref. [121]*

of these drift-times may be used to track the flight-path of the fragments. The description of the calibration of the energy losses is given in section 2.3.

2.2.3 Multiwire proportional chambers

A schematic drawing of the multi-wire (MW) chambers [108] used during the experiment is shown in figure 2.10. The MW detectors are equipped with four sets of wires in parallel planes. The distance among the wires is 2mm for anode and cathode, and 1mm for the x and y planes. The MW chambers are made of $100\mu m$ Ti or $25\mu m$ kapton windows, and are filled with a mixture of Ar, CO_2 and alcohol at atmospheric pressure. All the chambers, except the manually-mobile MW42, are housed in hermetic containers, which may be inserted into the beam line. The readout of the MW is achieved via a delay line. Each wire corresponds to a different delay time which is converted with time-to-digital converters (TDCs).

The wire structure of the MW introduces inhomogeneities in the projectile or fragment beam, therefore, MWs were used for the calibration measurements only and they were then taken out of the beam line while the measurements of the reaction products were carried out. Only the MW at the exit of the FRS were kept in the beam line.

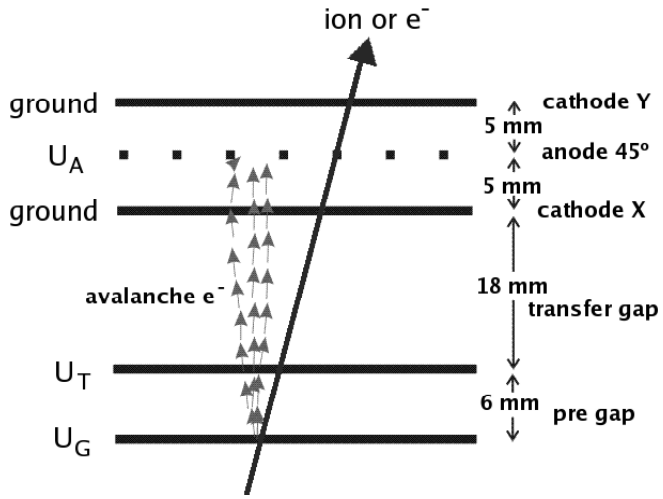

Figure 2.10: *Schematic layout of a Multi-Wire chamber. Figure adapted from [122]*

2.2.4 Data acquisition (DAQ)

The VME-based DAQ at FRS consists of a single "branch" within the GSI Multi-Branch System (MBS) framework [123]. In order to increase the data recording rate, the different tasks (readout, event building, taping etc.) are divided between two different processors - a data sender and a data receiver.

The data sender is a RIO-3 processor which resides in the FRS VME crate. The RIO-3 handles the readout of the digitisers (ADCs, QDCs etc.) and then passes on the data via TCP/IP to a Lynx-OS PC, which acts as data receiver. The latter formats the events and makes these available to analysis clients (e.g. via a remote event server) and controls taping or disk storage. For on-line visualisation of the data stream, several different software packages can be used, including PAW [124] and SATAN [125].

Two different triggers have been defined aiming at reading the standard FRS equipment detectors for the calibration and for the cross-section measurements. The acquisition was started using the scintillator SC4 and a 10Hz clock. These triggers were controlled from the acquisition trigger module in the FRS CAMAC crate.

2.3 Data analysis

In order to determine the A/Z ratio, the magnetic rigidity $B\rho$, and the velocity v (through the time-of-flight in the second part of the FRS), of the ion must be measured. Since the velocity was measured in the second half of the spectrometer, the magnetic rigidity also had to be measured in the second section of the FRS. The former quantities can only provide the ratio mass to ionic charge A/Q, according to eq. 2.1, so we need to know not only the atomic number Z, but also the ionic charge state of the particle, to define Q and to assign the correct mass.

2.3.1 Calibrations of the experimental setup of the FRS

In the present work it is necessary to calibrate the plastic scintillation detectors to obtain the horizontal position of the transmitted nuclei at the central and final image planes of the FRS, the time-of-flight (TOF) in the second part of the FRS, the effective radii of the dipoles, dispersions at F2 and F4, and the energy loss of the fragments in the ionisation chambers. In the following subsections all calibration procedures are described in detail, including the different corrections which were applied to obtain an optimum resolution.

Calibration of the plastic scintillators

The plastic scintillators allow us to determine the horizontal position of the transmitted nuclei at the central and final image planes of the FRS. This is determined by the time difference of the signals arriving at the two photo-multipliers, mounted at both sides of each scintillator. The scintillators are also used to calculate the time-of-flight in the second part of the FRS.

Position calibration

The position calibration is performed by irradiating the detector with particles over the whole range of the detector, which is achieved by defocussing the beam at the central and final focal plane. By comparing the maximum and minimum channel of the spectra (see figure 2.11) with the geometrical dimensions of the detector(220 mm at F2 and 200 mm at F4), it is possible to calibrate the signals from the detector in position, by a linear fit.

This calibration of the scintillator detectors is performed several times during the experiment to assure that the detector response had not

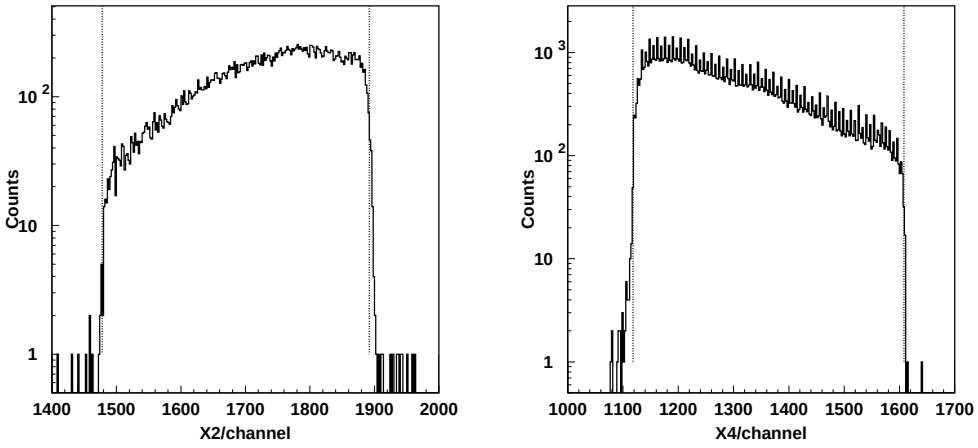

Figure 2.11: *Raw spectra from the scintillator response at F2 and F4 used for position calibration.*

changed, due to either radiation damage or to the sensitivity to the temperature in the cave of the photo-multipliers.

Time-of-flight calibration:

The time-of-flight is measured in the second half of the FRS by means of the two scintillators at F2 and F4. The ratio of the flight-path s (approximately 36 m) to the time-of-flight between the two scintillators gives the velocity of the fragments, which is needed to perform the identification.

As explained in section 2.2.1, the signals coming from the photo-multipliers are used as the start and stop of a time-to-amplitude converter(TAC) (see figure 2.8). The electronic signal generated by the TAC module of the scintillator was read by an analog-to-digital converter(ADC), and translated into a time measurement (in nanoseconds) by means of a pulse generator with a well known frequency. The right and left signals, ToF_R^* and ToF_L^*, are transformed from channel to nanoseconds through the calibration factors α_R and α_L. We used a generator with a pulse every 10 ns (see figure 2.12) in order to take several points and make a linear fit. The corresponding calibration factors are $\alpha_L = 0.01312\ ns/ch$ and $\alpha_L = 0.01299\ ns/ch$.

The delay needed to bring the signals from scintillator at F2 *after* the signals from scintillator at F4, which is the master-trigger of the acquisition

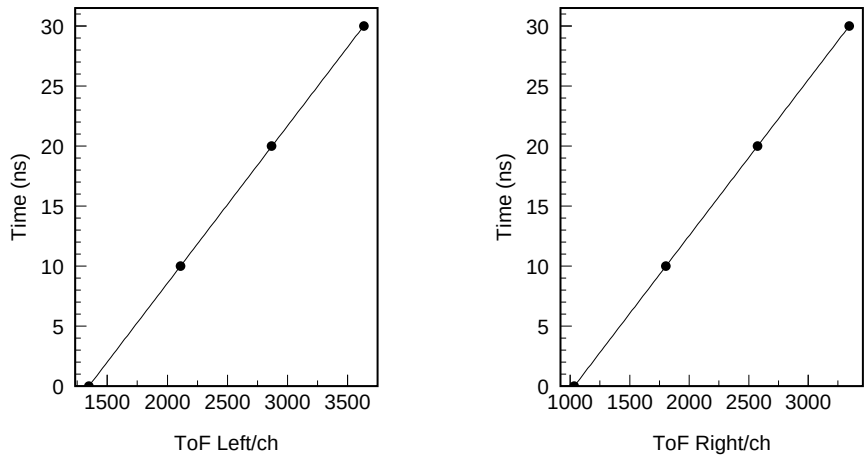

Figure 2.12: *TAC calibration for the left and right side. The difference between two pulses of the generator corresponds to 10 ns.*

system, has to be adjusted with the beam. By inserting different layers of matter into the beam line at F2, the beam was slowed down, and as a consequence, different times-of-flight were registered. The corresponding laboratory velocity was calculated with AMADEUS from the $B\rho$ applied to centre the beam for each layer of matter to obtain d_0 and T_0 by fitting equation 2.27 by a first-order polynomial.

$$\frac{1}{v} = \frac{T_0}{d_0} - \frac{ToF^*}{d_0} = a + b \cdot ToF^* \tag{2.28}$$

Calibration of the ionisation chambers (MUSIC)

The atomic number is determined by measuring the energy loss of the ions in the MUSIC chambers. The energy loss (ΔE) in matter is governed by electromagnetic interactions, and according to the Bethe theory, is directly proportional to the square of its atomic number (Z) and inversely proportional to the square of its velocity. In the case of ions one should consider the effective ionic charge of the nuclei (Q_{eff}), taking into account the possible charge states, so that $Q_{eff} = Z - n_e$, where n_e is the number of electrons. The MUSIC signal is the sum of the ionisation charge created along the trajectories in the chamber, whereby the charge state of the ion may change due to the atomic collision processes in the gas.

The signal generated by one nucleus will vary according to the distance of the trajectory of the ions with respect to the anode of the chamber due to recombination effects. The re-combination follows an absorption law, so the dependence of the energy-loss signal on the fragment position is described by an exponential function.

Therefore, to determine the atomic number, the dependence on the velocity $f_1(v)$ and the position dependence at F_4 $f_2(x_4)$, have to be corrected, and thus

$$Q_{eff} = \sqrt{\Delta E_m} \tag{2.29}$$

where

$$\Delta E_m = f(Z, v, x_4) \propto (Z - n_e)^2 \frac{f_2(x_4)}{f_1(v)} \tag{2.30}$$

Since there is a correlation between the position x_4 and the velocity, if the energy-loss signals are corrected for the $f_1(v)$ dependence, the correction function in position can be approximated by a power law, thus making the application of the correction to the data much simpler.

MUSIC energy-loss signals

As described before, the MUSICs used during the experiment have four anodes which provide four independent measurements of the energy loss of the fragment. The mean value of all four signals within one chamber provides an improved resolution in the charge measurement, and since the gas conditions within the MUSIC are the same for the four anodes, the corrections in velocity and position can be applied directly to the mean value.

Evaluation of $f_1(v)$:

The function $f_1(v)$ has been obtained from the theoretical calculations performed by using the code AMADEUS. The energy loss of a given fragment for different velocities is determined and the energies obtained in this calculation were represented as a function of β and fitted to a third-order polynomial.

If we apply the same procedure for different ions, we obtain different curves because the theoretical calculation also depends on the charge. To remove the charge dependence, we can write the velocity dependence as

$$f_1(v) = \Delta E(v_{ref})/\Delta E(v) \tag{2.31}$$

where $\Delta E(v_{ref})$ represents the energy loss corresponding to a reference velocity v_{ref}. To perform the fit, we calculate the energy loss by the beam ^{208}Pb traversing the ionisation chamber at different values of β ranging from 0.76 to 0.82. The reference velocity chosen was $v_{ref} = 23.38 cm/ns$, corresponding to the energy of 557 A MeV.

Evaluation of $f_2(x_4)$:

In order to determine accurately the position dependency of the energy loss, it is necessary to populate the full position range at F4 (see figure 2.13). This can either be done by defocusing the beam at F4, or by using a magnetic setting of the FRS where the full range at F4 is covered, so that the position dependence can be fitted to an appropriate function. This function was a third-order polynomial for both chambers.

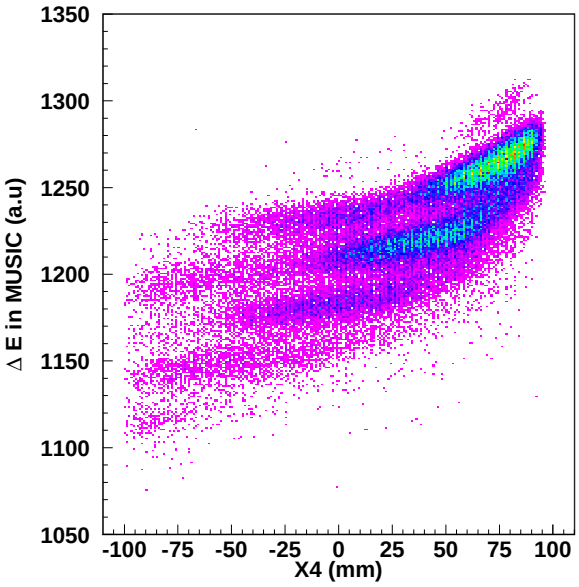

Figure 2.13: *Position dependence of the energy-loss signal in MUSIC1 for one magnetic setting of the FRS centred on ^{194}W*

As ionisation chambers are gas detectors, the density of the gas influences the magnitude of the energy loss of the fragment, as this fragment passes through the MUSIC. Since the density of the gas is modulated by the atmospheric conditions, pressure and temperature,

the energy-loss spectra have to be checked at different times during the experiment, and any shift with respect to the reference spectrum must be compensated for. As a reference, a magnetic setting of the FRS where the beam ^{208}Pb was passing through the MUSIC was selected.

Dispersions at F2 and F4

In order to measure the dispersions at the intermediate and final focal planes, we used the ^{208}Pb beam at 1 A GeV ($B\rho$ = 14.2790 Tm). After aligning the beam through the FRS axis, we measured the position of the beam at F2, and increased the magnetic rigidity from target to F2 by 0.5% steps, in order to cover the whole momentum acceptance window, monitoring the beam-position shifts to determine the dispersion by making a linear fit of ΔB as a function of x_2. An analogue procedure is carried out for the second section of the FRS. The corresponding measured values for the dispersion at F2 are $D_2 = 6.47 \pm 0.04\ cm/\%$ and $D_4 = 8.72 \pm 0.06\ cm/\%$.

Effective radii of the dipoles

The output voltages of the Hall probes used to measure the magnetic field are subject to long-term variations, as, for instance, radiation damages, and the product of B_{Hall} and ρ have to be calibrated using the beam, from which we know the magnetic rigidity independently.

The measurement of the effective radii is performed by passing the primary beam through the FRS, traversing only the SIS-window, the SEETRAM and a Nb stripper foil (60 mg/cm^2 place at S0), and centring the beam at F2 and F4. The corresponding magnetic fields of the four dipoles are registered. AMADEUS is used to calculate the magnetic rigidity of the completely-stripped beam after it has passed the three layers.

The use of the stripping foil is to reduce the fraction of incompletely stripped ions, because otherwise the charge state will not correspond to the theoretical charge of the beam. Now the values of effective radii can be determined from the relation: $\rho_i = \frac{B\rho_i}{B}$. The measured effective radii in the experiment were: $\rho_1 = 11.2578 \pm 0.0009\ m$, $\rho_2 = 11.2832 \pm 0.0009\ m$, $\rho_3 = 11.2878 \pm 0.0009\ m$, $\rho_4 = 11.2804 \pm 0.0009\ m$.

2.3.2 Isotopic identification of projectile residues

The identification of heavy neutron-rich projectile residues is a challenging task. Two issues have to be overcome to obtain an unambiguous identification of residues:

- contamination due to charge states produced inside the FRS
- loss in resolution in the energy-loss measurements ΔE with the MUSIC chambers due to stochastic changes in charge-states within the gas.

The use of a profiled aluminium degrader, placed at the intermediate focal plane of the FRS, and the combined measurement of the energy loss (ΔE) of the fragments in two MUSIC chambers with a stripper foil in between, allowed us to separate all non-bare nuclei. A detailed description of this method can be found in Refs. [16, 126].

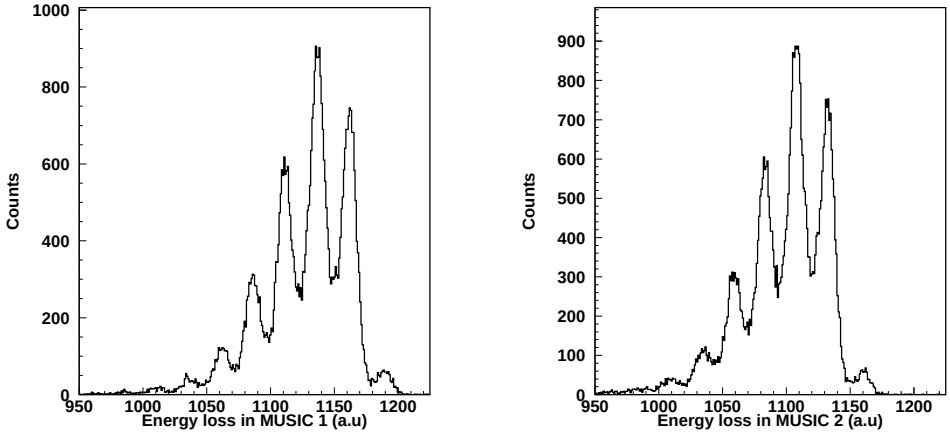

Figure 2.14: *Energy-loss spectra measured in MUSIC1 (left) and MUSIC2 (right) after applying all the aforementioned corrections, for a setting of the FRS centred on* ^{194}W

Figure 2.14 shows an example of the energy-loss spectra of MUSIC1 (left) and MUSIC2 (right) after applying all the described corrections in previous sections. As can be seen, the final resolution is not good enough for charge separation. This is due to the different ionic charge states populated by the heavy ions. The charge state of the ion can change within

the active region of the ionisation chamber, and this effect contributes to the broadening of the energy-loss signal.

In the experiment we used two ionisation chambers, and this allowed us to have two independent measurements of the energy loss and to define an effective charge, with an improved resolution.

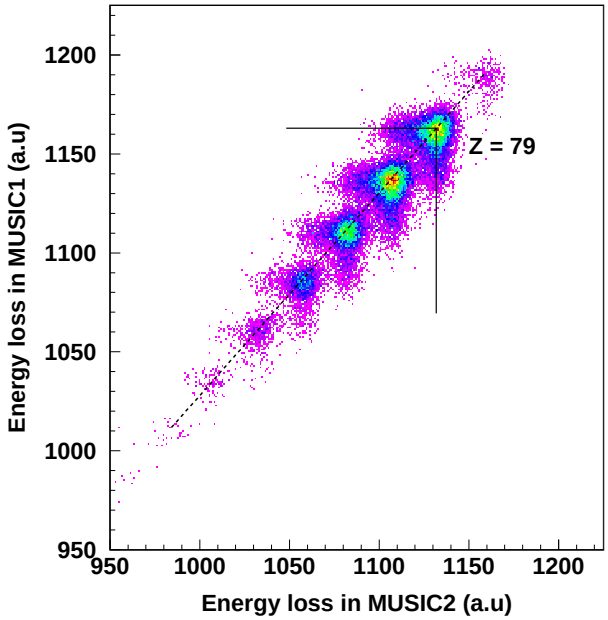

Figure 2.15: *Scatter plot of the correlation between the energy-loss signals in the two ionisation chambers for a setting of the FRS centred on* ^{194}W.

Figure 2.15 illustrates the correlation between the energy-loss signal of the two MUSICs. For each ion we can define a new value Q_{eff}^{max} which corresponds to the highest energy loss measured by any of the two chambers. Since $\Delta E \propto Q^2$, the value Q_{eff}^{max} is sensitive to changes in the ionic charge between the two chambers. The probability of one ion being fully-stripped at least in one chamber was optimised with a stripper Nb foil (260 mg/cm^2) placed in between. Thus, Q_{eff}^{max} corresponds to the atomic number Z with a maximal probability.

The observed *double-wing* pattern for each spot in figure 2.15 is due to the atomic charge distribution measured in both chambers. For each charge, the energy-loss signal in the horizontal wing corresponds to those

ions which carry no electrons in the first chamber (MUSIC1). The vertical wing corresponds to the fully-stripped ions at the second chamber (MUSIC2). The wings overlap in cases of fully-stripped ions in both chambers. A tilted line passing through the different cores corresponds to those events for which the same atomic charge was measured by the two chambers. Q_{eff}^{max} can be defined once the observed main diagonal of charges has been established. Only if the ion keeps at least one electron in the path through the two chambers can it be misidentified. Figure 2.16 shows the final resolution achieved using this method.

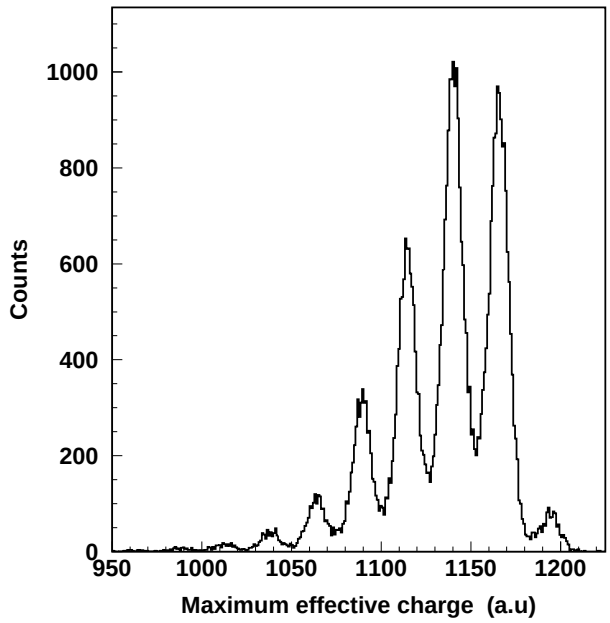

Figure 2.16: *Charge spectrum using the combined information of the two ionisation chambers. The charge resolution around $Z = 77$ is $\Delta Z = 0.47$ (FWHM)*

Additionally, we can determine the ionic charge state of a fragment within the FRS by the measuring the energy loss in the degrader. In the following section this procedure will be described in detail.

2.3.3 The energy loss in the degrader

If the magnetic spectrometer is set to select fully-stripped fragments with a given A/Z ratio, H-like fragments (that is, fragments with 1-electron) with atomic number Z and mass A - A/Z will also be transmitted, as well as He-like fragments with mass A - 2A/Z, etc. The degrader energy-loss method allows for the separation of the different charge states and for the assignment of both the values of the atomic charge Q and the atomic number Z, of the fragments passing through the FRS.

The energy loss in matter of an ion of mass A and kinetic energy E is given by

$$\Delta E = A\Delta\gamma \tag{2.32}$$

For calculations related to magnetic rigidities, it is more convenient to write this equation as follows:

$$\frac{\Delta E}{Q} = u \cdot (\gamma_1 - \gamma_2) \cdot \frac{A}{Q} \tag{2.33}$$

where γ is the relativistic factor, (the notation 1 and 2 represents the first (F2) and second (F4) stages of the FRS respectively), so that

$$\gamma_1^2 = 1 + (\frac{e_o c}{u})^2 \cdot (\frac{B\rho_1}{A/Q})^2 \tag{2.34}$$

and the value of γ_2 is given by the time-of-flight measurement. $B\rho_1$ is measured as described in previous sections, u and c are the mass unit and the speed of light respectively, and e_o is the charge unit.

The magnitude $\Delta E/Q$ is sensitive to changes of the atomic charge of the ion within the FRS, and therefore can be exploited to define the ionic charge state of a given nucleus in the FRS.

In figure 2.17 we plot the energy loss in the degrader, calculated as described above versus the effective charge measured by the combined measurement of the two MUSICs, for a magnetic setting of the FRS optimised to transmit ^{186}Lu. In the figure we see spots along four tilted lines. The spots that lie in the central tilted line are the most populated ones, and correspond to those nuclei which are fully-stripped along the whole FRS. Also small contributions of ions which carry 1-electron or even 2-electrons in the two magnetic sections of the FRS populate these spots. For a given Z value, the spots above and below the former ones correspond to those nuclei with 1-electron before the degrader and fully-stripped after and vice-versa, respectively. The 2-electron cases can also be seen in the

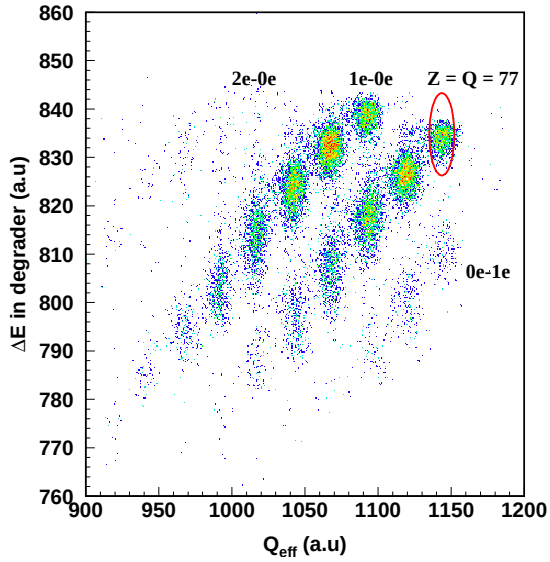

Figure 2.17: *Scatter plot of the energy loss in the intermediate degrader in relation to the energy loss measured with the two ionisation chambers Q_{eff} corresponding to an FRS setting optimised to transmit ^{186}Lu.*

plot. The most unfavourable cases when using this analysis are those nuclides with one or two electrons that do not change the charge state throughout the whole FRS. The identification in these cases fail in the assignation of the nuclear charge and also in the determination of the mass number A, but one can calculate this contribution quantitatively. In the present experiment, these events represent only 2% as calculated using the code GLOBAL [127].

2.3.4 Atomic- and mass-number identification

Once the fully-stripped ions are selected by using the method described above, the mass and the atomic number can be identified without any ambiguity. One practical way of identifying the fragments is to plot the atomic number Z against the A/Z ratio, calculated using equation 2.1.

Alternatively, the fragments can be identified by plotting the A/Z against the position at the intermediate focal plane (see figure 2.18), which allows us to separate the different isotopes by their mass.

Figure 2.19 (top) shows a two-dimensional cluster plot of the isotopes measured at two different FRS settings optimised to transmit ^{194}W and

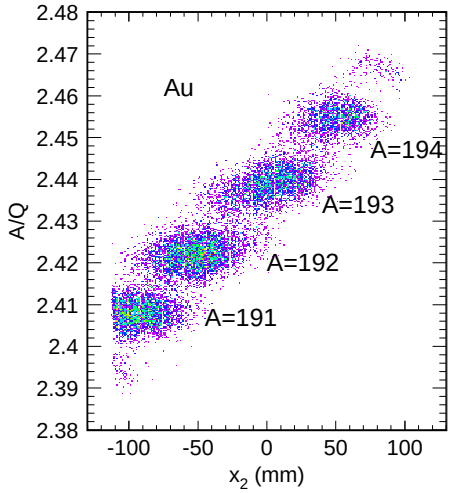

Figure 2.18: *Two-dimensional cluster plot used for the identification of different gold isotopes, measured in one FRS setting optimised to transmit* ^{188}Ir.

^{186}Lu. In this cluster plot each nucleus is represented by a spot. The high resolution achieved in this experiment can be seen in the clear separation of spots corresponding to different isotopes. The solid line in the cluster plot represents the present limits of the chart of nuclides. In the present work we were able to identify for the first time 25 heavy neutron-rich nuclei. Table 2.2 summarises the new isotopes. Figure 2.19 (bottom) shows the separation of different iridium isotopes.

The high resolution obtained after applying all the procedures described in this chapter will allow determining the cross-sections of the nuclei produced during the experiment, and the half-lives of some of them, as will be explained in the following chapters.

Table 2.2: *New isotopes identified for the first time in this experiment.*

Z	N	A
78	126	204
77	126	203
77	125	202
77	124	201
77	123	200
76	125	201
76	124	200
76	123	199
76	122	198
75	123	198
75	122	197
75	121	196
75	120	195
74	121	195
74	120	194
74	119	193
73	120	193
73	119	192
73	118	191
72	118	190
72	117	189
71	115	186
71	114	185
70	112	182
70	111	181

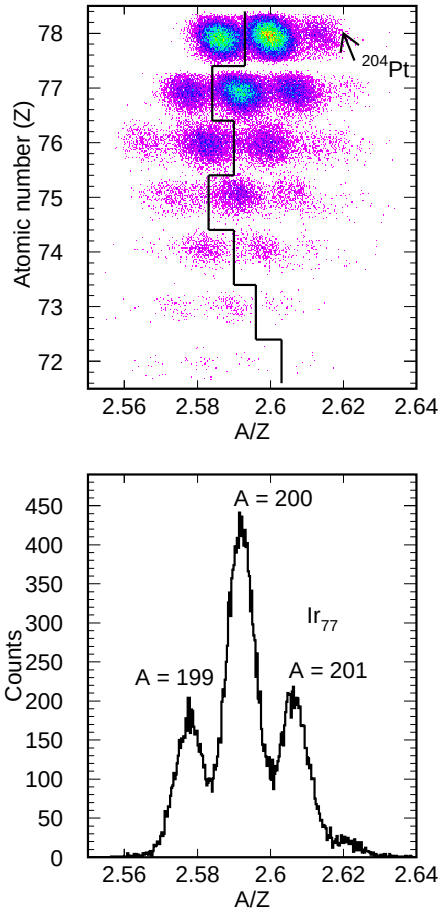

Figure 2.19: *Top:Two-dimensional cluster plot of Z vs. A/Z, containing the data corresponding to two different settings of the FRS optimised to transmit ^{194}W and ^{186}Lu. The solid lines represent the present limits of the chart of nuclides. Bottom: Projection of the A/Q ratio for the iridium isotopes. A mass resolution $A/\Delta A(FWHM) \approx 250$ for $A \approx 200$ is achieved.*

Chapter 3

Production Cross-Sections

The production cross-sections are determined by three independent magnitudes: the production rate or yield of single isotopes transmitted at the final focal plane n_f, the beam intensity or total number of impinging projectiles n_p, and the number of atoms in the target n_t.

$$\sigma_{A,Z} = \frac{n_f}{n_p \cdot n_t} \tag{3.1}$$

The number of target atoms per unit area n_t is given by

$$n_t = \frac{N_o \cdot t}{A_t} \tag{3.2}$$

where N_o is Avogadro's number, t is the target thickness in mg/cm^2 and A_t is the mass number of the target.

The procedure explained in the previous chapter allows us to identify unambiguously the nuclei produced in the reaction on an event-by-event basis. The experimental setup and the analysis procedure introduce restrictions to the isotopic identification. Different corrections have to be applied to the measured yields in order to obtain the actual yields of each nucleus. In the following sections, the determination of all these magnitudes and corrections applied will be explained in detail.

3.1 Beam intensity normalisation

The intensity of the primary beam is measured by means of the beam monitor SEETRAM which provides information on the current induced by the beam particles. In order to obtain the correct normalisation for the determination of the production cross-sections, the SEETRAM signals have to be calibrated to transform the measured SEETRAM current into

the number of incident particles. The calibration of the SEETRAM has to be performed in every experiment, since its response may change in the long-term due to irradiation damages.

In order to calibrate the SEETRAM we used a plastic scintillator which directly counts the number of traversing ions. The beam intensity was reduced below the detection limit of the SEETRAM (10^{-12} A) and subsequently increased in small steps, up to the upper limit of the linear operation of the plastic scintillator detector (approximately 10^5 particles per second), to obtain a sufficient number of calibration points.

Figure 3.1 shows an example of the SEETRAM spectrum measured during the experiment. The peaks in the spectrum correspond to the spills of the ^{208}Pb ions extracted from the SIS. The beam spills have a typical length of $\approx$ 2 s and a repetition cycle of $\approx$ 10 s. The SEETRAM has a constant offset (as can be seen in figure 3.1) created by a positive offset current produced by the current digitiser, which allows us to identify unwanted noise signals. For a correct calibration of the SEETRAM this offset has to be properly determined, subtracted and hence eliminated. The offset can be determined from the pause between spills in the SEETRAM spectrum. After the offset subtraction, the correlation between the SEETRAM counts and the number of particles measured by the scintillator allows us to determine the calibration factor f.

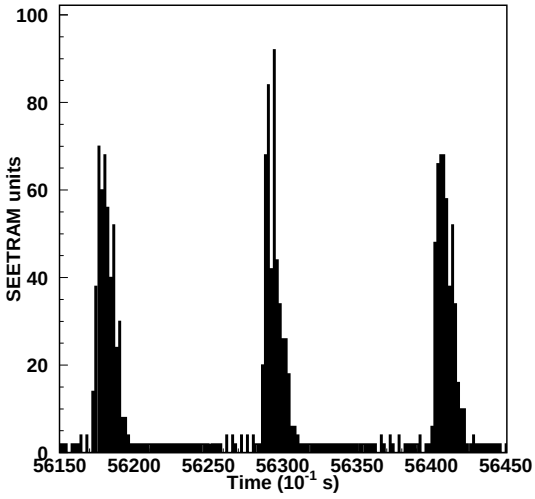

Figure 3.1: *SEETRAM counts over time, in a given time interval during the experiment*

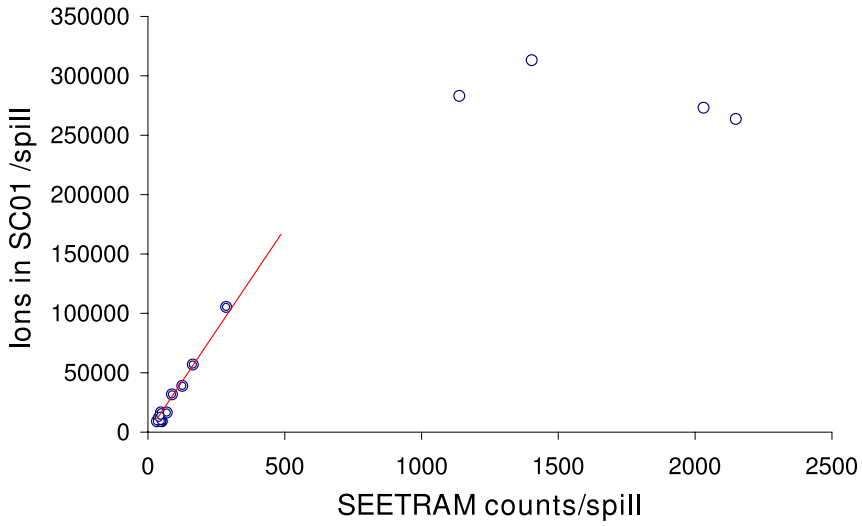

Figure 3.2: *Number of ^{208}Pb ions measured in the scintillator plotted against the number of SEETRAM counts. Each data point corresponds to the counts accumulated during one spill. The line shows the linear fit to the data in the range below 500 SEETRAM counts/spill*

The total number of impinging particles is given by

$$n_p = N_{SEETRAM} \cdot f \cdot 10^{10} \cdot sensitivity \tag{3.3}$$

where $N_{SEETRAM}$ is the total number of SEETRAM units with the background offset already subtracted. As it was explained in chapter 2, the SEETRAM sensitivity ranges from 10^{-4} to 10^{-10} A.

Figure 3.2 shows the SEETRAM counts in relation to the number of particles detected by the scintillator SC01 per spill. In this figure we can appreciate that there is a region in which the correlation is linear and then there comes a change in the slope which indicates a saturation of the scintillator. The SEETRAM calibration factor is determined by the slope of the linear region. The SEETRAM calibration factor obtained in the experiment was $f = 364 \pm 36$ ions/SEETRAM counts.

3.2 Yield corrections

In order to determine the actual number of fragments produced, some corrections have to be applied to the measured yields, $Y_{measured}$, since some of the *real counts* are lost in the setup and data analysis. One of these effects is the attenuation (due to nuclear and electromagnetic-dissociation reactions), of the residue flux produced in the target, and in the different layers of matter present in the beam-line setup. The measured yields correspond only to ions fully-stripped through the FRS, as the different ionic charge-state combinations are excluded when identifying unambiguously the nuclei in mass and nuclear charge. All combinations but 0e-0e must be included to determine the actual yield. Also, the acquisition and reaction rates will determine a certain *dead-time* that has to be included in the corrections of the yield.

Thus, the actual number of fragments produced is determined via the formula

$$n_f = Y_{measured} \cdot C_\tau \cdot C_1 \cdot C_2 \cdot C_3 \tag{3.4}$$

where C_τ is the correction factor due to the acquisition dead-time, C_1 and C_2 are the correction factors due to losses for the projectile in the target and for the fragments in the different layers of matter present in the beam-line setup respectively, and C_3 is the correction factor due to ionic charge state distributions in the experimental setup. If the transmission T through the FRS is not 100 %, the transmission correction factor $C_T = 1/T$ has also to be included in the calculation of the actual yields. In the following sections all these corrections will be described in detail.

Dead-time correction

The dead-time is defined as the time elapsed after one event is registered by the detection system in which it is not able to reveal another coming event. In each event readout we register the number of triggers, that is all signals, and the number of accepted triggers, that is the number of the fully-processed ones. The ratio between these two magnitudes serves as a measure of the overall dead-time of the detection system.

$$C_\tau = \frac{N_{free-triggers}}{N_{accepted-triggers}} \tag{3.5}$$

The dead-time values are determined by the acquisition rate, 2 - 3 10^3 Hz, and the number of real events, which depends on the characteristic production rates of the explored isotopic region. When the

production rates are relatively high, the dead-time values can be kept below 30% by adjusting the beam intensity. During the experiment the typical values of the dead-time range from 5% for the most exotic isotopic region and 30% for the regions close to the projectile.

Transmission through the FRS

As it was explained in chapter 2 , the FRS is limited in momentum acceptance by $\pm 1.5\%$ and in angle by ± 15 *mrad*. The transmission of a given nucleus at certain energy is defined by these two factors and the position of the fragment distribution at the intermediate and final focal plane.

The typical angular distribution of the measured fragmentation residues in this experiment is below 5 mrad. This means that the transmission is close to 100 %. This effect will only be important for nuclei that are transmitted to the edges of the focal plane positions. This limitation is overcome in most of the cases by the overlap of different magnetic settings of the FRS and the reconstruction of the longitudinal velocity distributions, by comparing channel by channel all velocity distributions measured for a given nucleus and taking the maximum value.

The longitudinal velocity of a given nucleus, once it has been identified unambiguously, can be deduced from its positions at the intermediate focal plane F2 by

$$v = \beta\gamma = \frac{e}{uc}\frac{(B\rho_0)_2 \cdot (1 + \frac{x_2}{D_2})}{A/Z} \tag{3.6}$$

Since the reaction cross-section does not vary in accordance with the small variation of energy that the beam experiences (due to the finite thickness of the target material), the position where the fragment is formed is thus, on average, the middle of the target. The fragment velocity is then calculated in the middle of the target with the help of AMADEUS in the reference frame of the beam, using the Lorentz transformations.

Figure 3.3 shows the velocity distribution in the projectile frame for the nucleus ^{206}Pb. The different areas correspond to the normalised data recorded in different magnetic settings, each contributing to the reconstruction of the whole velocity distribution.

Only for the cases in which the overlapping is not enough to reconstruct the full velocity distributions, are the fragment position distributions at the intermediate and final focal plane fitted to a Gaussian to obtain the transmission T, and the transmission correction factor $C_T = 1/T$ included in the normalisation of the yields. This procedure gives an overall

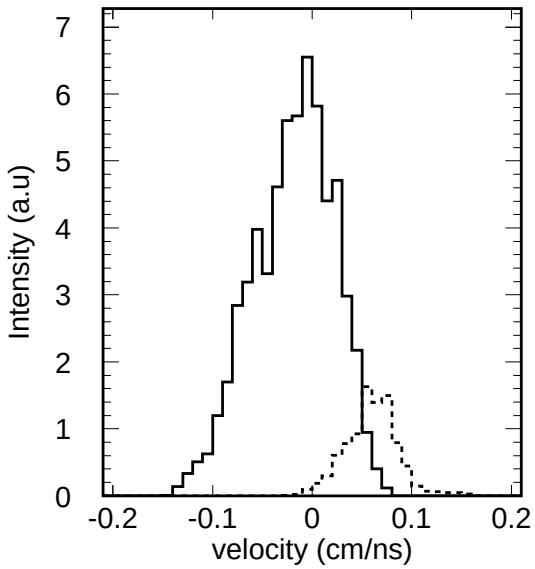

Figure 3.3: *Velocity distribution in the middle of the target, in the frame of the projectile, for the nucleus ^{206}Pb. The different areas correspond to the velocity measured in different FRS magnetic settings. Overlapping these measurements allows us to reconstruct the whole velocity distribution.*

uncertainty of 20% for the transmission correction factor.

Corrections due to secondary reactions

The measured yields have to be properly corrected for the beam attenuation and the secondary nuclear reactions produced in the target and in the different materials present along the beam-line.

Secondary reactions for the primary beam inside the target lead to a reduction of the counting rates. The correction for the fragment residues will include only losses of the fragments due to the secondary reactions, since the magnetic rigidities of the products of secondary reactions at the intermediate focal plane are, in general, outside the acceptance of the second stage of the FRS, so these products will not be transmitted to the final focal plane and thus will not be detected.

Losses for the projectile in the target (C_1) as well as for the fragments in the different layers of matter (C_2) present in the beam-line setup (see appendix B, C and D), were determined calculating the total nuclear reaction cross-sections according to the microscopic model of Karol

described in Ref. [128], so that

$$C_1 = \frac{1}{1 - P_1} \tag{3.7}$$

$$C_2 = \frac{1}{1 - P_2} \tag{3.8}$$

being P_1 and P_2 the reaction probability in the target and the different layers of matter in beam-line setup respectively.

The error of the corrections of secondary reactions in target and degrader is directly dependent on the error of the total-reaction cross-section formula which corresponds to 10% [128].

Figure 3.4 shows an example of the correction factors applied, calculated using a 1g target and 4.4g degrader, including all the detectors present in the experimental setup, for different elements. The main contribution to this correction factor is due to the plastic scintillator SC2 and the degrader, situated at F2, which amounts to about 50%.

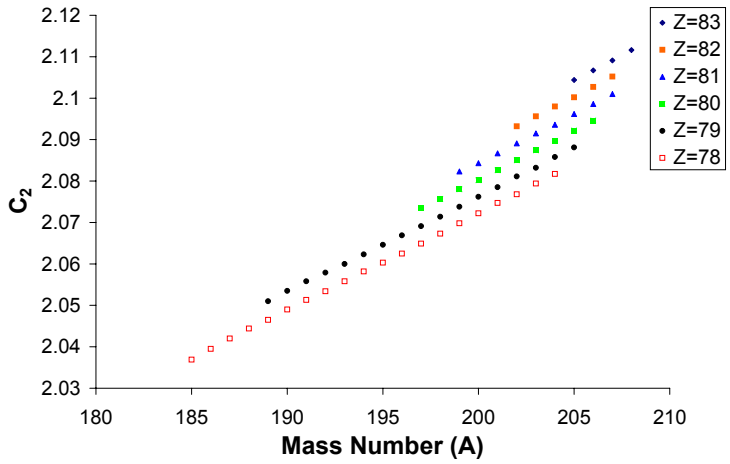

Figure 3.4: *Correction factor C_2 due to secondary reactions in the different layers of matter present in the beam-line setup, calculated for different isotopes of Pt, Au, Hg, Tl, Pb and Bi.*

Corrections due to ionic charge states

As was explained before the measured yields correspond to the nuclei fully-stripped along the FRS. All charge-state combinations different to 0e-0e must be included to determine the actual yields.

This can be done by determining the survival probability for the fully-stripped fragments P_{0-0}, and thus the correction factor C_3 is given by

$$C_3 = \frac{1}{P_{0-0}}. \tag{3.9}$$

The GLOBAL [127] calculation contains a refined parametrisation of charge exchange cross-sections depending on the target, projectile, energy and electronic shells. A calculation was done for the reaction $^{208}Pb(1AGeV)+Be$ including all the detectors present in the experimental setup, and the yields of each fragment were corrected accordingly (see figure 3.5). The uncertainty introduced by this correction amounts to 5%.

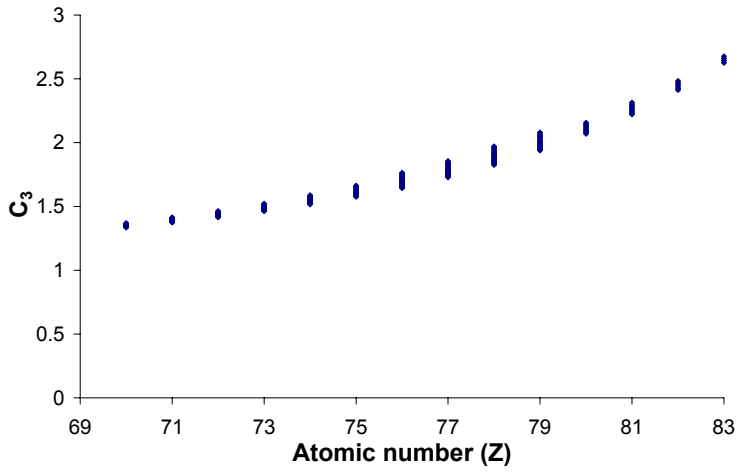

Figure 3.5: *Correction factor C_3 due to ionic charge state distributions in the experimental setup. Each data point in the plot corresponds to the calculation for a given nucleus (A,Z) using a 1g target and 4.4g degrader, including all the detectors present in the experimental setup*

3.3 Experimental results

All the fragment products measured in the present work are represented in the chart of nuclides in figure 3.6. They cover the region of heavy neutron-rich nuclei around the neutron closed-shell N = 126, with elements ranging from Yb to Bi. Solid lines in the figure indicate the present limits of the chart of nuclides, and dashed lines denote the limits of the known half-lives.

In the present work we were able to synthesise and measure the production cross-sections of more than 190 heavy neutron-rich residues, 25 of which were produced for the first time.

The tables in Appendix A list the data of the measured cross-sections together with the absolute errors (including both statistical and systematical uncertainties).

The statistical uncertainty is determined by the width of the Poisson distribution $\sqrt{N}$ of the accumulated statistics. The statistical uncertainty was below 10 % for all the fragments analysed. The uncertainty associated with the different corrections applied for the correct determination of the cross-sections, that is, the calibration of the SEETRAM counts, transmission correction, correction for secondary reactions and charge states, have been pointed out through the discussion of each one of them.

The relative uncertainty of the cross-section is the quadratic sum of the relative uncertainties of the different components, statistical errors and systematic errors.

3.4 Discussion of the experimental results

Figure 3.7 shows a more detailed survey of the fragment residue production, showing the isotopic production cross-sections measured and compared with the EPAX [47] parametrisation and the COFRA [16] analytical calculations.

EPAX is an empirical parametrisation of the fragmentation cross-sections based on experimental data. The EPAX parametrisation was developed based on the fragmentation reactions of medium- to heavy-mass projectiles.

In order to give an overview of the predictive power of EPAX in the region of the heavy neutron-rich nuclei, the calculated isotopic distributions are compared with the measured data (see figure 3.7). The EPAX predictions show a good overall agreement with the experimental data, however, the production cross-sections predicted for the most neutron-

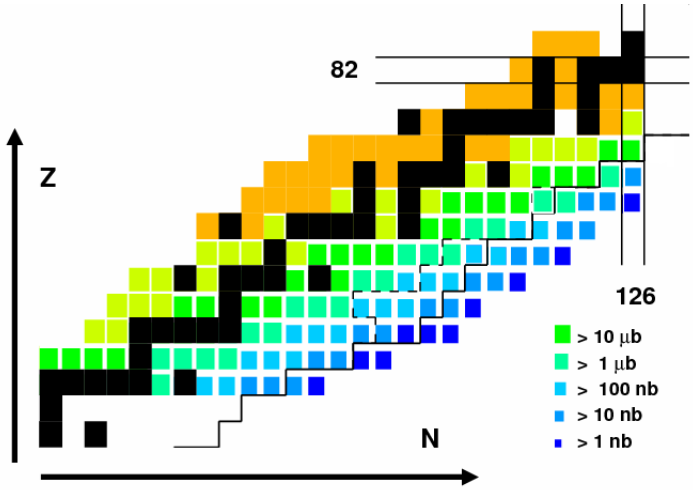

Figure 3.6: *Measured production cross-sections of the fragments residues in the reaction ^{208}Pb (1 A GeV) + Be. Solid line represents the present limits of the chart of nuclides and dashed line the limits of known half-lives.*

rich nuclei appear to be overestimated. The present data can be used to improve this parameterisation.

We also compared the measured data with the cold-fragmentation analytical calculations of COFRA code, based on the abrasion-ablation model [48]. In cold-fragmentation reactions only protons are removed from the projectile, and the excitation energy of the formed fragment is so low that no neutron evaporation follows the fragmentation.

The COFRA calculations reproduce the experimental data much better than the EPAX parameterisation, especially for the isotopes of the lighter elements tantalum, hafnium, lutetium and ytterbium.

The EPAX parametrisation is widely used to predict the fragmentation cross-sections in the regions for which experimental data is still not available. From our work we conclude that EPAX fails in reproducing the experimental data for the most neutron-rich nuclei, whereas COFRA gives more realistic predictions, and is therefore a safer way of predicting the production cross-sections.

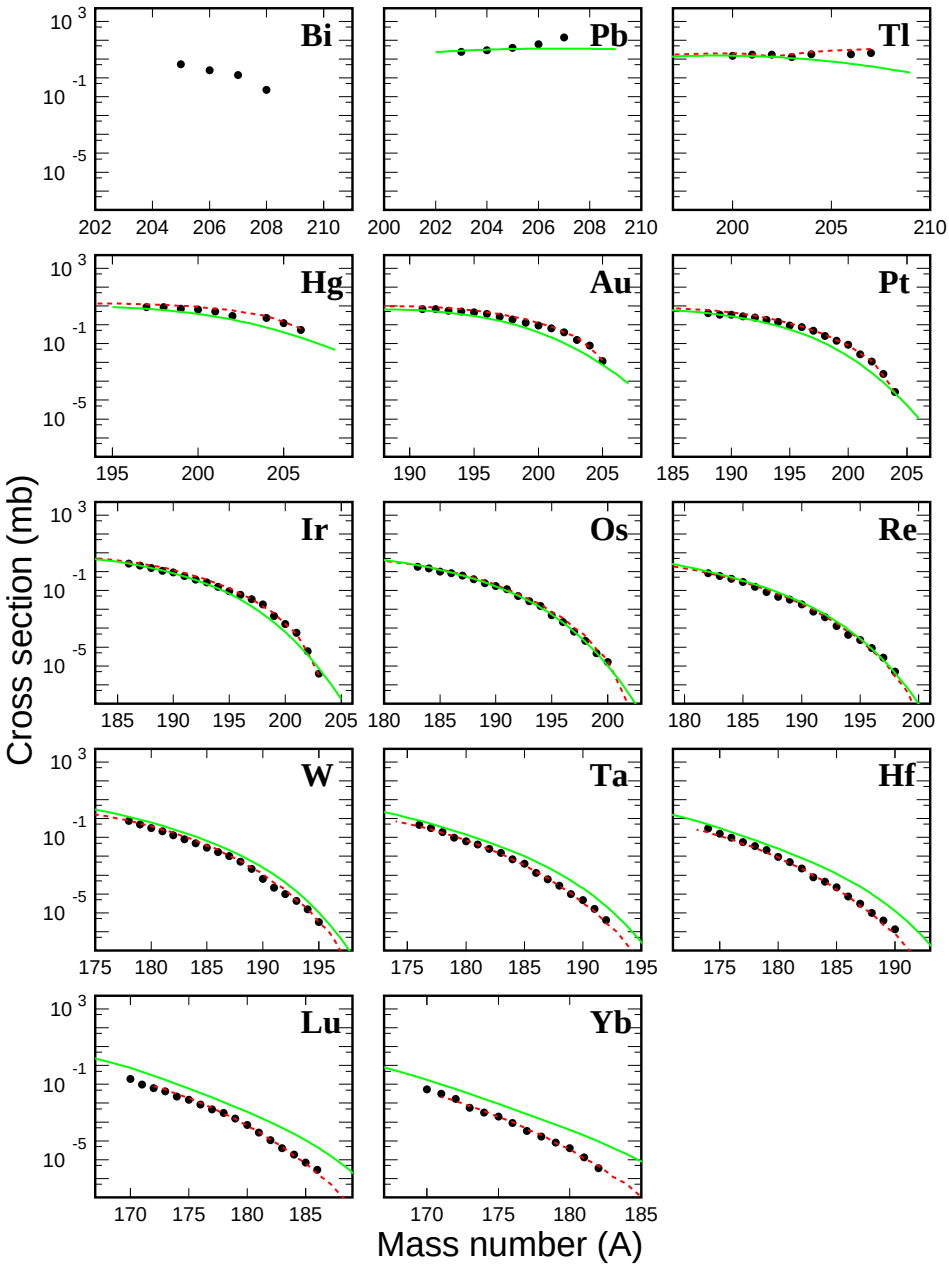

Figure 3.7: *Measured isotopic production cross sections of fragments residues produced in the reaction ^{208}Pb (1 A GeV) + Be, compared with the EPAX parametrisation (solid line) and the COFRA calculation (dashed line)*

3.5 The proton-removal channels and their implication in astrophysics

The use of fragmentation reactions allows for the production of a large variety of radioactive beams. The fragmentation reactions present large fluctuations in the N/Z value and excitation energies of the pre-fragments. These fluctuations can populate the *proton-removal channels*. In these reaction channels the projectile only loses protons in the fast nucleon-nucleon interaction, while the excitation energy is below the particle evaporation threshold. The limited energy that characterises these channels owns this process the name of cold-fragmentation. These are the most neutron-rich nuclides one can observe by using the experimental procedure described in this work, if one does not considers nucleon-exchange reactions, which occur with rather low cross-sections in very peripheral nucleus-nucleus collisions [129]

The measured proton-removal cross-sections in the experiment are plotted in figure 3.8 including a comparison with EPAX predictions and COFRA. As can be seen, the COFRA analytical code succeeds in reproducing the available data.

The experimental cross-sections were also compared with different target/projectile combinations using experimental data of previous measurements available in literature. In the figure 3.9 it can be observed that the data for the ^{208}Pb does not show any characteristic change with respect to other targets used. The same effect is observed when comparing reactions induced by different heavy ions over the same target material. Actually, all the results shown are compatible within the error bars. Therefore we can conclude that at this energy regime the target/projectile combination does not influence appreciably the production of the proton-removal channels.

When using a ^{208}Pb beam, the use of cold-fragmentation reactions allows for production of neutron-rich nuclei along the neutron closed-shell N=126. The study of the properties of the nuclei in this region holds a double interest: on the one hand it is important for the understanding of the astrophysical r-process close to the waiting-point A = 195, and to reproduce the abundance patterns, and on the other hand, we can study the robustness of the closed shell N=126 far below the doubly magic ^{208}Pb and the evolution of collective structures and shapes. The problem with this region is that there is almost no information available and the limits of the known isotopes lie very close to stability. However, as we have shown in the present work, the cold-fragmentation reactions represent a well-

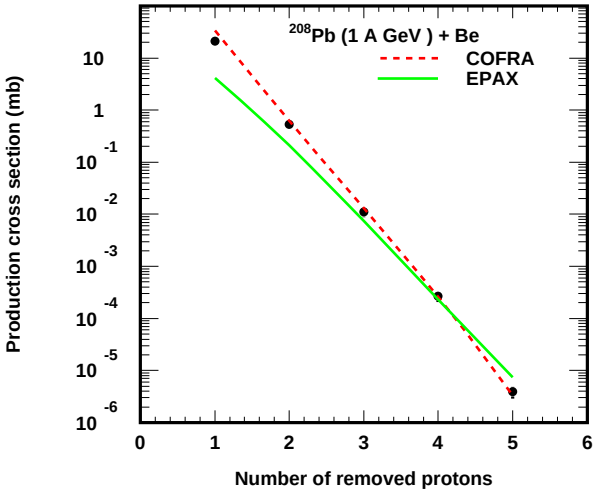

Figure 3.8: *Production cross-sections of the proton-removal channels measured in the reaction ^{208}Pb (1 A GeV) + Be, compared with the EPAX parametrisation (solid line) and the COFRA calculation (broken line)*

suited reaction mechanism for production of heavy neutron-rich nuclei. In the present work we were able to synthesise for the first time 25 heavy neutron-rich nuclei, extending the limits of the chart of nuclides. These experimental data represent a starting-point from which to design and schedule further experiments with these nuclei.

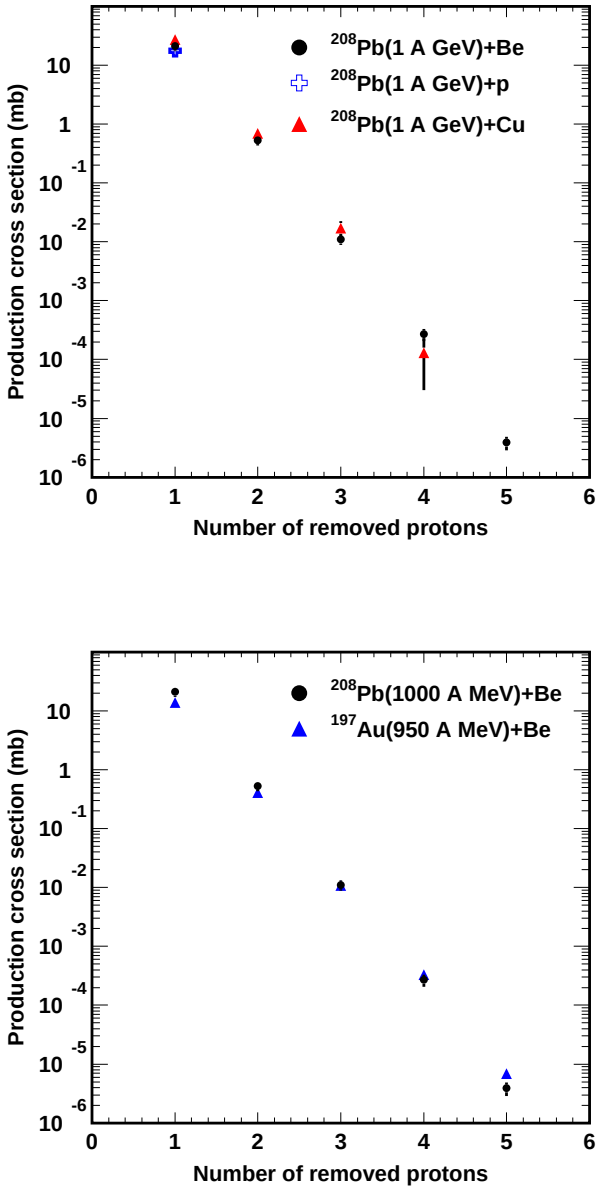

Figure 3.9: *Production cross-sections of the proton-removal channels measured in several heavy-ion reactions. Top: ^{208}Pb (1 A GeV)+Be (dots, this work), ^{208}Pb (1 A GeV)+Be (cross) [130], ^{208}Pb (1 A GeV)+Be (triangles) [131]. Bottom:^{208}Pb (1000 M GeV)+Be (dots, this work), ^{197}Au (950 A MeV)+Be (triangles) [132].*

Chapter 4

Active stopper and implantation technique

The main goal of the experiment was to determine β-decay half-lives of the new heavy neutron-rich nuclei produced. The half-lives of the nuclei were determined from the time correlations between the implantation time of the identified fragments and the subsequent β decays.

The ions at tens of $A \cdot MeV$ were implanted in an active stopper; a highly-pixelated Si detector stack which allows for the correlation in time and space of the signal from the implanted ion with the subsequent signal produced by the β-decay.

The use of a monoenergetic degrader at the FRS provides a horizontal dispersion and a narrow range distribution of fragments in the active stopper. The narrow range of fragments increases the implantation efficiency and allows to catch several exotic nuclei in a thin active stopper ($< 1\ mm$). The horizontal dispersion allows us to take advantage of the high pixelation of the active stopper to avoid multiple implantation of nuclei in the same pixel.

4.1 Experimental setup for β half-life determination

The experimental setup is schematically shown in Figure 4.1. A technical drawing of the setup can be found in Appendix D. The different nuclei transmitted through the FRS reach the final focal plane at energies that range from 500 to 600 A MeV. In order to measure β-decay half-lives the selected nuclei have to be implanted into an active stopper or catcher, which serves as both a fragment implantation target and a

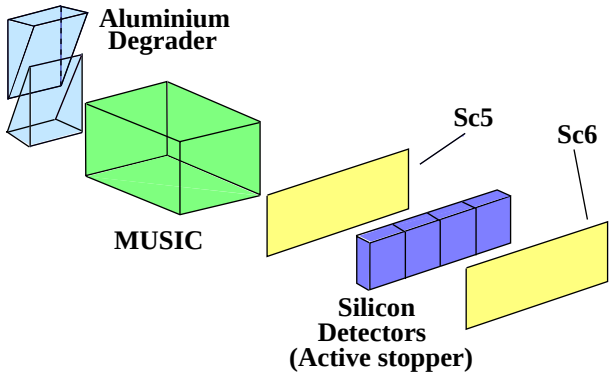

Figure 4.1: Detection setup for fragment-β time correlations

monitor of the β-decay activity. In order to be able to implant the nuclei into the active stopper they are slowed down using a variable-thickness aluminium homogeneous degrader. The active stopper consists of a stack of four double-sided silicon strip detectors (DSSD) of 1 mm thickness, providing enough depth of silicon for the implantation of several species and for the observation of the β decays. A monoenergetic degrader in the intermediate image plane of the FRS was used in order to obtain a narrow range distribution in the active stopper, and to illuminate as many pixels as possible to avoid multiple implantation of nuclei in the same pixel. Two plastic scintillation detectors were placed both in front of and behind the catcher, the first one served to check the horizontal position correlation with the strip detectors, and the second one served as veto for the implantation. In addition, an ionisation chamber was inserted into the beam-line to eliminate secondary reactions induced in the degrader, however it experienced technical problems during the experiment and therefore could not be used in the analysis.

4.2 Active stopper

4.2.1 Double-sided silicon strip detectors (DSSD)

The active stopper used in the experiment consists of a stack of 4 Micron Semiconductor Ltd [133] W(DS)-1000 5 cm x 5 cm double-sided silicon strip detectors, each of 1 mm thickness. Silicon detectors can be described as *pn* junction diodes, operated with a reverse bias voltage that forms a sensitive region depleted of mobile charge carriers, in order to allow the collection of free charge carriers generated by radiation.

Figure 4.2: Picture of the stack of 4 DSSD mounted into the vacuum chamber

The motion of a carrier (an electron or a hole), produced by ionisation inside a silicon detector, can be described by the equation

$$\nu = \mu(E) \cdot E \tag{4.1}$$

where ν is the carrier velocity, E is the electric field and μ is the mobility, that depends on the electric field. The negative bias increases the magnitude of the electric field across the depletion layer, which serves both to improve the charge collection as well as to decrease the time needed for the electrons and holes to reach the readouts (i.e the pulse duration). The current signal induced by a moving carrier is fed into the electronic chain formed by a preamplifier, that provides a gain, followed by a shaper, which tailors the overall frequency response for optimum noise performance, and limits the pulse length to accommodate the signal rate. To add position sensitivity, these detectors are highly segmented, that is, the readouts are divided into 16 strips of 3.12 mm pitch in both the front and back side.

In order to minimise the noise, the DSSDs were placed into a vacuum chamber. The preamplifiers were placed outside of the vacuum chamber and were connected to the DSSD detectors through 15 cm of twisted-pair cables (see figure 4.2).

4.2.2 Electronics

One of the challenges in designing the electronics for implantation-β-decay correlation experiments is the large difference between the two types

of events. A fragment implantation may deposit between 3 and 5 GeV of energy into the DSSD, while a β particle deposits less than 4 MeV. In the experiment we used single-output preamplifiers coupled with high-gain shaping amplifiers. As a consequence, the high-energy implantation events fell outside the maximum input voltage range of the ADCs and were recorded as overflow events. The high-gain signals were used to detect the β-decay events.

From each of the 4 DSSD, we read 24 signals coming from the 16 horizontal x strips and 8 vertical y strips. These signals were used to measure the deposited energy of the electrons coming from the β-decays and to obtain a fast signal to trigger the acquisition. We used 8 *GANIL 256 charge preamplifiers* [134] of 16 channels, with a conversion gain of 2 mV/MeV and $\tau_{fall} = 200\mu s$, which were connected to the amplifiers for further amplification and shaping of the signals. There are two outputs per channel. The fast outputs feed into constant-fraction discriminators (delay = 8 ns, fraction = 30%) and the energy outputs (800 ns peaking time, negative polarity, 300 ns delay). We used two types of amplifiers: 5 CAEN Model N568B [135] amplifiers with 16 channels for the energy signals of all Si detectors and the time signals of Si1 and Si2, and 4 EMERON amplifiers with 4 channels for the time signals of Si3 and Si4.

The 96 energy signals coming from the 4 DSSD were sent via 30m of twisted-pair cables to three ADC CAEN Model V785 [136] with 32 channels. The amplified fast signals coming from the vertical strips of the 4 DSSD were sent to 4 leading-edge discriminators (model TR8000 DVEE-GSI) with 8 channels. The β trigger resulted from an OR of the logic outputs of the leading edges, which means that any signal above the threshold in at least one vertical strip triggers the acquisition. A schematic diagram of the signal-processing system is shown in appendix E.

4.2.3 Trigger logic for implantation and decay events

Standard FRS data acquisition (DAQ) was used in the present experiment. The FRS CAMAC Crate and the USER VME crate included in the DAQ were equipped with a GSI Trigger Module [137] which controlled the hardware readout timing cycle.

Two different triggers have been defined for the implantation and decay events, aiming at:

- reading the detectors involved in checking the implantation of the nuclei in the Si detectors

- reading the detectors dealing with the decay of the implanted nuclei.

In the implantation trigger, the acquisition was started using the scintillator SC4, so that each time a signal was detected in this scintillator, the general acquisition starts and reads all FRS detectors, the silicon detectors, and veto scintillators. In the decay trigger, any signal above the threshold in at least one vertical strip triggers the acquisition, which reads only the silicon detectors. All these triggers are controlled from the acquisition trigger module in the FRS CAMAC crate.

4.2.4 Energy calibration

The region of the space-charge electric field in the DSSD is depleted of charge carriers that can participate in the conduction of a current, thus it is highly resistive. With the application of a reverse bias across the Si detector, the space-charge distribution is enhanced, the electric field is made stronger, and the depletion region grows. In order to determine the optimal bias, we used a triple alpha source made of ^{239}Pu, ^{241}Am and ^{244}Cm ($E_\alpha = 5148.85\ keV$, $5478.38\ keV$, and $5794.88\ keV$ respectively), and we determine the width of the α peaks for each bias applied.

The average energy needed to create an electron-hole pair in silicon is 3.62 eV. Thus, for a given deposited energy in the detector, many charge carriers are available to generate a signal in the silicon detector, reducing the statistical fluctuation of the signal, and as a consequence giving a good final energy resolution. Figure 4.3 shows an energy calibration spectrum for one of the silicon strips. The three peaks correspond to the three α energies of the source.

Each peak in the resulting energy spectra of the 96 strips was individually fitted with a Gaussian function. The widths of the three α peaks are around $\sigma = 30\ keV$ as shown in figure 4.3, and similar values are obtained for the rest of the silicon strips. Using the result of the fits to these spectra, energy calibrations were made using linear regression of the three points given by the three α peaks.

By measuring the width of the three α peaks for different bias voltage values applied, it is possible to determine the optimal bias as the one which gives the smallest energy dispersion. The bias applied in each DSSD and the corresponding leakage currents are summarised in table 4.1 . Further details can be found in Ref [138].

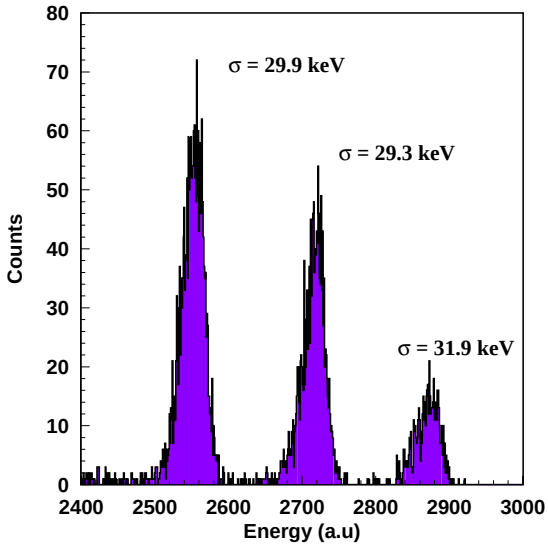

Figure 4.3: Energy calibration spectrum using a 3α source made of ^{239}Pu,^{241}Am and ^{244}Cm, corresponding to one strip of the Si3. The emission energies of the αs are $E_\alpha = 5148.85keV$, $5478.38keV$, and $5794.88keV$ respectively. The width obtained from the fit of each peak is presented in the plot.

Table 4.1: *Optimal bias and leakage currents determined for each silicon detector*

Detector	Bias (V)	Leakage current (nA)
Si1	160	570
Si2	190	520
Si3	210	580
Si4	210	560

4.2.5 Energy threshold

In order to check the detector response for the detection of β particles, we used a β source of ^{90}Sr. ^{90}Sr has a short-lived daughter isotope of ^{90}Y. These radioactive isotopes have maximum β decay energies of 0.546 and 2.283 MeV, respectively [139].

Figure 4.4 (upper panel) shows a typical energy spectrum measured for one strip with the β source. A large peak referred to as the 'pedestal' is evident in the energy spectrum. This peak occurs when the strip in question did not fire, but another strip triggered the event. The observed pulse height of the non-triggered strip corresponds to the ADC offset, that ideally would be a δ function. In reality, the pedestal is a Gaussian peak with a width that directly reflects the noise in the electronics.

For comparison we present the energy spectrum obtained at the beginning of the experiment with no radioactive source present (figure 4.4 bottom). In this case the acquisition was triggered every 0.1s by a running clock. In this case the width and shape of the pedestal is different to the one with a β source due to the different trigger definition. Table 4.2 summarises the upper energy limit of the pedestal for each strip. This value represents the lower limit or threshold for energy detection. Any β emitted that deposited an energy below this threshold would not be detected.

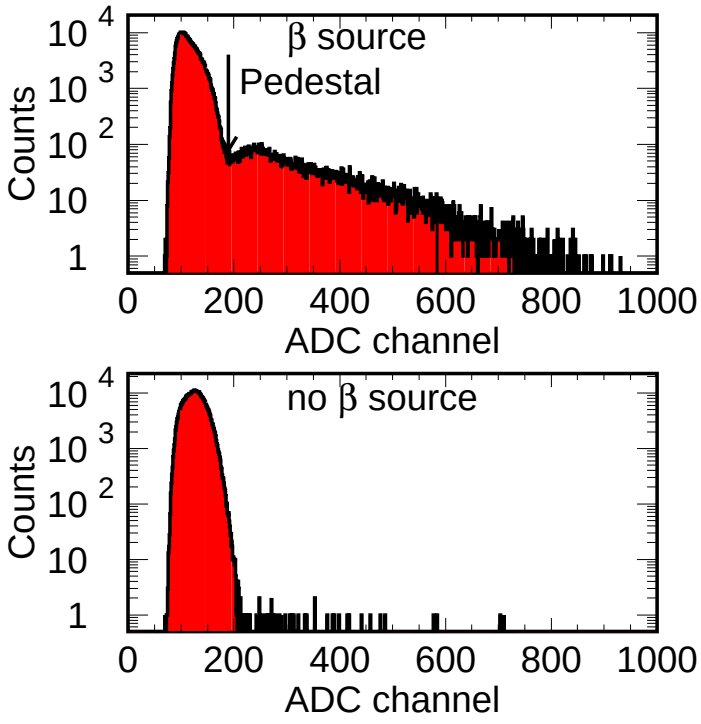

Figure 4.4: Energy spectrum corresponding to one strip of Si3. The figure in the upper part corresponds to the energy spectrum obtained using a ^{90}Sr β source. The figure at the bottom shows the energy spectrum obtained when there was no radioactive source near the detectors.

Table 4.2: *Energy thresholds of the DSSD. The energy threshold corresponding to the Si1 Y(3) is not included since this strip was not working properly during the experiment*

Si1 X	E_{th} (keV)	Si1 Y	E_{th} (keV)	Si2 X	E_{th} (keV)	Si2 Y	E_{th} (keV)
1	286.8	1	396.8	1	323.0	1	425.9
2	310.8	2	446.4	2	357.8	2	434.2
3	300.6	3	—	3	320.0	3	420.2
4	323.8	4	464.3	4	326.8	4	410.5
5	314.7	5	593.6	5	400.0	5	490.0
6	138.8	6	469.3	6	327.3	6	416.9
7	310.4	7	508.9	7	360.1	7	51.2
8	275.9	8	486.6	8	394.4	8	482.2
9	296.6			9	519.7		
10	237.4			10	278.4		
11	345.6			11	130.1		
12	331.4			12	265.4		
13	360.0			13	375.7		
14	324.6			14	271.5		
15	323.5			15	262.5		
16	320.2			16	316.1		
Si3 X	E_{th} (keV)	Si3 Y	E_{th} (keV)	Si4 X	E_{th} (keV)	Si4 Y	E_{th} (keV)
1	282.8	1	536.5	1	378.8	1	400.8
2	341.6	2	522.2	2	417.5	2	365.3
3	378.5	3	477.5	3	351.1	3	407.3
4	328.0	4	595.8	4	367.3	4	438.4
5	400.4	5	582.8	5	347.9	5	421.6
6	308.0	6	705.9	6	384.2	6	395.5
7	342.6	7	730.1	7	357.3	7	404.7
8	423.1	8	508.6	8	382.5	8	407.8
9	346.2			9	384.2		
10	412.0			10	443.3		
11	365.4			11	339.2		
12	379.2			12	398.5		
13	501.1			13	421.1		
14	324.9			14	387.5		
15	362.2			15	412.4		
16	344.1			16	384.4		

4.3 Scintillator detectors: veto of the implantation

A couple of plastic scintillator detectors were placed both in front of and behind the active stopper (SC5 and SC6 in figure 4.1). The scintillator SC5 provides information on the position of the penetrating fragments, and SC6 acts as a veto detector, allowing the offline suppression of those fragments which were not stopped in the catcher. The sensitive area of the scintillators is 200 mm x 80 mm.

For the scintillator SC5 we recorded the time difference of the signals arriving at the two photo-multipliers, mounted at the left- and right-hand side, and the horizontal position at the scintillator was determined as explained in chapter 2. We also registered the energy-loss signals at the left- and right-hand of each scintillator. These energy signals will allow us to define the veto condition and to determine the thickness of the aluminium degrader needed to implant the selected fragments in the active stopper. The energy threshold of the plastic scintillator was determined by the energy spectra obtained using the β trigger (see figure 4.5).

4.4 Implantation technique

In order to perform fragment-β time correlations, it is necessary to slow-down the nuclei to be able to implant them into the active stopper. The width of the resulting range (σ_R) of ions stopped in matter is determined by the incident momentum distribution σ_p of the projectiles, the location straggling, that is the momentum width of fragments produced along the target thickness due to the different specific energy losses of projectile and fragment, the reaction straggling related to the Fermi momentum of the abraded nucleons and the energy-loss straggling due to fluctuation of the energy loss due to the individual ion-electron collisions. However, this latter contribution is quite small.

To obtain a narrow range distribution in the active stopper, a significant reduction in momentum spread is necessary. A monoenergetic degrader [140] at the dispersive focal plane has been used to reduce the momentum spread effectively. This will increase the efficiency of capture by the active stopper.

As described in chapter 2, when using the monoenergetic FRS degrader, the fragments have an extended horizontal image. As a consequence, using this degrader is quite a convenient way for illuminating as many pixels as

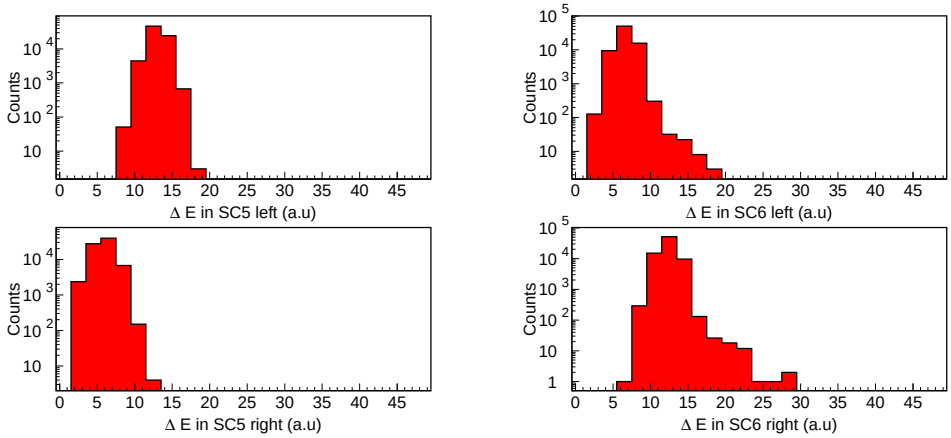

Figure 4.5: *Pedestals of energy spectra of the scintillators SC5 and SC6 as detected by the left-hand photomultiplier (top) and the the right-hand one (bottom) respectively, when using the β-trigger.*

possible in the active stopper in order to avoid multiple implantation in the same pixel.

Let us consider a fragment (A, Z) with momentum p and range R, and another ion $(A+\Delta A, Z+\Delta Z)$ and momentum $p+\Delta p$. The range difference, following the discussion presented in chapter 2, will be given by

$$\frac{\Delta R}{R} \approx \lambda \frac{\Delta p}{p} + \frac{\Delta A}{A} - 2\frac{\Delta Z}{Z} \tag{4.2}$$

Two fragments that follow the same trajectory have the same $B\rho$, so that

$$\frac{\Delta B\rho}{B\rho} = 0 = \frac{\Delta p}{p} + \frac{\Delta A}{A} - \frac{\Delta Z}{Z} \tag{4.3}$$

and therefore

$$\frac{\Delta R}{R} \approx (\lambda - 2)\frac{\Delta Z}{Z} - (\lambda - 1)\frac{\Delta A}{A} \tag{4.4}$$

The different nuclei transmitted at the final focal plane have slightly different energies and ranges, thus the isotopic selection was accomplished by using this range difference and varying the thickness of the homogeneous aluminium degrader at F4.

In order to implant a given nuclide in the middle of the active stopper, we calibrated first the thickness of the degrader by using the primary beam, ^{208}Pb. In Figure 4.6 we show the energy loss of the beam in the scintillators in front (SC5) of and behind (SC6) the active stopper for different degrader thicknesses. In cases 'A' and 'B' the energy loss in the scintillator in front of the active stopper is proportional to the energy loss in the scintillator behind it. This corresponds to degrader thicknesses thin enough to allow the beam to cross both scintillators. As we progressively increase the degrader thickness, the scintillator behind the active stopper, SC6, starts to prevent the beam from passing through. The energy loss in that scintillator starts to decrease, since the fragment deposits less energy due to the decreasing range in the scintillator. This effect can be seen in regions C, D, E, and F in the figure 4.6. Region G corresponds to a degrader thickness for which half of the beam distribution reaches the scintillator SC6. If we add to this degrader, the aluminium-equivalent thickness of the air that separates the scintillator SC6 and the active stopper (35 cm), the thickness of the titanium window of the vacuum chamber (50 μm), and half of the thickness of the DSSD (0.5 mm), we would then implant the beam just in the middle of the active stopper. We used this degrader thickness to calibrate the implantation of different species, so that

$$T(X) = R(X) - R(^{208}Pb) + T(^{208}Pb)\ mg/cm^2 \tag{4.5}$$

where T(X) is the required degrader thickness to implant a given nuclide which has a range R(X) at F4, in the middle of the active stopper.

In the experiment we selected five different implantation settings. The corresponding degrader thicknesses used during the experiment are summarised in table 4.3. Table 4.4 summarises the energy and implantation range of fragments in the active stopper for the different settings calculated using LIESCHEN [118] and AMADEUS [113].

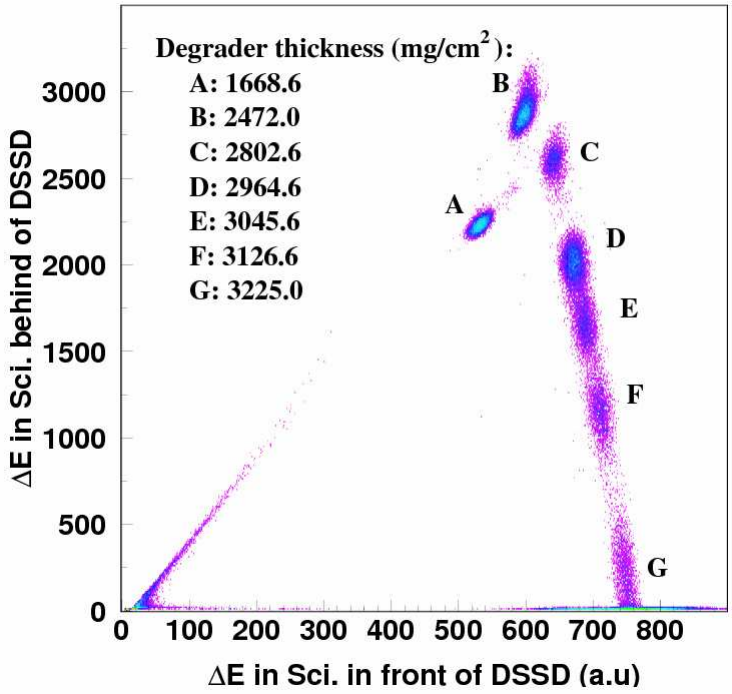

Figure 4.6: Calibration of the thickness of the aluminium degrader used during the experiment. The energy loss of the ^{208}Pb beam at the scintillator detectors placed both in front of and behind the catcher is represented. The different letters indicate the beam distribution at the different degrader thicknesses.

Table 4.3: *Thickness of the homogeneous degrader placed at the final focal plane needed to implant different species in the middle of the active stopper. The target and degrader thickness used for the production and separation of the nuclei are also included. All thicknesses are given in* (mg/cm^2)

Setting	Target	Degrader at F2	Degrader at F4
^{186}Lu	2526	5186	3752
^{190}W	1023	5962	3818
^{194}W	2526	5186	3253
^{198}Ir	1023	5041	4259
^{202}Ir	2526	4320	3664

Table 4.4: *Range of different fragments in the 980 μm thick silicon detector. Ranges (R) are given in μm and energies at F4 in MeV*

Z	A	E_{min}	R_{min}	E_{av}	R_{av}	E_{max}	R_{max}
75	197	514.2	—	514.8	—	515.4	—
75	196	520.1	93.3	520.6	127.9	521.2	162.9
75	195	525.9	336.3	526.9	397.9	527.9	462.1
75	194	531.6	577.1	532.3	614.6	532.9	652.5
75	193	537.4	815.4	538.1	854.6	538.7	894.2
74	194	521.2	533.3	521.9	576.3	522.6	618.8
74	193	527.0	775.4	527.7	821.3	528.5	866.7
74	192	532.7	—	533.5	—	534.2	—
74	191	538.4	—	539.2	—	540.0	—
75	193	559.8	—	560.5	—	561.2	16.7
75	192	566.3	204.2	567.0	249.2	567.7	292.5
74	192	555.2	164.6	555.9	209.2	556.6	253.3
74	191	561.7	446.7	562.4	490.8	563.0	528.8
74	190	568.2	725.4	568.9	769.6	569.5	807.5
74	189	574.7	—	575.3	—	575.9	—
73	189	564.9	—	564.3	—	570.6	—
72	187	542.3	294.2	543.5	371.7	544.7	449.2
72	186	548.0	530.8	549.3	614.6	550.5	692.1
71	188	526.4	59.2	527.8	151.7	529.2	244.6
71	187	532.0	299.6	533.5	398.8	534.9	491.3
71	186	537.7	544.6	539.2	643.3	540.6	643.3
79	204	568.6	—	569.8	25.4	571.0	96.7
78	204	560.2	47.1	561.7	137.9	563.2	270.4
78	203	564.8	207.9	566.3	298.3	567.8	389.2
78	202	569.5	372.9	571.0	462.9	572.4	547.5
78	201	574.1	529.6	575.6	619.6	577.0	703.8
77	203	556.5	312.5	558.3	423.6	560.1	534.6
77	202	561.1	476.7	562.9	587.5	564.7	698.3
77	201	565.7	638.8	567.5	749.6	569.3	860.0
77	200	570.3	799.2	572.1	909.2	573.9	—
77	199	575.0	963.3	576.8	—	578.5	—
76	201	555.4	629.6	558.5	824.2	561.6	—
76	200	562.0	920.8	564.1	—	566.2	—

4.5 Position correlation

Fragment implantation events were established by software, first requiring a signal above the threshold in the scintillator SC5 in front of the active stopper, no signal in the veto detector SC6, and a high-energy signal in a given pixel (x, y), where x is a horizontal strip and y a vertical strip of the DSSD. The high-energy implantation events were recorded as overflow events. Moreover, the large implantation signal for a given strip induced signals in neighbouring strips, resulting in an average implantation multiplicity of three in the x-strips (see figure 4.7). The data was affected by a high cross-talk on the y signal that inhibited pixel analysis, therefore only the analysis of the correlated fragment-β-decay events occurring in the same x-strip will be considered. Figure 4.8 shows the position correlation between the SC5 signals and the x-strip for the fragments implantations.

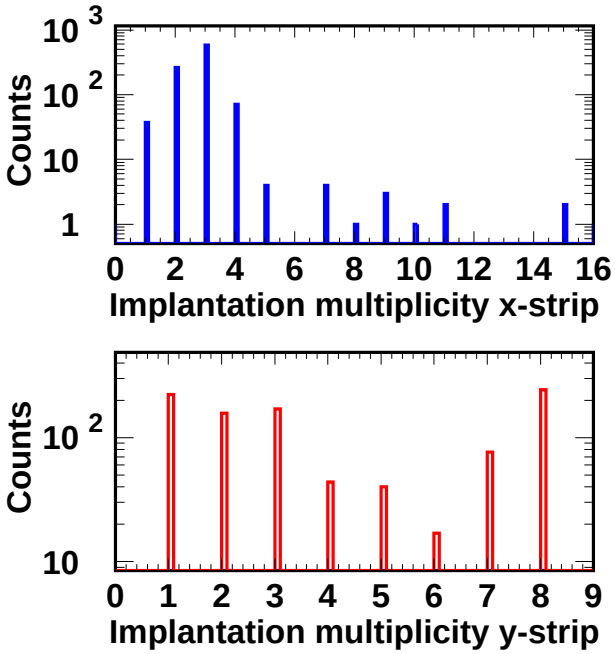

Figure 4.7: Implantation multiplicity of the DSSD for one setting of the FRS optimised to transmit ^{194}W. The multiplicity refers to the number of strips that were triggered for a given implantation event.

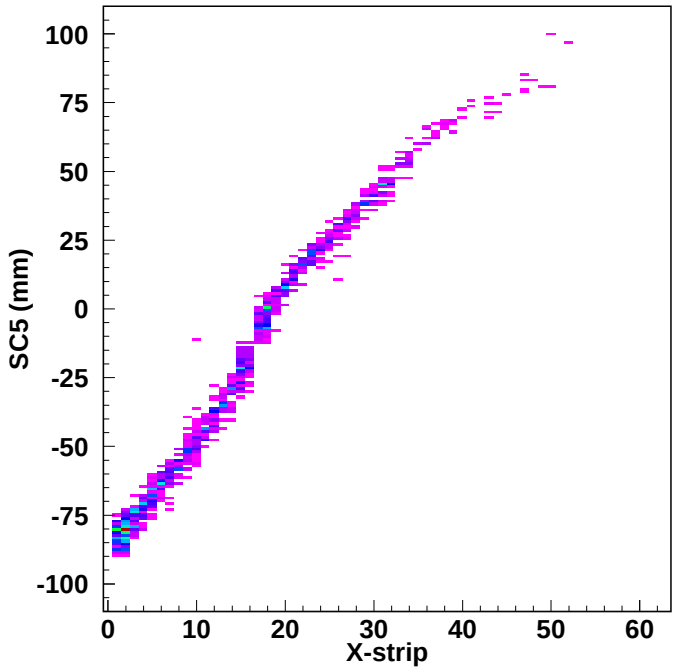

Figure 4.8: Position correlation between the horizontal position in the SC5 scintillator in front of the active stopper and the x-strip hit by the implanted fragments for one setting of the FRS optimised to transmit ^{194}W.

4.6 Implantation results

Between 6 to 9 different nuclides transmitted to the final focal plane are implanted into the active stopper, which allows us to measure the half-life of several species at the same time. Fragments with shorter ranges are stopped either in the degrader or in the layers of matter before the active stopper. The veto rejects more penetrating or secondary fragments produced in any of the layers of matter.

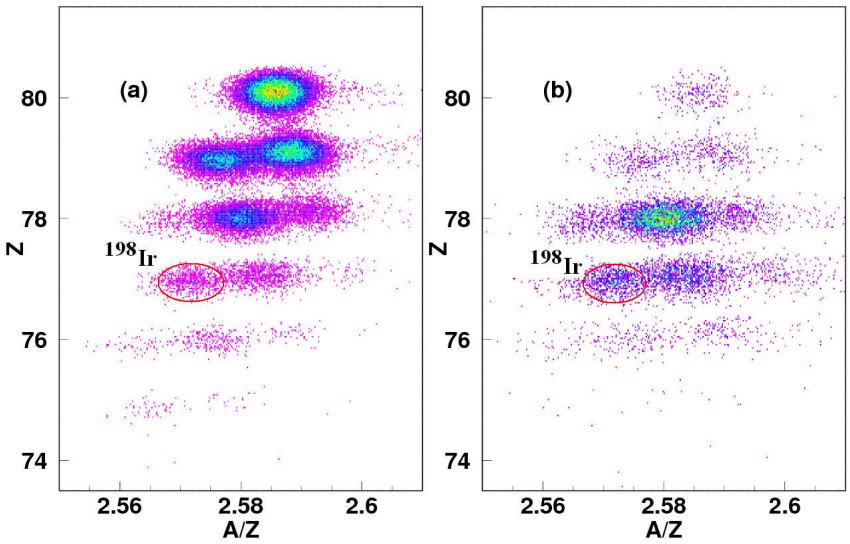

Figure 4.9: Particle identification plots corresponding to a FRS setting optimised to transmit ^{198}Ir with a monoenergetic degrader. The figure shows the total production yield at the end of the FRS (a) and the ions which were selected for implantation in the 1mm-thick DSSD.

Table 4.5 summarises all the fragments implanted during the experiment. The production rate at the final focal plane and corresponding number of implantations are included.

Figure 4.9 shows an example of an identification matrix corresponding to one setting of the FRS, optimised to transmit ^{198}Ir using the monoenergetic degrader of the FRS. The left panel shows the nuclei identified at the final focal plane and the right panel shows the corresponding nuclei implanted into the active stopper. The implantation probability is never higher than 50 %. This is explained by secondary

reactions in the layers behind the FRS and the finite detection efficiency. Figure 4.10 shows the implantation depths of the different nuclei, for the same setting as calculated using LIESCHEN and AMADEUS. Not only fully-stripped ions but also some ions with H-like charge states fall into the range window of the active stopper. Charge states of a given selected fragment are not implanted into the DSSD as they have longer ranges.

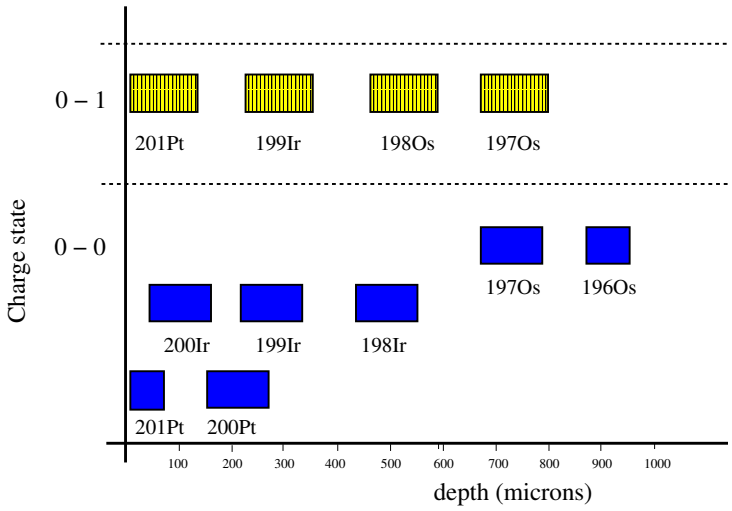

Figure 4.10: Implantation depth in 980 μm of Si as calculated using LIESCHEN/AMADEUS for a FRS setting optimised to transmit ^{198}Ir with a monoenergetic degrader. Fully-stripped and He-like charge states are included

4.6.1 Contaminants in the active stopper

We have to consider the possibility that the nuclide identified in the FRS undergoes a nuclear reaction in the degrader, in one of the detectors or in another layer of matter behind the fragment separator, before it is stopped. When such a secondary product is implanted in the active stopper, its β-decay is erroneously attributed to the identified nuclide and falsifies the β half-life measurement. In the present section we investigate the importance of this problem.

We calculated the energy and range distributions of all primary fragments transmitted to the final focal plane with the LIESCHEN code.

As an example, the calculations made for ^{195}Re are presented. ^{195}Re fragments leave the fragment separator with an average energy of 402 A MeV. When these fragments pass through an aluminium layer of 3293 mg/cm^2, corresponding to the degrader thickness used in the experiment, they undergo a nuclear reaction with a probability of 25.5%. This corresponds to the total reaction cross section of 4.18b as calculated with the Glauber-type KAROL code [128]. Since the other layers of matter are much thinner, they are not considered here. Fortunately, most of the secondary fragments have different ranges predominantly smaller ranges than the primary fragment, and thus they are not implanted in the stopper. In order to calculate the formation cross sections of all secondary fragmentation residues, we used the ABRABLA code [48]. From this calculation we estimate that the total amount of secondary fragments falling into the range window of the active stopper amounts to 3.9% of the number of primary fragments. They are dominated by the neutron-removal channels.

Figure 4.11 shows the calculated range distributions using LISE++ [141] with the ABRABLA cross sections for the ^{195}Re case. Table 4.6 summarises the contaminants implanted into the active stopper. Only neutron-removal channels are presented, since they are the ones which contribute most to the contamination, as can be seen in figure 4.11.

If the nuclide of interest is well implanted into the DSSD, as is the case in the example presented above, this unavoidable contribution represents only a small fraction of the deposited nuclei, and the beta half-life measurement is not noticeably disturbed. The problem becomes more severe, if the range distribution of the nuclide of interest does not peak inside the DSSD detector and consequently this nuclide is implanted with lower probability. The most severe problem arises, if the range distribution of the nuclide of interest peaks behind the active stopper. Since the strong neutron-removal contaminants have shorter ranges, they will be implanted with high probability and represent a large fraction of the observed betas. But also the relative contribution of contaminants with larger ranges can become high when most of the nuclides of interest are stopped in front of the active stopper.

As a consequence of these considerations, the analysis has been restricted to those species, which are implanted with high probability.

Table 4.5: *Total number of fragments detected at F4 and implanted into the active stopper during the experiment*

Nuclide	N. of fragments at F4	N. of implanted fragments
^{204}Pt	1925	32
^{203}Pt	8445	200
^{202}Pt	36748	6001
^{201}Pt	2810	634
^{203}Ir	188	21
^{202}Ir	3137	1090
^{201}Ir	13110	4820
^{200}Ir	14387	3387
^{199}Ir	2143	1056
^{198}Ir	2326	1271
^{200}Os	547	331
^{199}Os	3013	1303
^{196}Re	1058	454
^{195}Re	1527	625
^{194}Re	1148	314
^{193}Re	1322	236
^{192}Re	722	298
^{194}W	212	100
^{193}W	473	208
^{192}W	73	19
^{191}W	551	255
^{190}W	641	420
^{190}Ta	304	89
^{189}Ta	175	60
^{187}Hf	89	43
^{186}Hf	85	28
^{188}Lu	47	3
^{187}Lu	89	6
^{186}Lu	85	6

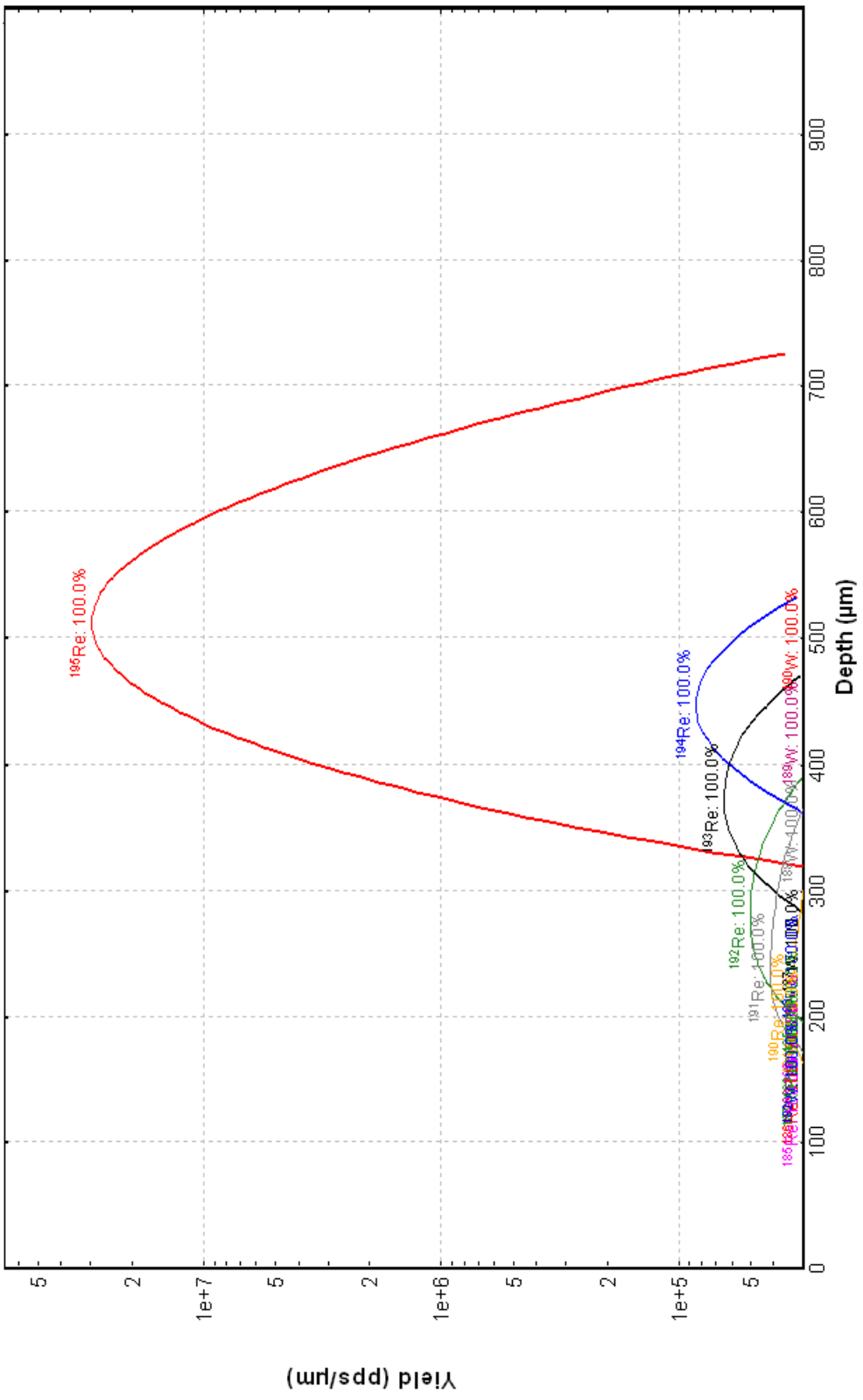

Figure 4.11: Yields and implantation depth of secondary reaction fragments produced in the homogeneous degrader for ^{195}Re

Table 4.6: *Contaminants of the* ^{195}Re implanted into 1 mm of Si, calculated using ABRABLA and LISE++. Only n-removal channels are indicated. The total number of simulated ^{195}Re is 5.45E8 nuclei.

Nuclide	N. of implanted nucleus	(%) stopped in detector
^{195}Re	5.24E8	96.1
^{194}Re	1.44E6	0.26
^{193}Re	1.26E6	0.23
^{192}Re	1.06E6	0.19
^{191}Re	9.63E5	0.18
^{190}Re	9.13E5	0.17
^{189}Re	8.27E5	0.15
^{188}Re	7.21E5	0.13
^{187}Re	6.26E5	0.12
^{186}Re	5.41E5	0.10

Chapter 5

β half-life measurements

In order to measure the half-lives, the nuclei of interest were implanted into an active stopper. Half-lives were deduced from position-time correlations between the implanted fragments and the subsequent β-decays. The lifetimes were extracted from the measured and simulated ratio of the spectra of time correlations in forward and backward directions by applying the least-squares method. In this chapter the aforementioned procedure will be described in detail.

5.1 β-fragment position correlations

As discussed in chapter 4, implantation events were identified in software in an event-by-event basis, by first requiring a signal above the threshold in the scintillator SC5 in front of the active stopper, no signal in the veto detector SC6, and an overflow in a strip detector. The particle identification data (Z,A) as well as the implantation time, were stored for each implantation event.

A subsequent β-decay in the same strip was that which produced a low-energy signal above threshold in a single strip. Unlike implantation events, β events could be isolated to a given pixel. This was due to the fact that the emitted β particles were far less energetic than the implanted ions. In addition, rather than depositing their full energy within the DSSD, the β particles were depositing just a fraction of their total energy, as they were emitted from a given pixel in the DSSD. These β decays were then correlated with previously identified implanted nuclei within a given strip.

5.2 β-fragment time correlations

5.2.1 Correlations with complex background

A fragment-β-correlated time spectrum was generated by histogramming the differences between the time of the β-events and the correlated implantation events to generate a decay curve (see figure 5.1). This time distribution was obtained from the time intervals between an implantation and the first β-particle detected after implantation.

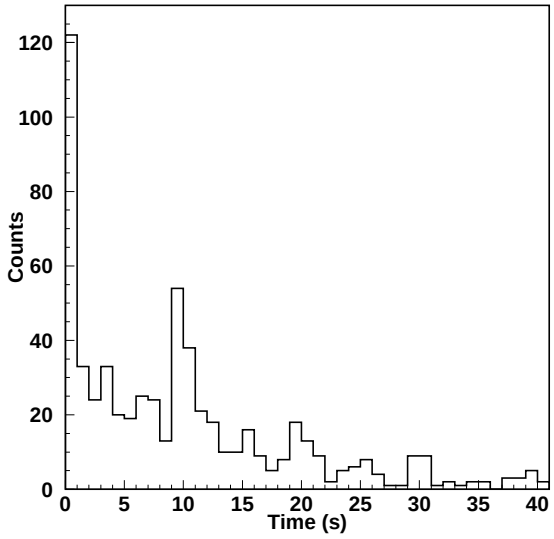

Figure 5.1: Example of a time correlation spectrum obtained during the experiment.

The beam extracted from SIS has a spill structure (See figure 5.2), with a typical spill length of 2 s and a repetition cycle of 10 s. Due to the pulsed structure of the beam, the rates of implantation events and β-decay were modulated with a periodic time structure, which is clearly visible in figure 5.1. This pulsed structure makes the analysis of the time-correlation distributions more delicate, as the background determination is the key to the time-correlation analysis.

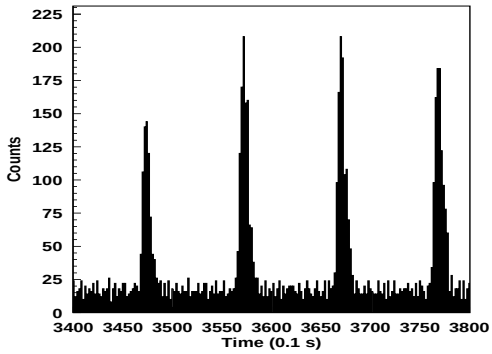

Figure 5.2: Spill structure of the beam as seen by the SEETRAM monitor.

5.2.2 Background evaluation

The β background is an essential parameter for the analysis of the time interval sequences between implantations and β-decays. If the β-background is too high, the determination of the β-decay half-lives becomes a more delicate matter.

In the experiment we observe a beam-induced background contamination in the recorded time-correlation spectra. This background originates from the time structure of the previously implanted nuclei and the presence of δ or atomic electrons generated during the beam pulse.

In order to be able to disentangle the background from the real events, it is necessary to establish the shape of the uncorrelated events. It is evaluated by histogramming the time difference between a given implantation to a previous β, that is, making the fragment-β correlations in a time reversed sequence.

When comparing the forward- and backward-time spectra we found a signature in the forward-time correlations that is not present in the backward-time correlations(See figure 5.3). The ratio between the forward- and backward-time correlations contains the information on the 'true' fragment-β correlations.

For certain measurements where the percentage of implanted ions and the frequency of β background are elevated, the pulsed component described above acquires a huge importance and disturbs the measurements of the half-lives, and as a consequence has to be taken carefully into account when it comes to determining the half-lives.

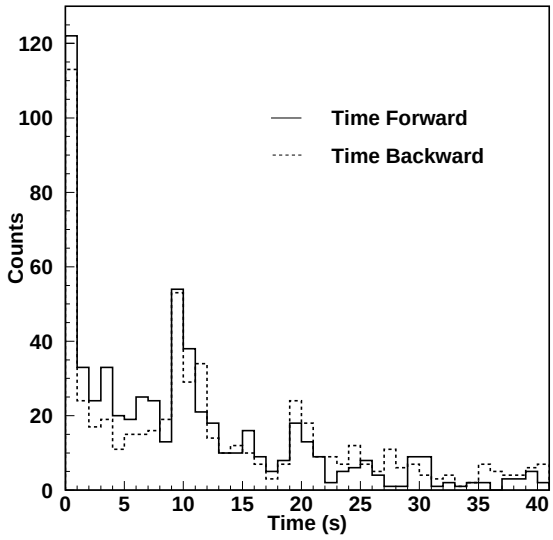

Figure 5.3: Measured implantation-β forward and backward time distributions

5.3 Procedure for determining β half-lives

5.3.1 First principles of the method

The half-lives of the nuclei were deduced from time-position correlations between the implanted fragments in the active stopper and the subsequent β-decays. As described above, due to the pulsed structure of the beam, the event rates of implantation and decay were modulated with a periodic time structure. In addition, we were faced with a beam-induced background contamination in the recorded time-correlation spectra.

The very complex background conditions found in the present data cannot be easily modelled theoretically. We propose a new method to determine the β-decay half-lives by fitting the experimental data to a numerical function (rather than an analytical function), obtained from Monte-Carlo simulations of time correlations between implantations and β-decay events, which allow us to evaluate and disentangle the background from the real decays.

5.3.2 Monte Carlo simulation

A Monte-Carlo code has been developed to simulate the time sequences in an experiment with implantations of β-radioactive ions. In this code the time sequence of fragment implantation and β detection are simulated according to the experimental conditions (spill sequence, fragment implantation rate during the spill and background rate during spill and pause), leaving two free parameters: the β lifetime τ, and the efficiency ϵ for the detection of the β decays of the nuclide of interest. The code produces time-correlation spectra in forward- and backward-time direction.

For simplicity, only one "cell" is considered. This cell corresponds to the strip or pixel which was triggered by one implantation and by one β-like event. All frequencies given as input parameters refer to this cell. A realistic simulation of the experimental conditions with different counting rates in the different cells can be performed by an accumulation of a series of calculations in which the appropriate parameters for each cell are specified.

When N_F nuclides are implanted, the expected number of β-like events in the time-correlation spectrum, recorded in a time interval $[t, t + \Delta t]$ is

$$\Delta N(t) = N_F \rho(\tau, \epsilon, t) \Delta t \tag{5.1}$$

where $\rho(\tau, \epsilon, t)$ is the probability density for detecting a β-like event in a time t after the implantation of the considered nuclide. This β-like event can be a 'true' β coming from the decay of the nuclide under study or a background event. The analysis can be performed on all consecutive β-like events detected in a given time interval or on the first β-like event detected following the implantation.

We developed two versions of the code: one which accumulates all β-like events observed after implantation up to a given maximum time T_{max}, and a second version which accumulates only the first β-like event observed after implantation. The corresponding source codes can be found in GSI-CHARMS web-page [142].

In figure 5.4 the results using both methods are shown. The parameters used in the simulations are: 2 s spill length, 10 s cycle, an implantation rate of 0.003 s^{-1}, a frequency of β-like events during spill of 0.1 s^{-1}, a frequency of β-like events during pause between spills of 0.0375 s^{-1}, a lifetime of 9 s, an efficiency of 30 % and a maximum correlation time of 30 s, which are typical values of the parameters we found in the data analysis.

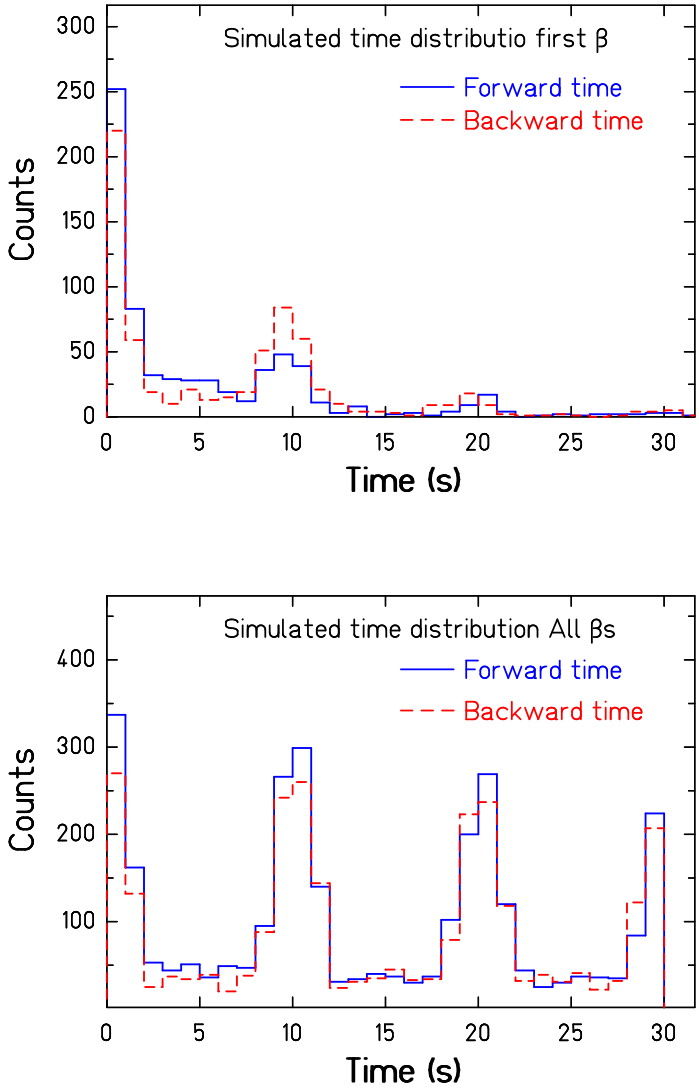

Figure 5.4: Monte-Carlo simulated time distributions considering only the first β-like event observed after implantation of a given nuclide (top), and the corresponding one (bottom) when considering all β-like events observed after implantation up to a given maximum time of 30 s.

The first histogram shows the time-correlation distributions, forward and backward in time when using the code version which accumulates only the first β-like event observed after implantation. The second histogram shows the time-correlation distributions using the same experimental conditions, but the code version which accumulates all β-like events observed after implantation up to a given maximum time T_{max}.

From this study it can be observed that finding the first β-like event after fragment implantation gives a clearer sign of the β-decay and reduces the influence of the β-background. The benefit of recording only the first β-like event is twofold: Firstly, in the time interval corresponding to the lifetime of the nucleus, the contribution of the background events is considerably reduced, and the excess of counts due to the true βs is much clearer. Secondly, the height of the spectrum at larger times is reduced due to the 'shielding' of the background by the preceding true decay events. Thus, the experimental signature in the time-correlation spectra even extends beyond the time range strongly populated by the true decays. Therefore, for treating the analysis of the data we will consider only the first β-like event observed after implantation.

5.3.3 The χ^2 fit procedure

Since the experimental time-correlation spectra correspond to a limited number of events, the number of counts in the different time bins is subject to statistical fluctuations according to the Poisson statistics. Therefore, the measured time-correlation spectrum will deviate from the simulated one, even if the parameters of the simulation were 'correct'. For extracting the parameters of interest, e.g. the half-life of the nuclide considered, we apply the chi-squared (χ^2) method by determining the parameters of the simulation, which are most compatible with the measured spectra.

The chi-squared (χ^2) statistic characterises the dispersion of the observed frequencies from the expected frequencies. The χ^2 test can be applied when comparing two sets of data in an attempt to decide whether or not they were drawn from the same parent population.

If we have two distributions, $g(x_j)$ and $h(x_j)$, the χ^2 is given by

$$\chi^2 = \sum_{j=1}^{n} \frac{[g(x_j) - h(x_j)]^2}{\sigma^2(g) + \sigma^2(h)} \tag{5.2}$$

The denominator $\sigma^2(g) + \sigma^2(h)$ is simply the variance of the difference $g(x_j) - h(x_j)$. The expectation value for χ^2 is $< \chi^2 >= \nu$, where ν is the number of the degrees of freedom and is equal to the number n of sample

frequencies minus the number of constraints or parameters that have been calculated from the data.

The reduced chi-squared χ^2_ν is defined as $\chi^2_\nu \equiv \chi^2/\nu$, with the expectation value $< \chi^2_\nu > = 1$. Values of χ^2_ν much larger than 1 result from large deviations from the assumed distribution and may indicate poor measurements, or an incorrect choice of the probability function. Very small values of χ^2_ν are equally unacceptable and may imply some misinterpretation of the experiment [105].

In the χ^2 test we assume Gaussian statistics and quote the standard deviation σ in a result from the Gaussian probability density function, in which approximately 68.3 % of the events of the Gaussian distribution fall within $\pm\sigma$ of the mean and approximately 95.4 % fall within $\pm 2\sigma$.

According to the least-squares method, the optimum values of the parameters a_j of the fitting functions are obtained by minimising χ^2 simultaneously with respect to each parameter. As the condition for minimising χ^2 is that the first partial derivative with respect to each parameter cancels out (i.e., $\partial\chi^2/\partial a_j = 0$)), we can expect that near a local minimum with respect to any parameter a_j, χ^2 will be a quadratic function of that parameter.

In addition, we can estimate the errors in the fitting parameter a_j by varying each parameter around the minimum to increase χ^2 by 1 unit from the minimum value.

The definition of the confidence level in a one-parameter experiment is generally straightforward. We can plot the data and observe whether the distribution is Gaussian and estimate directly from the distribution of the probability that the result lies between two specified values. When two or more variables have been determined and those variables exhibit some correlation, the definition of the confidence level becomes a little more difficult.

The contour plot of χ^2 as a function of two parameters a_1 and a_2 is generally approximately elliptical near the minimum. The degree of correlation between the parameters is indicated by the tilt of the ellipse.

In order to determine a confidence interval, that is, a region of the $a_1 - a_2$ space in which we estimate there is for example, a $\approx 68\%$ probability of finding the true values of the two parameters we should consider the full range of the $\Delta\chi^2 = 1$ contour. This is equivalent to allowing a_2 to assume its best values for each chosen value of a_1. Similarly, if we wish to find the limits of 2 standard deviations, we should find the limits on the $\Delta\chi^2 = 4$ contour.

In the present work, the half-lives of the different nuclides under study were obtained from two-dimensional fits of the measured and simulated

ratios of time correlations in forward- and backward-time direction. This was achieved by applying the least-squares method in which the lifetime τ and the β-detection efficiency ϵ are the two-fitting parameters.

5.3.4 Limits of the method

As described in previous sections, we determine the half-life of a given nuclide using the statistical analysis of the distributions of time intervals between the implantation of the selected fragment and the subsequent β-like event in the same strip detector. Because we assume Gaussian statistics in the χ^2 calculation, the number of counts in the histogram bins has to be approximately > 10 [105]. In this case, the Poisson distribution can be well approximated by a Gaussian function. However, if we are concerned with statistical accuracy, we can merge the low-counting bins to satisfy the Gaussian statistic requirements.

With regard to the present data, the analysis of the time-correlation distributions is quite a delicate matter, in that we are limited by the β-detection efficiency and by the presence of a considerable and complex β-background.

In order to be able to produce a significant result from such an analysis, it is essential that the number of β-correlations corresponding to the decay of the nuclide under study is greater than the number of fluctuations from the β-like background (at least in the region of the time distribution, where most of the β-decays are concentrated, that is, $t \leq T_{1/2}$).

Following the discussion on the statistical analysis presented in Ref. [119] and Ref. [81], let N_F be the total number of implanted fragments from which we can measure the half-life $T_{1/2} = ln2\tau$, ν_β the background rate of β-like signals measured per detector, and ϵ the β detection efficiency. The number of 'true' β-decays detected during a time equal to $T_{1/2}$ after the implantation of the fragment, is then $N_F\epsilon/2$, and the β-like background detected in the same time $N_F\nu_\beta T_{1/2}$. The fluctuation of the random events at same time is the square root of the last formula.

If we impose as a condition that the number of true correlations has to be at least three times the number of random correlations

$$N_F\epsilon/2 > 3\sqrt{N_F\nu_\beta T_{1/2}} \tag{5.3}$$

we obtain an upper limit of the value of the half-life that we can measure

$$T_{1/2} < \frac{N_F\epsilon^2}{36\ \nu_\beta}. \tag{5.4}$$

If we decrease the ν_β by increasing the thresholds over the ΔE_β in the analysis, in order to reduce the noise, we also decrease ϵ, which itself intervenes in that which has been discussed above, so this reduction has to be made carefully.

From the experience gained during the analysis we found that we can expect to obtain reliable results with our analysis method, if the number of true correlations is at least four times higher than the fluctuations of the random correlations, leading to the condition

$$N_F\epsilon/2 > 4\sqrt{N_F\nu_\beta T_{1/2}} \tag{5.5}$$

being the upper limit of the value of the half-life that we can measure

$$T_{1/2} < \frac{N_F\epsilon^2}{64\ \nu_\beta}. \tag{5.6}$$

Correlating the position of the implanted ion with the position of the subsequent β-like event detected leads to a reduction of the random events, but as it was described in chapter 4, the high noise y signals from the DSSD stack inhibited pixel analysis, therefore only the analysis of fragment-β correlations occurring in the same strip will be considered. This effect will increase the β-background counting rate, and will impose restrictions on the analysis of the time correlations.

As it was described in section 5.2.2, the background signals may come from the β-decays of the previously implanted fragments in the same strip, or from δ electrons produced by the fast highly-charged ions. Due to the spill structure of the beam, we are faced with not only a periodic time structure which modulates the event rates of implantation and decay, but in addition, a beam-induced background contamination in the recorded time spectra. For the ^{202}Ir and ^{198}Ir implantation settings this beam prompt background dominates and does not allow us to perform the time correlation distributions with the full time structure, but only in the pause between spills. As it will be shown in the next section, the results obtained using the full time distribution, or the time correlations only during the pause between spills, give consistent results, but the latter gives the cleaner conditions, and the error bars in the final half-life are smaller, so in general the analysis for all nuclides will be performed only during the pause between beam pulses.

In table 5.1 we summarise the parameters associated with each measurement: number of fragments N_F, average background rate ν_β per strip, and the corresponding upper limits of the half-lives for each nuclide under study, assuming an average ϵ equal to 30%. One should consider

that the value of ν_β used in eq. 5.6 to calculate the $T_{1/2}$ upper limit is appropriately chosen: For half-lives shorter than the spill length, the value during the spill should be taken. For longer half-lives, the analysis not including the spills gives smaller statistical uncertainties, and thus the value of ν_β during pauses gives the more realistic estimation. We also include the theoretical predictions for these nuclei according to the Gross-Theory calculations [144], the hybrid-model with Gamow-Teller decays in RPA and first-forbidden decays in the Gross-Theory [145], and the self-consistent QRPA approach [146–148].

The parameters which intervene in the analysis of the fragment-β time correlations are the lifetime τ, the background rate ν_β, the efficiency ϵ, the number of fragments N_F, and the time intervals in the histograms. We already discussed above the conditions for ν_β, ϵ and N_F. Two parameters that constrain the time intervals in the histograms are the maximum correlation time T_c and the minimum time between implanted ions.

The maximum correlation time is defined as the longest time window in which a β-decay can be correlated with an implanted ion. The time T_c needs to be long enough to encompass between 2 to 5 times the expected value for the half-life [149] of the nuclide under study in order to extract a reasonable decay curve. Longer T_c times would increase the chance of correlating the implanted ion of interest with a background event. The minimum implantation time is defined as the minimum amount of time between two successive implantation events. The time window defined by the minimum implantation time depends on the implantation probability in the same detector. The implantation probability follows a Poisson distribution and can be written as follows:

$$P(t) = \frac{(\nu \cdot t)^n}{n!} e^{-\nu \cdot t} \tag{5.7}$$

where ν is the implantation rate, t is the time window of the measurement and n is the number of nuclides implanted in the same detector. In order to calculate the probability of multiple implantation in the same detector we need to determine the implantation probability of more than 1 nuclide, that is, $P_m = 1 - P_0 - P_1$, where P_0 is the probability of implantation of no one nuclide and P_1 is the implantation probability of only one nuclide. Table 5.2 summarises the implantation probabilities for the different nuclides implanted for various time windows.

From this table we can realise how big the difference is in the time window available for the study of the different nuclides, depending on the implantation rate. As the expected half-lives fall into the region of a few seconds, the iridium and osmium isotopes will be the most difficult cases to

analyse. On the other hand, the rhenium and tantalum cases allow us the largest time windows, leading to most optimal experimental conditions.

Following the discussion presented above, the experimental conditions attained in the present experiment allow us to analyse the half-lives of 8 nuclides by applying the proposed least-squares method. They are ^{202}Ir,^{199}Ir, ^{198}Ir, ^{200}Os, ^{199}Os, ^{196}Re, ^{195}Re and ^{194}Re, all of them with unknown half-lives except the case of ^{198}Ir, which has a previously measured half-life of 8 s [150, 151].

5.3.5 Examples of the fitting procedure

As an example in figures 5.5 and 5.6 we show the corresponding time-correlation spectra in forward- and backward-time directions, making the time correlations in both spill and pause and only during the pause respectively (upper panels) and an example of the same distributions simulated with the Monte-Carlo code (bottom).

The data correspond to ^{195}Re, a heavy neutron-rich nuclide synthesised for the first time in this experiment. We select this nuclide because the experimental conditions, as discussed above, allow us to study the fragment-β time correlations in both with the full time distribution and only during the pause.

Figure 5.7 shows the measured ratios with the experimental error bars, and a comparison with three different Monte-Carlo simulated ratios, for a fixed efficiency, and different lifetimes in both, only during the beam pauses (top) and using the full time structure (spill+pause) (bottom). Note that the simulations have been performed with high statistics, imposing that the statistical uncertainties of the simulations are negligible. From these graphs we learn that it is necessary to make time correlations using several spills in order to distinguish between different lifetimes.

In order to determine the half-life of the selected nuclide, we perform sets of simulations with a given efficiency and lifetime, and we calculate the χ^2 from the measured and simulated ratio of the spectra of time correlations in forward- and backward-directions for each set of simulations. This allows us to perform 2-dimensional χ^2 contour plots like the ones shown in Figure 5.8. From these contour plots we found that there is a minimum in both parameters, efficiency and lifetime, from which we can determine the half-life of the nuclide by fitting the region around the minimum of the χ^2 distribution to a parabola.

Even though both types of analysis (full time and only pause) give consistent results within the error bars, that is, $T_{1/2} = 6^{+2}_{-2}$ s when using the full time structure, and $T_{1/2} = 6^{+1}_{-1}s$ when correlating fragment and

β-decays only between beam pulses. It is clear that the analysis only in the pause gives smaller error bars, which is consistent with the fact that by avoiding the beam pulses the time correlations are less dominated by the background.

This gives us confidence in the results of the half-lives determined in the cases when it is only possible to study the time correlation distributions in the pause between the beam pulses (due to the high β-background present during the spill).

Table 5.1: *Parameters associated to each measurement: number of fragments N_F, background rate ν_β, $T_{1/2}$ upper limit, and different theoretical predictions. The values marked with $*$ are previously measured data taken from literature [143]*

Nuclide	N_F	ν_β (s^{-1})	$T_{1/2}<$ (s)	$T^{th.}_{1/2}(s)$ Gr. Th. [144]	$T^{th.}_{1/2}(s)$ RPA [145]	$T^{th.}_{1/2}(s)$ CQRPA [148]
^{204}Pt	32	0.11	0.4	6.8	321.8	
^{203}Pt	200	0.11	2.3	41.1	564.0	12.7
^{202}Pt	6001	0.11	68.2	$1.8D6^*$	8650.5	
^{201}Pt	634	0.11	7.2	$2.5M1^*$	575.0	
^{203}Ir	21	0.11	0.2	3.1	34.9	
^{202}Ir	1090	0.11	12.4	8.5	68.4	9.8
^{201}Ir	4820	0.11	54.8	18.5	130.0	
^{200}Ir	3387	0.11	38.5	13.3	124.1	
^{199}Ir	1056	0.15	8.8	1.61m	370.6	
^{198}Ir	1271	0.15	10.6	$8s1^*$	377.1	19.1
^{200}Os	331	0.11	3.8	16.0	187.1	6.6
^{199}Os	1303	0.11	14.8	17.2	106.8	6.6
^{196}Re	454	0.08	7.1	5.1	3.6	1.9
^{195}Re	625	0.08	9.8	10.3	3.3	11.6
^{194}Re	314	0.08	4.9	16.1	70.8	2.6
^{193}Re	236	0.03	9.8	1.09m	414.7	
^{192}Re	298	0.03	12.4	$16s1^*$	54.0	
^{194}W	100	0.08	1.6	8.1	19.9	
^{193}W	208	0.08	3.3	21.0	12.8	
^{192}W	19	0.03	0.8	36.6	36.2	
^{191}W	255	0.03	10.6	1.16m	9.5	
^{190}W	420	0.03	17.5	$30.0M15^*$	1638.9	
^{190}Ta	89	0.03	3.7	8.5	1.4	1.5
^{189}Ta	60	0.03	2.5	34.7	96.8	10.0
^{187}Hf	43	0.03	1.8	11.7	47.8	
^{186}Hf	28	0.03	1.2	$2.6M12^*$	1139.6	
^{188}Lu	3	0.03	0.1	2.1	0.3	
^{187}Lu	6	0.03	0.3	5.0	1.4	
^{186}Lu	6	0.03	0.3	3.9	2.1	

Table 5.2: *Multiple implantation probability in the same strip for different time windows*

Nuclide	Implantation rate (s^{-1}) per strip	P_m(%) by time window (s)							
		1	10	20	30	40	60	80	100
^{203}Pt	0.006	0.0018	0.17	0.7	1.4	2.5	5.1	8.4	12.2
^{202}Ir	0.019	0.0178	1.59	5.6	11.2	17.7	31.6	44.9	56.6
^{201}Ir	0.146	0.968	42.9	78.9	93.3	98.0	99.8	100.0	100.0
^{200}Ir	0.175	1.36	52.2	86.4	96.7	99.3	100.0	100.0	100.0
^{199}Ir	0.046	0.1	7.8	23.5	40.1	54.9	76.2	88.2	94.4
^{198}Ir	0.032	0.05	4.2	13.5	25.0	36.6	57.2	72.5	82.9
^{200}Os	0.012	0.0071	0.7	2.5	5.1	8.4	16.3	25.0	33.7
^{199}Os	0.040	0.08	6.2	19.1	33.7	47.5	69.2	82.9	90.8
^{196}Re	0.003	0.0004	0.04	0.2	0.4	0.7	1.4	2.5	3.7
^{195}Re	0.006	0.0018	0.17	0.7	1.4	2.5	5.1	8.4	12.2
^{194}Re	0.004	0.0008	0.08	0.3	0.7	1.2	2.5	4.1	6.2
^{190}Ta	0.001	0.0	0.0	0.0	0.0	0.1	0.2	0.3	0.5
^{189}Ta	0.001	0.0	0.0	0.0	0.0	0.1	0.2	0.3	0.5

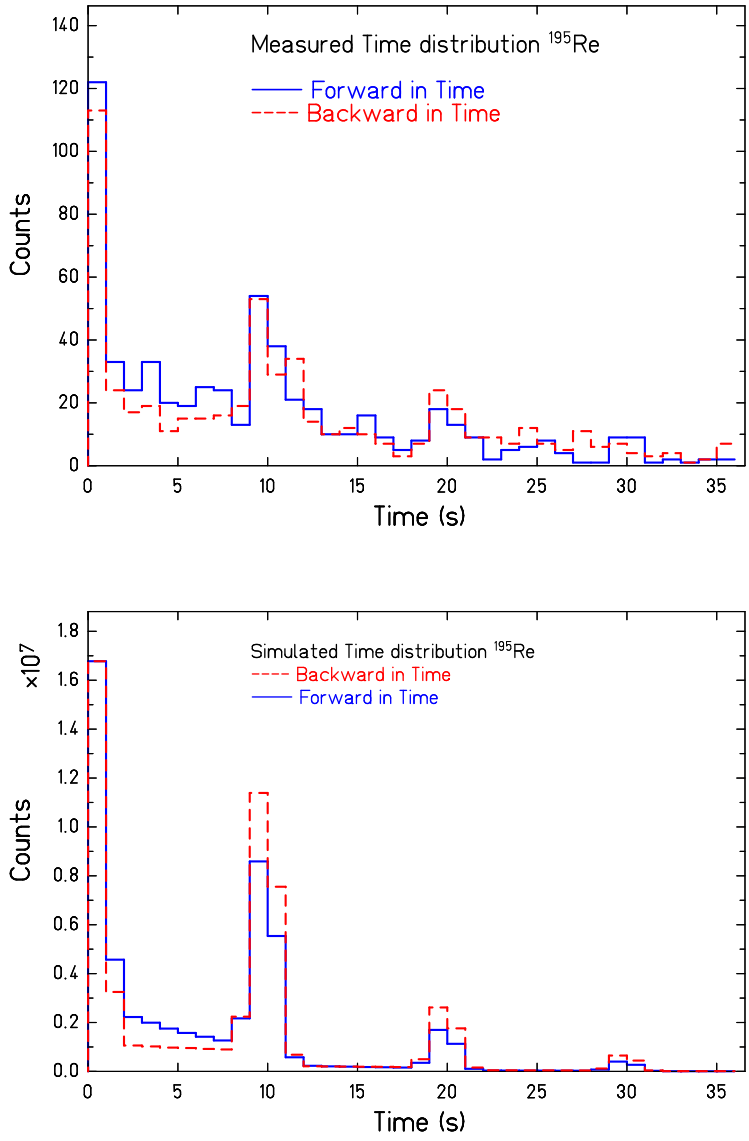

Figure 5.5: Measured implantation-β forward- and backward-time distributions for ^{195}Re for the full-time structure (spill+pause) (top) and an example of the same distributions simulated with a Monte-Carlo code assuming $\tau = 8$ s and 40 % β-detection efficiency (bottom).

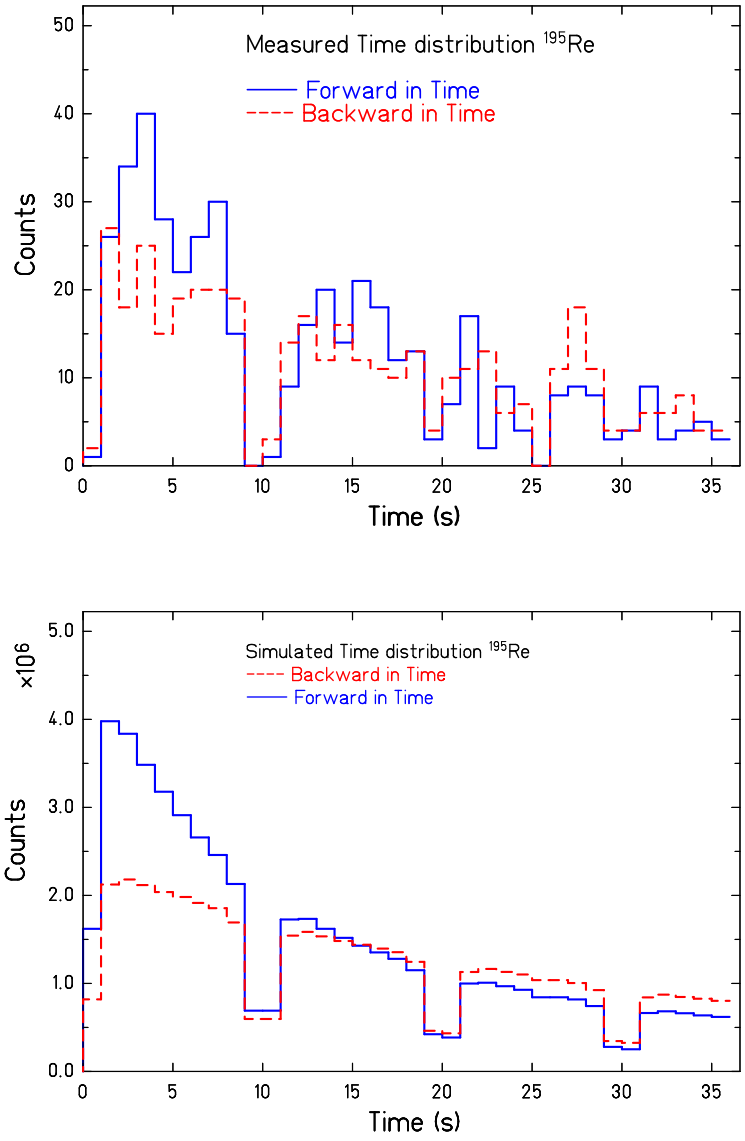

Figure 5.6: Measured implantation-β forward- and backward-time distributions for ^{195}Re for the time correlations performed only during the pause between beam pulses (top) and an example of the same distributions simulated with a Monte-Carlo code assuming $\tau = 9$ s and 30 % β-detection efficiency (bottom).

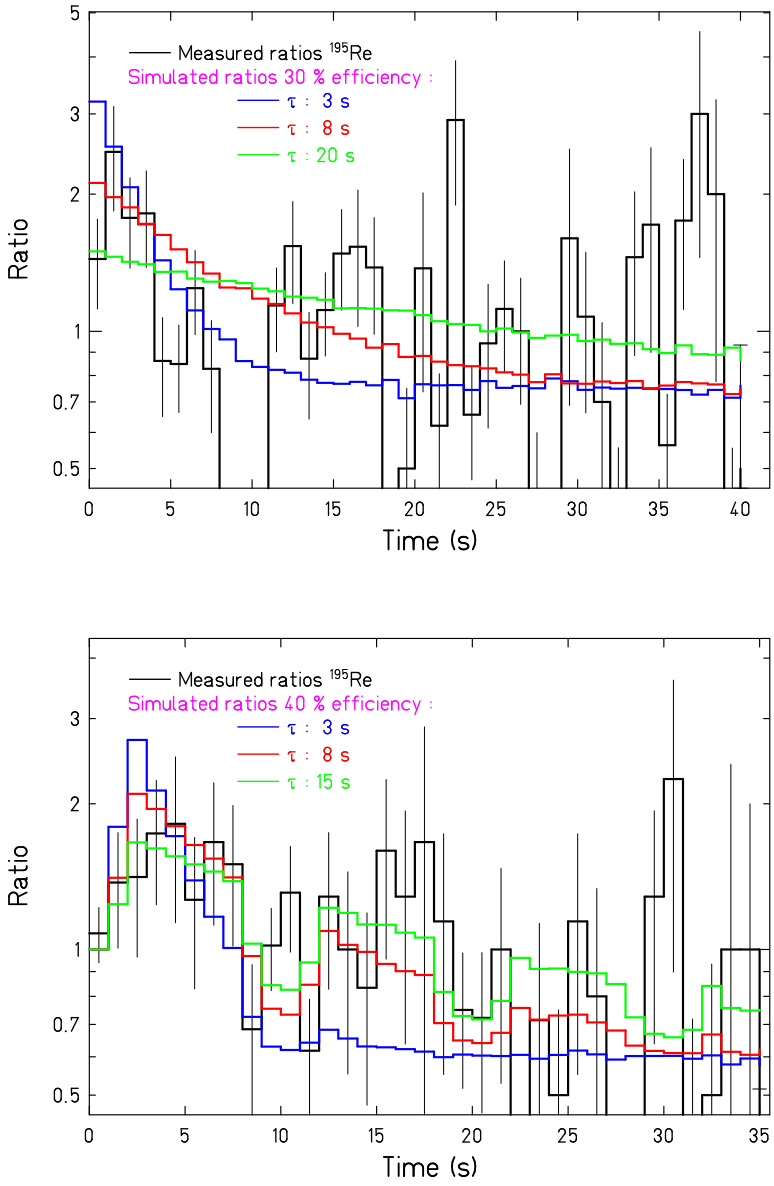

Figure 5.7: top: Ratios of the time-difference spectra between the first β-particle detected and the ^{195}Re implanted in the same strip during the pause between beam pulses, in forward- and backward-time and the corresponding Monte-Carlo simulated ratios for different lifetimes and an efficiency of 30 %. bottom: ratios of the time distribution using the full time structure compared with Monte-Carlo simulated ratios for different lifetimes and $\epsilon = 40\%$

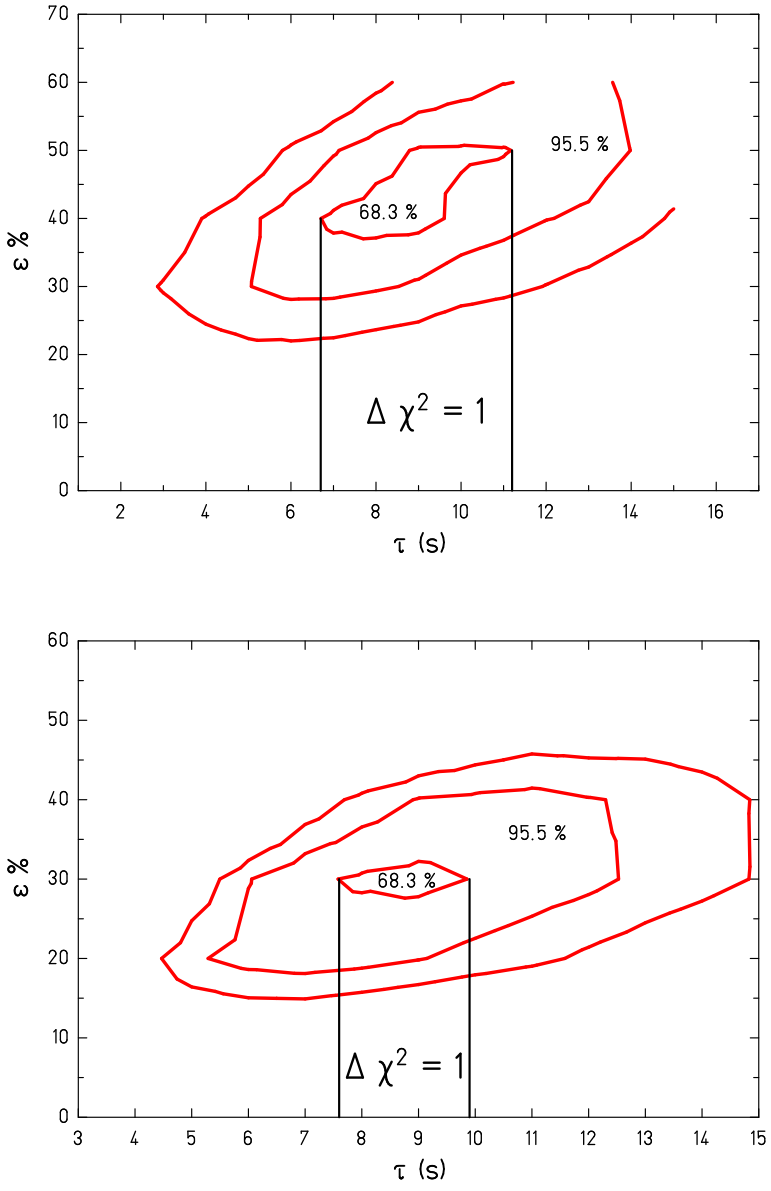

Figure 5.8: Top: χ^2 two-dimensional contour plot (lifetime-efficiency) obtained with our fitting procedure when considering the full time structure, spill and pause, and (bottom) the corresponding one for only the pause between spills.

In order to validate the proposed analysis method, we studied the ^{198}Ir nucleus which has a previously measured half-life of 8 s ± 3 s in Ref. [150] and 8 s ± 1 s in Ref. [151]. The minimum χ^2 of the fit for the ratio of the forward- and backward-time correlations corresponds to a $T_{1/2}$ = 8 s ± 2 s which is in perfect agreement with the previous measurement. The corresponding χ^2 distribution is shown in figure 5.9

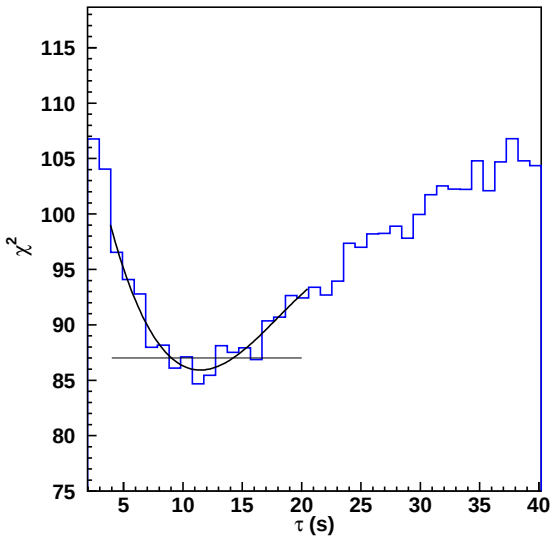

Figure 5.9: χ^2 projection into the lifetime coordinate for a 40 % detection efficiency for ^{198}Ir

In the next section we present the experimental results for all other nuclides.

5.4 Measured β half-lives

5.4.1 Results

Table 5.3 shows the resulting measured half-lives in this work. The reported values corresponds to the minimum of the reduced chi-squared χ^2_ν from the measured and simulated ratios of the forward and backward time correlations. The minimum χ^2_ν is reported in each case.

The average β-decay detection efficiency was $\epsilon \approx 30\%$. The uncertainty in the determination of ϵ is less than 10%.

The error bars correspond to statistical uncertainties, being one σ or $\Delta\chi^2 \leq 1$ in the contour plots of the variation of the χ^2 as a function of τ and ϵ, which corresponds to a 68% confidence interval. Since the nuclei under study are close to the stability, it is not necessary to include the daughter half-lives, since they are too long in comparison with those of the parent nuclei.

Table 5.3: *Experimental β-decay half-lives measured in this work from the analysis of the time correlations*

Nuclide	$T_{1/2}$ (s)	χ^2_ν
^{202}Ir	11^{+3}_{-3}	1.51
^{199}Ir	6^{+5}_{-4}	2.1
^{198}Ir	8^{+2}_{-2}	1.41
^{200}Os	6^{+4}_{-3}	0.7
^{199}Os	5^{+4}_{-2}	0.6
^{196}Re	3^{+1}_{-2}	1.11
^{195}Re	6^{+1}_{-1}	1.35
^{194}Re	$1^{+0.5}_{-0.5}$	1.29

5.4.2 Comparison with theoretical predictions and implications in astrophysics

The half-life calculations require knowledge of many features of the β-decay, as for instance quantum numbers of final states, the initial and final state nuclear configurations, Q_β and nuclear quadrupole deformations. However, this represents a challenge for heavy neutron-rich nuclei. Until now, these nuclei, especially those in the N = 126 region, have been far from any experimental access. Therefore, most of the information on their structure has been obtained through the extrapolation of experimentally derived measurements of stable nuclei.

There are essentially two different approaches to calculating the half-lives; the first being an early global macroscopic approximation called Gross Theory [144], and the second being the more recent approximations based on microscopic calculations.

The Gross Theory is formulated by the Japanese school and the first compilation of the half-lives was presented by Takahashi et al. [152]. This approximation does not consider the global properties of the nuclides. The β-strength is great in the statistically-distributed final states. The discrete sums over the final states are replaced by two integrals. The

shell effects are not considered, except in the mass predictions. A revised version of the Gross Theory has been presented by Tachibana et al [153], proposing numerous improvements while taking into account pairing, and uses a better description of the single-particle strength for the Gamow-Teller (GT) and first-forbidden transitions. We will use the half-lives from this improved calculation and the values are taken from the Ref. [144].

The microscopic approximation uses the quasi-particle random-phase approximation (QRPA). The two calculations performed in the $N \approx 126$ region, and $Z > 70$ are developed by P. Möller et al. [145] and I.N. Borzov et al. [146].

The Möller calculation is based on a macroscopic-microscopic finite-range droplet mass model (FRDM) [154] extended to include the contribution of the first-forbidden decays. The resulting FRDM-hybrid model [145] deals with the GT transitions within the random-phase approximation (RPA) and the first-forbidden transitions within the statistical Gross Theory framework.

The first self-consistent Hartree-Fock-BCS+continuum QRPA (CQRPA) model for the β-decay half-lives have been developed by I.N. Borzov in Ref. [155]. The self-consistent ETFSI+CQRPA approximation used calculate the ground state masses and weak-process rates has been elaborated in Ref. [156]. The density functional+CQRPA approximation, including the contribution of the GT and first-forbidden β-decays, has been recently dealt with in Ref. [147]. The half-lives that are used in the present study are calculated within the aforementioned approximation and are taken from Ref. [148].

The experimental values obtained in this work were systematically compared in figure 5.10 with the three theoretical models mentioned above, which predict half-lives in the region of the chart of nuclides corresponding to heavy neutron-rich nuclei around N = 126.

Generally, the calculations made within the Gross Theory framework overestimate the half-lives of the nuclides, except for those close to the shell closure, where the agreement is good, providing a general rough agreement with the experimental data.

The FRDM-hybrid RPA(GT) + FF(gr.th.) model by P. Möller fails in reproducing the measured half-lives by orders of magnitude, and this effect gets stronger as we approach the closed neutron shell. Far from the shell, in the region around $A \approx 195$ where deformation starts to become important, the agreement with the experimental data is quite reasonable. Since this model brings macroscopic corrections (for the first-forbidden transitions) to the original microscopic RPA model, it is hard to interpret the results obtained.

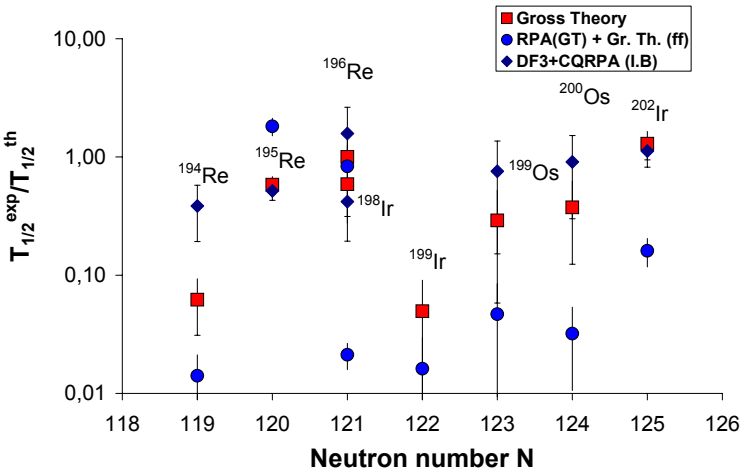

Figure 5.10: Ratios of experimental half-lives to theoretical calculations: from the revised Gross Theory calculations of Tachibana [144], the microscopic model of Möller using RPA [145] and the self-consistent CQRPA approach [148]

We found that, in general, DF3+CQRPA from Borzov seems to work better in reproducing the experimental data close to the shell. High-energy first-forbidden transitions reduce the total β-decay half-lives for the nuclei crossing the closed shells, and seems to be a key issue when describing β-decay close to N=126. The differences observed between the experimental half-lives and the model calculation for nuclei far from the closed-shell could be attributed to deformation effects. Indeed, nuclear deformation is an important input parameter for the QRPA calculations of Gamow-Teller (GT) strength function, and a 'wrong GT-decay pattern will ultimately result in a 'wrong half-life.

These comparisons show the necessity for measuring more half-lives of nuclides far from stability in order to test the validity of nuclear and β-decay models, and to provide a basis for choosing a reliable extrapolation. In fact, knowledge of half-lives of neutron-rich nuclei far from stability is required for r-process calculations.

Local maxima in the solar abundances are related to the existence of waiting-points around A = 80, 130 and 195. In those regions, the neutron

shell closures provide a limit to the r-process. Predictions of half-lives of isotopes close to the waiting-points are of importance in order to reproduce the relative yields and elemental composition in the waiting-point peak abundances.

In the case of A = 195 waiting-point, near Z ≈ 60-80, the role of the first-forbidden decays is decisive, since these nuclei undergo high-energy first-forbidden decays related to the $\nu 1i_{13/3} \rightarrow \pi 1h_{11/2}$ configuration [157]. The data from our experiment agrees with the I.N. Borzov model which predicts shorter half-lives than the other calculations. If these results are confirmed, this would imply an acceleration of the matter flow through this 'waiting-point', both in canonical r-process scenario and in the neutrino wind model, which in turn would radically change the overall picture regarding the r-process.

Chapter 6

Conclusions and Outlook

The results shown in this work represent a first step towards the study of heavy neutron-rich nuclei approaching the r-process waiting point at A=195. The progress relies on the implantation of projectile-like reaction products obtained by cold fragmentation in an active stopper.

In the present work we were able to synthesise and measure with high accuracy the production cross-sections of more than 190 heavy neutron-rich residues, 25 of which were produced for the first time. This data were used to benchmark the predictive power of different models.

It has been shown that semi-empirical parameterisations, such as EPAX, fail to describe the production of very neutron-rich nuclei. The present data may then be used to improve those parameterisations.

However, calculations based on the abrasion-ablation model present a much better predictive power. These calculations confirm that the production of neutron-rich nuclei in projectile fragmentation reactions are due to large fluctuations in both N/Z and excitation energy in the first stage of the collision.

A new technique has been developed to measure the β-decay half-lives of exotic nuclei in complex background conditions, using position and time correlations between the implantation of the fragment and the subsequent β-decay. Due to the specific experimental conditions of this technique, conventional analysis tools, based on analytical time-distribution functions could not be applied. Therefore, a new analysis procedure has been developed to extract the β-decay half-lives of the exotic nuclei, and its success has been demonstrated.

Monte-Carlo simulations of time correlations between implantations and β-like events allow us to evaluate and disentangle the background from the real events. This new method copes with the complex time structure present in the time-interval distributions of the fragment-β correlations due

to the periodic operation cycles of the heavy-ion synchrotron, providing the primary beam. We have shown that this time structure of the secondary beams can be used directly without losses due to additional beam suppression. The new method is generally suited to analyse experimental time distributions which are modulated with periodic source variations. When using adapted conditions, mostly beam intensities and purification of secondary beams, half-lives can be determined for a wide region of the chart of nuclides.

A correct understanding of the nuclear structure in the N=126 shell closure and mass region around A = 195 is of particular importance due to its relevance in the r-process modelling. The β-decay half-lives predicted within the DF3+CQRPA framework are in better agreement with experimental $T_{1/2}$ measured data than the RPA (GT)+ff(Gr.Th.) and Gross Theory results. For heavy r-process relevant nuclei, the first-forbidden transitions are expected to play an important role. The good agreement between the measured $T_{1/2}$ and the DF3+CQRPA calculations near the closed shell, accounting for the allowed and the first-forbidden transitions, seems to confirm the effect of the first-forbidden transitions in the N=126 region. The shorter half-lives predicted and measured in the present work would imply an acceleration of the matter flow through the A=195 'waiting-point', which in turn radically changes the overall picture regarding the r-process in this region.

Systematic comparisons of the measured $T_{1/2}$ with theoretical predictions can be used to resolve uncertainties in the models themselves, and uncertainties in the input parameters such of Q_β and deformations.

This work has shown that the N=126 region far below the doubly magic ^{208}Pb has become accessible experimentally. Experiments including $\beta - \gamma$ coincidences will be performed in the near future within the RISING [158] Collaboration, which will not only allow us to measure half-lives with greater precision, but will also allow us to obtain information on the nuclear structure of these heavy neutron-rich nuclei.

In a few years the new FAIR [41] facility will offer a tremendous potential for further investigations of the r-process path around the waiting point A = 195, by using the cold-fragmentation reaction mechanism, which will allow us to extend the limits of the chart of nuclides in the region of heavy neutron-rich nuclei, provided that enough primary beam-intensity is available.

Appendix A

Measured cross-sections in the reaction $^{208}Pb + Be$ at 1 A GeV

The production cross-sections measured in the experiment are summarised. The corresponding absolute errors (values include both statistical and systematical uncertainties), are indicated.

Table A.1: Production cross-sections (in mb) measured in the reaction $^{208}Pb(1 \cdot AGeV + Be)$. The absolute errors include statistical and systematical uncertainties.

Atomic number	Neutron number	σ (mb)	$\Delta\sigma$ (mb)
83	125	0.230E+00	0.609E-01
83	124	0.140E+01	0.297E+00
83	123	0.250E+01	0.620E+00
83	122	0.520E+01	0.135E+01
82	125	0.140E+03	0.253E+02
82	124	0.620E+02	0.112E+02
82	123	0.400E+02	0.724E+01
82	122	0.300E+02	0.543E+01
82	121	0.240E+02	0.434E+01
81	126	0.210E+02	0.380E+01
81	125	0.180E+02	0.333E+01
81	123	0.180E+02	0.326E+01
81	122	0.130E+02	0.269E+01
81	121	0.170E+02	0.308E+01
81	120	0.170E+02	0.308E+01
81	119	0.150E+02	0.311E+01
80	126	0.530E+00	0.959E-01
80	125	0.120E+01	0.251E+00
80	124	0.230E+01	0.481E+00
80	122	0.300E+01	0.627E+00
80	121	0.510E+01	0.928E+00
80	120	0.640E+01	0.116E+01
80	119	0.710E+01	0.129E+01
80	118	0.850E+01	0.176E+01
80	117	0.870E+01	0.183E+01
79	126	0.120E-01	0.216E-02
79	125	0.800E-01	0.144E-01
79	124	0.160E+00	0.291E-01
79	123	0.400E+00	0.844E-01
79	122	0.640E+00	0.136E+00
79	121	0.930E+00	0.224E+00
79	120	0.130E+01	0.246E+00
79	119	0.190E+01	0.350E+00
79	118	0.270E+01	0.624E+00
79	117	0.380E+01	0.722E+00
79	116	0.470E+01	0.973E+00
79	115	0.500E+01	0.905E+00
79	114	0.560E+01	0.105E+01
79	113	0.690E+01	0.125E+01
79	112	0.670E+01	0.139E+01

Atomic number	Neutron number	σ (mb)	$\Delta\sigma$ (mb)
78	126	0.270E-03	0.621E-04
78	125	0.250E-02	0.517E-03
78	124	0.110E-01	0.228E-02
78	123	0.270E-01	0.559E-02
78	122	0.890E-01	0.165E-01
78	121	0.140E+00	0.255E-01
78	120	0.260E+00	0.621E-01
78	119	0.490E+00	0.118E+00
78	118	0.760E+00	0.160E+00
78	117	0.920E+00	0.167E+00
78	116	0.140E+01	0.294E+00
78	115	0.180E+01	0.374E+00
78	114	0.240E+01	0.499E+00
78	113	0.280E+01	0.599E+00
78	112	0.350E+01	0.749E+00
78	111	0.340E+01	0.615E+00
78	110	0.410E+01	0.849E+00
77	126	0.390E-05	0.103E-05
77	125	0.590E-04	0.124E-04
77	124	0.560E-03	0.116E-03
77	123	0.170E-02	0.352E-03
77	122	0.290E-02	0.528E-03
77	121	0.560E-02	0.298E-02
77	120	0.370E-01	0.707E-02
77	119	0.580E-01	0.125E-01
77	118	0.920E-01	0.233E-01
77	117	0.160E+00	0.309E-01
77	116	0.270E+00	0.581E-01
77	115	0.380E+00	0.703E-01
77	114	0.600E+00	0.125E+00
77	113	0.900E+00	0.189E+00
77	112	0.110E+01	0.200E+00
77	111	0.160E+01	0.291E+00
77	110	0.210E+01	0.382E+00
77	109	0.270E+01	0.562E+00
76	124	0.160E-04	0.349E-05
76	123	0.470E-04	0.978E-05
76	122	0.210E-03	0.454E-04
76	121	0.660E-03	0.139E-03
76	120	0.210E-02	0.399E-03
76	119	0.480E-02	0.113E-02
76	118	0.150E-01	0.304E-02

Atomic number	Neutron number	σ (mb)	$\Delta\sigma$ (mb)
76	117	0.270E-01	0.578E-02
76	116	0.500E-01	0.111E-01
76	115	0.120E+00	0.251E-01
76	114	0.170E+00	0.321E-01
76	113	0.240E+00	0.470E-01
76	112	0.390E+00	0.733E-01
76	111	0.610E+00	0.116E+00
76	110	0.820E+00	0.148E+00
76	109	0.100E+01	0.182E+00
76	108	0.150E+01	0.297E+00
76	107	0.180E+01	0.374E+00
75	123	0.500E-05	0.112E-05
75	122	0.280E-04	0.532E-05
75	121	0.900E-04	0.165E-04
75	120	0.240E-03	0.454E-04
75	119	0.450E-03	0.936E-04
75	118	0.130E-02	0.246E-03
75	117	0.380E-02	0.726E-03
75	116	0.760E-02	0.178E-02
75	115	0.180E-01	0.436E-02
75	114	0.330E-01	0.865E-02
75	113	0.470E-01	0.104E-01
75	112	0.840E-01	0.185E-01
75	111	0.160E+00	0.408E-01
75	110	0.280E+00	0.647E-01
75	109	0.410E+00	0.799E-01
75	108	0.600E+00	0.113E+00
75	107	0.850E+00	0.163E+00
74	121	0.320E-05	0.110E-05
74	120	0.150E-04	0.360E-05
74	119	0.420E-04	0.903E-05
74	118	0.100E-03	0.191E-04
74	117	0.210E-03	0.445E-04
74	116	0.630E-03	0.152E-03
74	115	0.210E-02	0.504E-03
74	114	0.520E-02	0.103E-02
74	113	0.100E-01	0.211E-02
74	112	0.170E-01	0.362E-02
74	111	0.290E-01	0.612E-02
74	110	0.480E-01	0.917E-02
74	109	0.800E-01	0.171E-01

Atomic number	Neutron number	σ (mb)	$\Delta\sigma$ (mb)
74	108	0.130E+00	0.270E-01
74	107	0.210E+00	0.460E-01
74	106	0.310E+00	0.921E-01
74	105	0.480E+00	0.907E-01
74	104	0.750E+00	0.141E+00
73	119	0.400E-05	0.936E-06
73	118	0.160E-04	0.322E-05
73	117	0.480E-04	0.941E-05
73	116	0.100E-03	0.220E-04
73	115	0.270E-03	0.570E-04
73	114	0.600E-03	0.121E-03
73	113	0.130E-02	0.299E-03
73	112	0.400E-02	0.836E-03
73	111	0.690E-02	0.128E-02
73	110	0.150E-01	0.277E-02
73	109	0.250E-01	0.472E-02
73	108	0.430E-01	0.916E-02
73	107	0.620E-01	0.112E-01
73	106	0.960E-01	0.174E-01
73	105	0.190E+00	0.344E-01
73	104	0.310E+00	0.567E-01
73	103	0.466E+00	0.965E-01
72	118	0.130E-05	0.368E-06
72	117	0.380E-05	0.840E-06
72	116	0.990E-05	0.211E-05
72	115	0.310E-04	0.679E-05
72	114	0.730E-04	0.202E-04
72	113	0.220E-03	0.803E-04
72	112	0.450E-03	0.131E-03
72	111	0.780E-03	0.187E-03
72	110	0.220E-02	0.543E-03
72	109	0.500E-02	0.975E-03
72	108	0.920E-02	0.171E-02
72	107	0.210E-01	0.386E-02
72	106	0.340E-01	0.629E-02
72	105	0.570E-01	0.141E-01
72	104	0.970E-01	0.176E-01
72	103	0.160E+00	0.290E-01
72	102	0.300E+00	0.543E-01
71	115	0.290E-05	0.696E-06
71	114	0.690E-05	0.166E-05

Atomic number	Neutron number	σ (mb)	$\Delta\sigma$ (mb)
71	113	0.190E-04	0.435E-05
71	112	0.410E-04	0.105E-04
71	111	0.110E-03	0.277E-04
71	110	0.270E-03	0.116E-03
71	109	0.680E-03	0.174E-03
71	108	0.150E-02	0.414E-03
71	107	0.300E-02	0.666E-03
71	106	0.480E-02	0.103E-02
71	105	0.860E-02	0.181E-02
71	104	0.150E-01	0.322E-02
71	103	0.220E-01	0.462E-02
71	102	0.420E-01	0.874E-02
71	101	0.640E-01	0.132E-01
71	100	0.990E-01	0.205E-01
71	99	0.190E+00	0.393E-01
70	112	0.360E-05	0.756E-06
70	111	0.130E-04	0.265E-05
70	110	0.410E-04	0.849E-05
70	109	0.790E-04	0.163E-04
70	108	0.170E-03	0.604E-04
70	107	0.330E-03	0.116E-03
70	106	0.870E-03	0.233E-03
70	105	0.190E-02	0.429E-03
70	104	0.320E-02	0.710E-03
70	103	0.580E-02	0.133E-02
70	102	0.170E-01	0.357E-02
70	101	0.320E-01	0.666E-02
70	100	0.550E-01	0.114E-01

Appendix B

List of layers in the experiment

The thickness of the layers of matter that define the different detectors, targets and strippers of the FRS are listed in table B.

Table B.1: *List of the layers of matter used in the experiment*

Place	Layer	Material	Thickness (mg/cm^2)
TA	SIS window	Ti	4.5
	SEETRAM	Al	8.9
	Target 1	Be	1023
	Target 2	Be	2526
	Stripper	Nb	221
F2	Plastic scintillator SC2	Al	594.4
	Degrader 1-1	Al	4447
	Degrader 1-2	Al	5331
	Degrader 2-1	Al	4553
	Degrader 2-2	Al	3688
	Stripper	Nb	108
F4	MW41	Al	165
	Vacuum window	Ti	90.2
	Music 1	Al	98.5
	Stripper	Nb	222.8
	Music 2	Al	98.5
	MW42	Al	35.1
	Plastic scintillator SC4	Al	594.4
	Degrader 1	Al	3752
	Degrader 2	Al	3818
	Degrader 3	Al	3253
	Degrader 4	Al	4259
	Degrader 5	Al	3664
	Music 3	Al	300.7
	Plastic scintillator SC5	Al	283.3
	Active stopper	Ti	22.6
		Si	231.6
		Ti	22.6
	Air (35 cm)	Al	31.9
	Plastic scintillator SC6	Al	425

Appendix C

Beam-line setup at F2

The nuclei produced in the target cross different layers of matter, which correspond to the different detectors and stripper foils placed along the FRS. The location of these detectors at the intermediate focal plane F2 are shown in figure C.1.

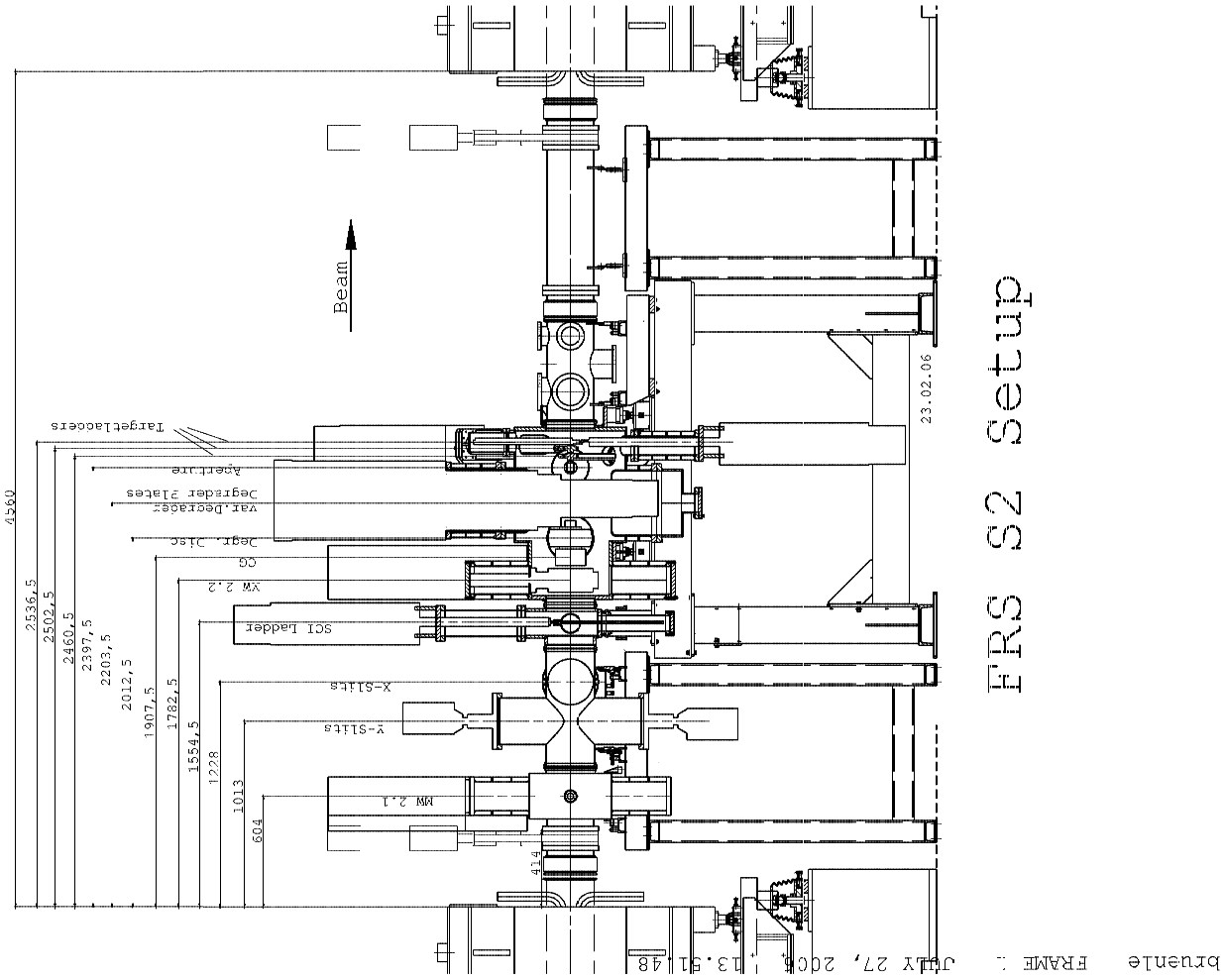

Figure C.1: Technical drawing of the FRS beam-line at the intermediate focal plane F2. The arrows indicate the relative distances (in mm) between the different detectors.

Appendix D

Beam-line setup at F4

Beam-line particle identification detectors corresponding to the implantation experimental setup at F4. Behind the MW41, also where the vacuum ends, two MUSIC ionisation chambers were placed. A stripper foil (not displayed) was placed between them. The MUSIC2 was followed by MW42 and a scintillator SC41. For the implantation experiment an homogeneous degrader was placed behind SC41. The Munich MUSIC was followed by a scintillator SC42 and the Si stack active stopper. At the end, a scintillator SC43 was placed, which serves as veto of the implantation in the active stopper.

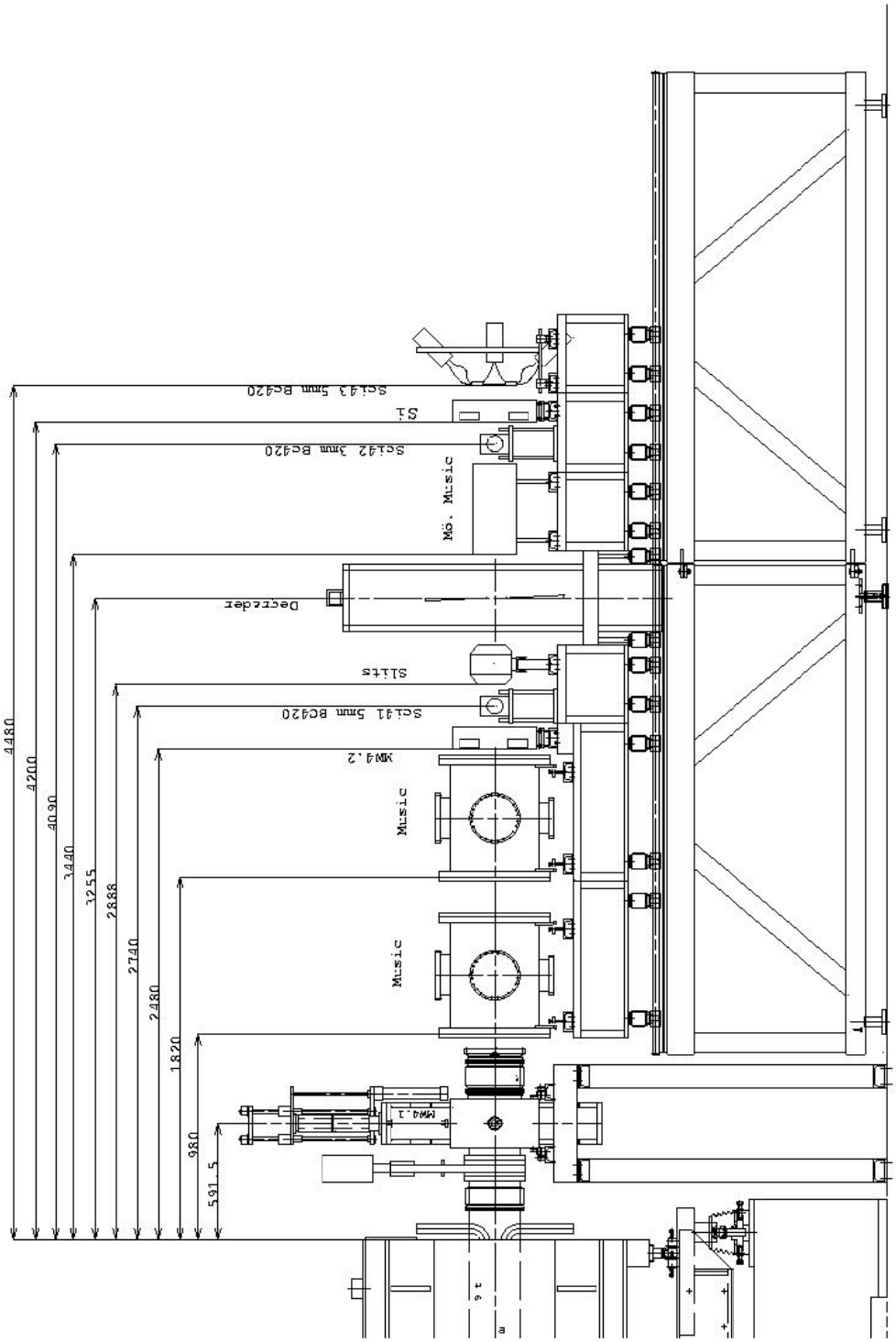

Figure D.1: Technical drawing of the FRS beam-line at the final focal plane F4. The arrows indicate the relative distances (in mm) between the different detectors.

Appendix E

DSSD electronics

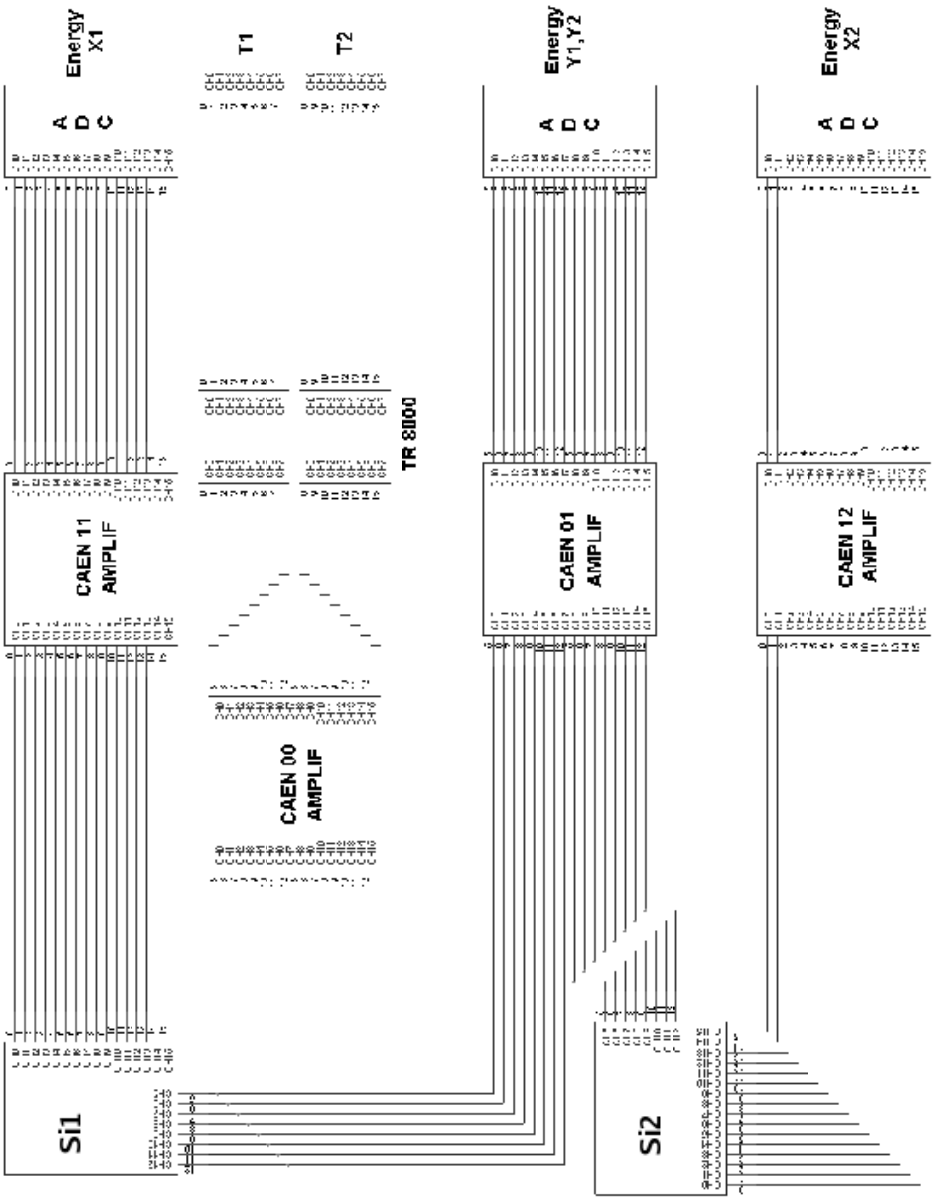

Figure E.1: Diagram of the electronics of Si1 Si2. Adapted from Ref. [138].

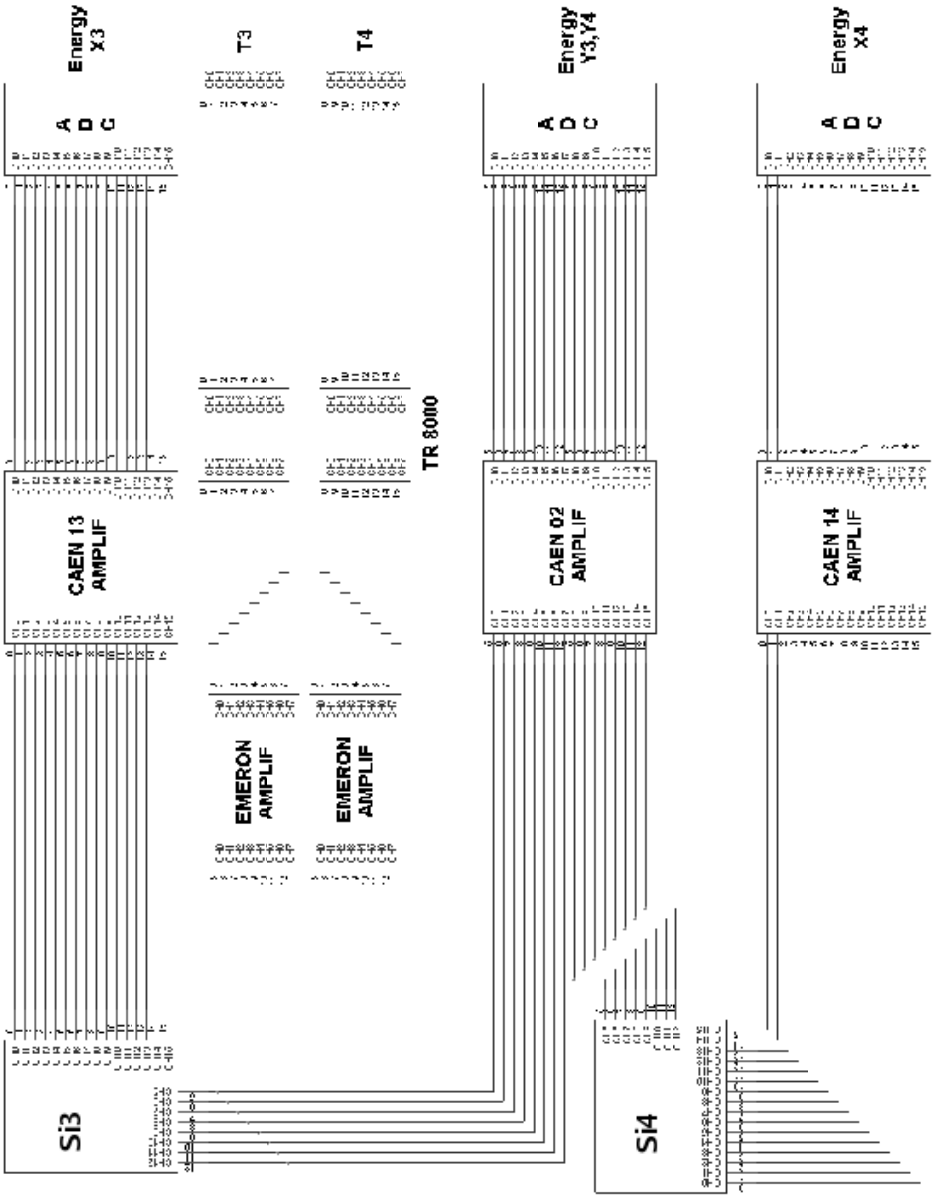

Figure E.2: Diagram of the electronics of Si3 and Si4. Adapted from Ref. [138].

Appendix F

β efficiency

The β efficiency ϵ is defined as the correlation efficiency, that is, the efficiency in the detection and the recording of a β decay. A good estimation of ϵ is needed, since an error in ϵ will affect the measurement of the half-lives.

In order to gain a gross idea of the expected values for ϵ, we used a GEANT4 [159] simulation of a DSSD. In this simulation monoenergetic β particles [160] are randomly generated, and the geometry of one DSSD pixel is defined. The β particles are randomly distributed in 4π. The position of the β emitter can be adjusted so that we can simulate the β efficiency for different implantation depths.

Figure F.1 summarises the results of the simulation of a 1.55 x 1.55 mm^2 pixel of 1 mm thick, with β particles emitted, with energies up-to 5 MeV, from the middle of the detector, z = 0.0 mm, (dots) and β particles emitted from the surface of the detector, z = 0.5 mm , that is, side-implantation (triangles). The corresponding β efficiencies are calculated using different energy thresholds.

A more realistic simulation was performed using the β spectrum shape estimated by the Fermi Theory of β-decay [161], instead of using a uniform distribution of monoenergetic electrons(see figure F.2). Since β^- emission is a three-body process, the total Q_β value for the reaction is equally shared between the daughter nucleus, β^-particle, and neutrino. This results in a β particle energy spectrum that extends from zero to the Q_β value (minus a small amount of energy for the mass of the neutrino and the nuclear recoil). For the decays in the present study, the Q_β values are typically around 4 MeV.

The corresponding β efficiencies calculated using different energy thresholds are summarised in table F.1

Considering the calibrated energy thresholds of the active stopper

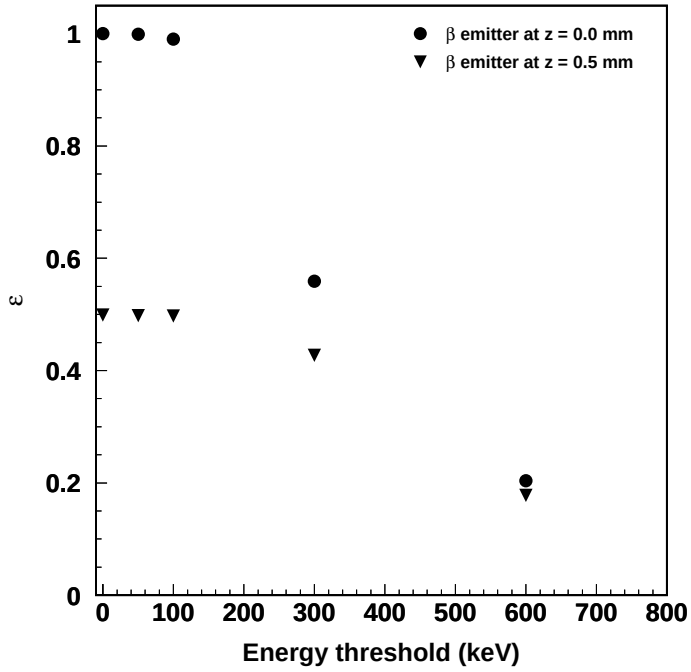

Figure F.1: Efficiency as a function of the energy threshold, for different implantation depths z = 0.0 mm and z = 0.5 mm

summarised in table 4.2, we would expect an average detection efficiency that ranges between 30% and 50%. The actual values of ϵ for each one of the nuclei to be analysed are determined by the simultaneous two-parameter fit (lifetime τ and efficiency ϵ), of the time correlations between the implantantion and the subsequent β decay. This procedure is described in chapter 5.

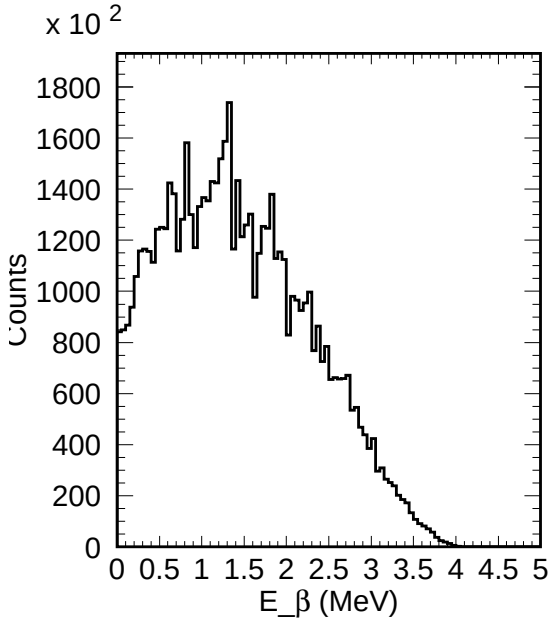

Figure F.2: Fermi Distribution for β-decay Energy for $Q_\beta = 4$ MeV

Table F.1: *β detection efficiency*

Z (mm)	β efficiency ϵ (%) by energy threshold			
	0 keV	50 keV	100 keV	300 keV
0.0	100.0	99.9	98.0	55.9
0.5	49.2	48.9	48.7	45.5

Resumen en castellano

1. Introducción.

Uno de los grandes retos de la astrofísica nuclear moderna, consiste en explicar los procesos que dan origen a la producción de materia y energía en el Universo, y en particular, de los procesos que conducen a la formación de elementos químicos, a través del proceso de nucleosíntesis.

Entre los datos más importantes de los que se dispone actualmente, se encuentran las abundancias conocidas de los elementos químicos en las estrellas, las nebulosas y en la propia tierra, pues estos valores, imponen determinadas restricciones, sobre los mecanismos a través de los cuales se ha producido la nucleosíntesis (ver figura F.1).

En los primeros momentos del Universo, bajo condiciones extremas, en que toda la materia se encontraba en estado de plasma, tuvieron lugar las reacciones de fusión de protones y neutrones, que produjeron elementos cada vez más pesados.

La fusión en el centro de las estrellas, se produce cuando la densidad y temperatura, que proviene de la presión gravitacional, son suficientemente altas. Existen varios ciclos de fusión, que ocurren en diferentes fases de la vida de una estrella . La primera etapa, es la fusión del Hidrógeno en Helio (cadena protón-protón [163]). Esta es la etapa en que se encuentra nuestro Sol.

En las estrellas de muy alta temperatura (temperaturas mayores de 16 millones de Kelvin), pueden ocurrir otros tipos de reacciones de fusión, como el llamado Carbono-Nitrógeno-Oxígeno, el ciclo (CNO) [163]. Aquí el átomo del Carbono es un catalizador para la reacción: participa pero no se "quema". A temperaturas aún mayores, el Helio que se quema produce Carbono. Finalmente, a temperaturas extremadamente altas, los elementos más pesados, como el Hierro, se forman por la fusión del Carbono, Oxígeno y Silicio.

En núcleos más pesados que el Hierro, la repulsión de Coulomb entre los nucleones, domina sobre las fuerzas nucleares, y no permite la agregación

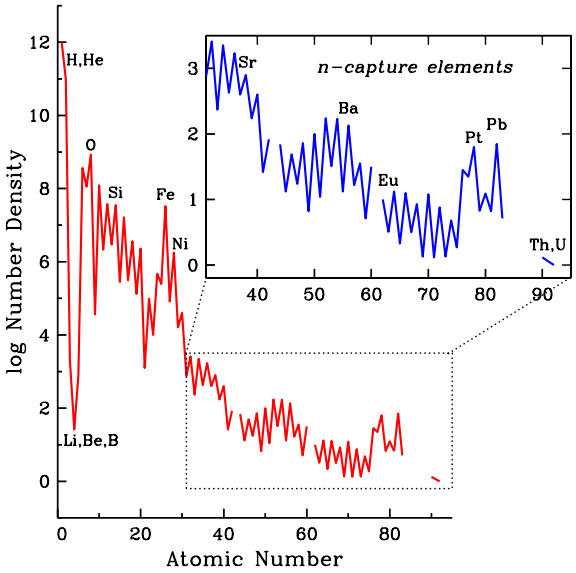

Figure F.1: *Curva de abundancias de elementos en el sistema solar. La figura principal muestra todos los elementos, mientras que el recuadro esta restringido a los elementos producidos por captura neutrónica, definidos aqui como aquellos elementos con* $Z > 30$. *Figura tomada de [162].*

de más protones, a menos de que se suministre energía. La manera de seguir creando elementos más pesados, es por medio de la captura de neutrones, ya que éstos no tienen carga, y por tanto, no estan afectados por la barrera Coulombiana. Una vez que un neutrón es incorporado a un núcleo, puede transformarse en protón mediante la desintegración β, emitiendo un electrón y un neutrino, y de esta manera, seguir formando núcleos con mayores números atomicos.

En particular, se cree, que determinados escenarios estelares, como explosiones de Supernova tipo II y estrellas de neutrones, dan lugar a la producción de núcleos pesados (con número másico superior a 60), mediante reacciones de captura de neutrones. En algunas estrellas, la captura de neutrones tiene lugar de forma tan rápida, que dan lugar a la producción de núcleos pesados ricos en neutrones. Este proceso es conocido como proceso de captura rápida de neutrones, o proceso-r [1]. Las curvas de abundancias del proceso-r observadas, muestran picos entorno a los números másicos A = 80, 130 y 195, los cuales estan relacionados con la existencia de capas cerradas de neutrones ("números mágicos") N = 50, 82 y 126, modelo propuesto por M. Goeppert-Mayer y J. Jensen

[164].

La física de las explosiones de supernova y formación de estrellas de neutrones, está intimamente ligada al comportamiento de la materia nuclear, bajo condiciones extremas. Actualmente se cree que los neutrinos juegan un importante papel en el mecanismo del colapso de una supernova. Durante la implosión, una ráfaga de neutrinos atraviesa la estrella, y una cantidad masiva de neutrones es producida, contribuyendo a la formación de elementos radiactivos.

Los núcleos extremadamente ricos en neutrones, que se producen en el proceso-r, se encuentran relativamente lejos del valle de la estabilidad (la región donde la relación entre el número de protones y de neutrones, hace a estos sistemas estables, en cuanto a la emisión de partículas, ver figura F.2). Trabajos teóricos recientes sobre la desintegración β de los núcleos que se encuentran lejos de la estabilidad, han puesto de relieve el papel del espaciado de los niveles energéticos altamente excitados en el núcleo hijo [147]. La vida media de la desintegración β, es muy sensible a esta cantidad, siendo ésta un ingrediente crucial, para calcular la producción de elementos pesados en supernovas y estrellas de neutrones.

El estudio experimental de núcleos pesados ricos en neutrones, en la región donde se produce el proceso-r, es fundamental para entender el mencionado proceso de nucleosíntesis estelar, y para comprobar las diferentes teorías a partir de las cuales, se derivan las propiedades nucleares de los isótopos lejos de la estabilidad [10].

Durante los últimos años, se han obtenido resultados experimentales prometedores, en el estudio de las propiedades de núcleos ricos en neutrones de masa intermedia, cercanos al punto de espera o 'waiting point' alrededor de N = 82 [13], sin embargo, la región próxima a N = 126 permanece inexplorada [15]. La fisión ha sido usada con éxito, para producir isótopos ricos en neutrones de masa intermedia [166], mientras que los actuales límites de la carta de núcleos, en la región de núcleos pesados ricos en neutrones, permanece cercana a la estabilidad. Sin embargo, recientemente, las reacciones de fragmentación fría inducidas por proyectiles relativistas, han sido propuestas [16] como un mecanismo de reacción óptimo, para producir núcleos pesados ricos en neutrones.

Asimismo, son necesarias predicciones fiables de las distribuciones de intensidad de desintegración β, para el cálculo de las vidas medias, así como para los procesos retardados β (como la emisión de partículas o la fisión retardada β). La distribución de la intensidad, depende de la estructura microscópica de las funciones de onda nucleares, inicial y final, así como de la interacción que media la desintegración. De este modo, se precisa de una descripción consistente del estado fundamental

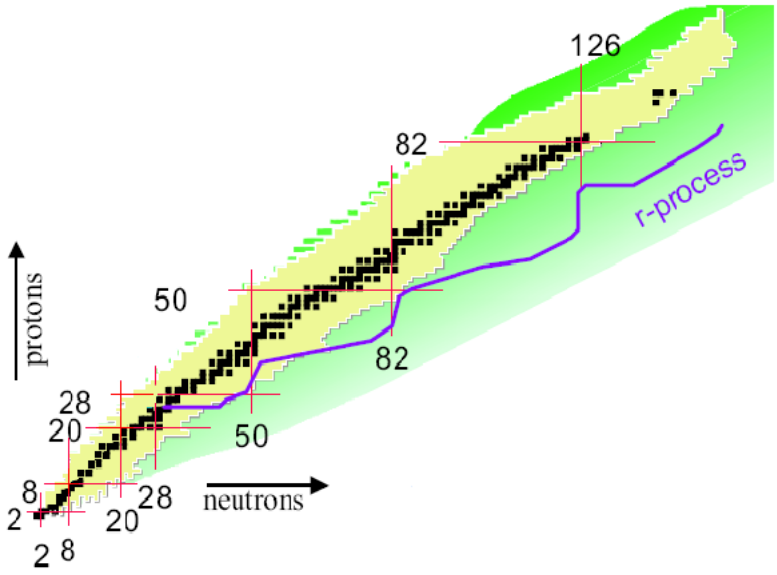

Figure F.2: *Carta de núcleos, mostrando los núcleos conocidos hasta ahora. El valle de la estabilidad esta indicado en negro. La región en amarillo indica los núcleos inestables producidos y estudiados en el laboratorio. La región en verde indica los núcleos inestables que aun no han sido explorados. Las lineas rojas verticales y horizontales muestran los números mágicos, reflejando las regiones donde se espera que los núcleos estan más ligados y tienen vidas medias más largas. La línea púrpura indica una posible ruta del proceso r de nucleosíntesis estelar. Figura adaptada de [165].*

del núcleo madre, y de los estados poblados del núcleo hijo, para obtener de forma fiable la intensidad β. Al mismo tiempo, si las distribuciones de intensidad obtenidas teóricamente, no se corresponden con el experimento, eso indicaría la necesidad de mejorar el formalismo teórico empleado.

En la presente tesis doctoral, se propone estudiar experimentalmente, la desintegración β de algunos de los núcleos, que son producidos en el proceso-r de nucleosíntesis estelar. En particular, se quieren estudiar isótopos de Iridio, Osmio y Renio, con un exceso de neutrones más allá de los límites actuales de los núcleos conocidos. El gran exceso de neutrones de estos núcleos, constituye la principal dificultad de su estudio. Estos núcleos son inestables, y por tanto hay que producirlos en el laboratorio, utilizando reacciones nucleares entre iones pesados. Además, para medir su

vida media, debemos recurrir a una técnica experimental ingeniosa, capaz de producir e identificar en vuelo estos núcleos, y estudiar su desintegración β. La complejidad de estos experimentos hace necesaria la participación de varios grupos de investigación. En concreto, el presente estudio experimental se ha realizado en colaboración con diferentes institutos europeos: GSI, Alemania, IPN-Orsay, GANIL, CENBG-Bordeaux, Francia y la Universidad de Santiago de Compostela, España.

2. Técnica experimental

Para producir núcleos pesados ricos en neutrones, se utilizan reacciones de fragmentación fría [16] inducidas por proyectiles de Plomo, con una energía de 208 GeV sobre un blanco de Berilio. El objetivo de estas reacciones es arrancarle al núcleo proyectil (Plomo), el mayor número posible de protones, sin que éste pierda neutrones. De esta forma se producen núcleos residuales con un gran exceso de neutrones. El uso de un haz de ^{208}Pb permite producir núcleos pesados ricos en neutrones a lo largo de la capa cerrada de neutrones N =126.

Estos experimentos pueden realizarse en las instalaciones del Gesellschaft für Schwerionenforschung mbH (GSI), ubicado en Darmstadt, Alemania, donde su acelerador de iones pesados SIS [19], nos permite acelerar núcleos de Plomo, hasta una energía de 1 $A \cdot GeV$.

La detección e identificación de los núcleos producidos se realiza en vuelo, utilizando el separador de fragmentos FRS [17] del GSI. Este separador es un espectrómetro de gran resolución, de más de 70 m de longitud, con cuatro dipolos como elementos ópticos principales, que permite identificar en vuelo, la relación carga/masa de núcleos a alta energía, por medio de la medida de la rigidez magnética, tiempo de vuelo y pérdida de energía de cada fragmento que atraviesa el FRS, según la ecuación

$$\frac{A}{Z} = \frac{e}{u}\frac{B\rho}{\beta\gamma c} \tag{F.1}$$

donde A es el número másico, Z es el número atómico, B es el campo magnético dentro del imán, ρ es el radio de la trayectoria, u es la unidad atómica de masa, e es la carga del electrón, $\gamma = (1-\beta^2)^{1/2}$ con $\beta = v/c$, donde v es la velocidad del ión, determindada a partir del tiempo de vuelo y c es la velocidad de la luz.

Una de las dificultades principales, a la hora de trabajar con iones pesados en este régimen de energías, es que no se presentan completamente ionizados, y la distribución de sus estados iónicos cambia al atravesar un

material. La posibilidad de identificar sin ambigüedad cada núcleo, suceso a suceso, fue posible mediante el uso de un bloque de aluminio (*degrader*), situado en la trayectoria de vuelo de las partículas dentro el espectrómetro. La selección en rigidez magnética que induce ese sistema, junto con la medida adicional de pérdida de energía que supone su presencia, permiten identificar los estados de carga dentro del espectrómetro.

Para determinar el número atómico, mediante cámaras de ionización, surge la misma dificultad. La combinación de la medida con dos cámaras independientes y los resultados obtenidos con el *degrader*, nos permite diferenciar, todas las combinaciones de estados de carga posibles. De ese modo, la identificación es completa.

La técnica experimental permite determinar las secciones eficaces de producción, mediante la medida de la tasa de producción de cada núcleo, normalizada a la intensidad del haz incidente y el número de átomos por unidad de área en el blanco, el cual viene dado por

$$N_t = N_o \frac{T_{blanco}}{A} \tag{F.2}$$

donde N_o es el número de Avogadro, T_{blanco} es el espesor del blanco, en unidades de mg/cm^2 y A es el número másico. Para monitorizar el haz, se empleó una cámara denominada SEETRAM [111] (SEcondary Electron TRAnsmission Monitor), interpuesta en su trayectoria, que por la emisión electrónica inducida por el flujo de partículas, permite determinar la intensidad del haz.

Una vez producidos los núcleos de interés, se estudia su desintegración β, y en particular su período de desintegración. Para ello, se hace uso de un dispositivo experimental, capaz de frenar los núcleos ricos en neutrones que hemos producido a energías relativistas, y a su vez, capaz de identificar la posterior emisión de una partícula β, y medir el tiempo transcurrido entre la implantación y la desintegración del núcleo.

Este dispositivo consta de un sistema de láminas de aluminio de espesor variable, que permite frenar los núcleos que se han producido hasta energías del orden de las decenas de MeV. Adicionalmente se utiliza una matríz de cuatro detectores de silicio (*Double Side Silicon Strip Detectors, DSSD*), cada uno de ellos con 16 pistas en ambas caras, separadas por una distancia de 3.12 mm, en los cuales se implantan los núcleos de tal forma que la posterior emisión del β queda registrada por los detectores.

3. Resultados y discusión

Identificación isotópica y secciones eficaces

En la figura F.3, se muestra la matríz de identificación de los isótopos medidos en dos configuraciones diferentes del FRS, centrados en ^{194}W y ^{186}Lu, con un tiempo de adquisición de 2h 41' y 11h 45' respectivamente. Las líneas en la figura representan los límites actuales de la carta de núcleos. En la figura cada *cluster* o cúmulo representa un núcleo. La alta resolución obtenida, está claramente representada en la figura, lo cual ha permitido identificar, sin ambigüedad, los diferentes núcleos producidos en el experimento.

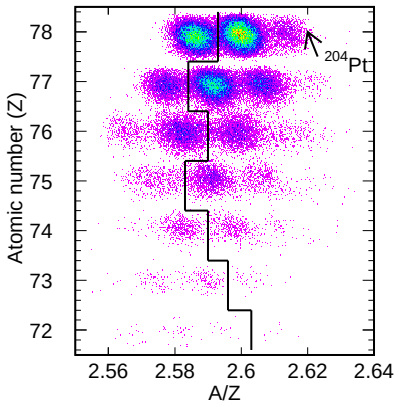

Figure F.3: *Matríz de identificación, Z en función de A/Z medido en la reacción $^{208}Pb + Be$ a 1 $A \cdot GeV$. Los datos corresponden a dos configuraciones del FRS, centrados en ^{194}W y ^{186}Lu. Las líneas representan los límites actuales de la carta de núcleos.*

En el presente trabajo, se han medido secciones eficaces de producción de más de 190 isótopos ricos en neutrones, de elementos desde el Plomo hasta el Iterbio (ver figura F.4). Para ello hubo que normalizar los contajes observados para cada núcleo, a la intensidad del haz primario y espesor del blanco de producción. Posteriormente se han realizado una serie de correcciones, transmisión, reacciones secundarias y estados de carga, necesarias para la obtención de los resultados con una alta precisión. Estas medidas han permitido identificar por primera vez 25 nuevos isótopos ricos en neutrones, cercanos a la capa cerrada N = 126, extendiendo así los límites actuales de la carta de núcleos.

En la figura F.5, se muestran las distribuciones isotópicas de producción

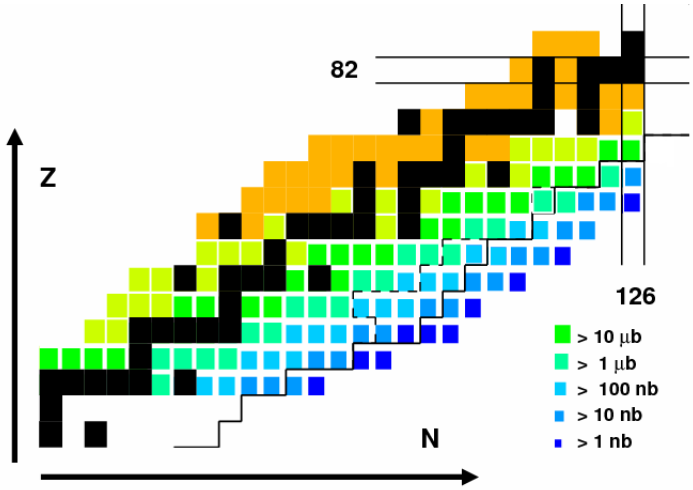

Figure F.4: *Carta de núcleos sobre la que se representan, las secciones eficaces medidas. Más de 190 núcleos ricos en neutrones han sido medidos en la reacción ^{208}Pb (1 A GeV) + Be. La línea sólida corresponde a los límites actuales de la carta de núcleos y la línea discontinua a los límites de las vidas medias conocidas.*

de todos los elementos. Como puede observarse, secciones eficaces de producción por debajo del nano barn, pueden medirse en una semana de tiempo de haz. La calidad de estos datos, nos permite realizar estudios comparativos con diferentes cálculos, que describen la producción residual en colisiones de iones relativistas.

La línea discontinua en la figura F.5, representa los cálculos obtenidos usando la fórmula semi-empírica EPAX v.2 [47]. Como puede observarse, este cálculo no reproduce adecuadamente nuestros datos. En particular, las secciones eficaces correspondientes a los núcleos más ricos en neutrones, están sobreestimadas por más de un orden de magnitud. Una mejor descripción de los datos experimentales, se obtiene a partir de los cálculos obtenidos, usando el código COFRA [16]. Este código es una formulación analítica del modelo de abrasión-ablación [48], donde la primera etapa de la reacción, lleva a la formación de un pre-fragmento, cuyo tamaño depende del parámetro de impacto. La energía de excitación depende del número de nucleones involucarados en el proceso de *abrasión*. Después de la termalización, el pre-fragmento se desexcita mediante la evaporación de nucleones, llevando a un núcleo residual final. La adecuada descripción de los datos de este modelo confirma, que los canales de reacción, que

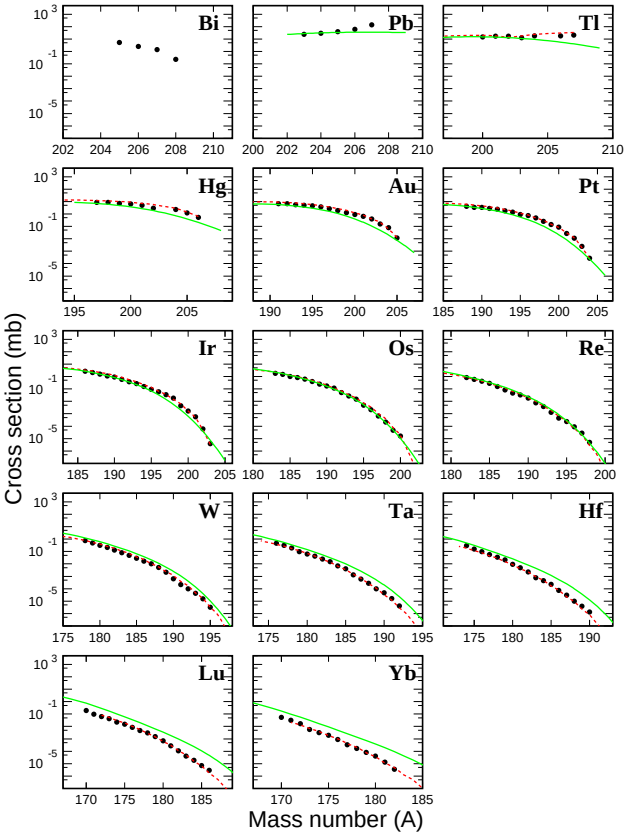

Figure F.5: *Secciones eficaces isotópicas de los fragmentos producidos en la reacción ^{208}Pb (1 A GeV) + Be medidos en este experimento, comparadas con los cálculos de producción residual, la parametrización EPAX [47] (línea sólida) y el código COFRA [16] (línea discontinua).*

permiten la producción de los núcleos más ricos en neutrones, es debida a la gran fluctuación tanto en N/Z como en la energía de excitación del pre-fragmento. Estas fluctuaciones hacen posible que con cierta probabilidad, se arranquen sólo protones del proyectil, introduciendo una pequeña energía de excitación. Este particular canal de reacción, denominado *fragmentación fría*, permite la producción de los residuos más ricos en neutrones, en las reacciones de fragmentación del proyectil.

Vidas medias de desintegración β

Una vez producidos los núcleos de interés, se estudia su desintegración β, y en particular, su período de desintegración. Las vidas medias, se determinan a partir de las correlaciones en posición y tiempo, entre los fragmentos implantados en el detector de Si (*active stopper*), y la posterior emisión del β.

Los espectros de correlaciones temporales fragmento-β, son el resultado de la superposición de dos componentes:

- las correlaciones temporales producto de la desintegración β del fragmento seleccionado

- y un fondo, producto de las correlaciones aleatorias de las emisiones β, de otras especies previamente implantadas, y electrones atómicos, estando este fondo influenciado por la distribución cíclica del haz incidente.

La clave del análisis de las correlaciones temporales, está en separar el fondo de los eventos reales. A fin de evaluar el fondo, se obtiene la forma de los eventos 'no correlacionados', evaluando la diferencia de tiempo entre una implantación dada y un β emitido en un tiempo anterior, esto es, haciendo las correlaciones fragmento-β, en una secuencia de tiempo inversa. Esta nueva correlación, representa el fondo de eventos aleatorios, no debidos a correlaciones temporales inducidas por la desintegración β del núcleo estudiado.

El cociente entre las correlaciones temporales 'hacia adelante' y 'hacia atrás', contiene la información de las correlaciones 'verdaderas'. Sin embargo, las vidas medias de densitegración β, no pueden determinarse a partir de los métodos analíticos estándar, debido a la compleja estructura de las correlaciones temporales. A fin de interpretar estos espectros, se desarrolló un código Monte-Carlo, que simula correlaciones de tiempo entre implantaciones y detección de electrones, bajo las condiciones experimentales encontradas en el FRS, esto es: secuencia de ciclo del haz, tasa de implantación de fragmentos y frecuencia de detección de electrones, durante el pulso del haz y en la pausa, dejando libres dos parámetros: el período de desintegración β (τ) y la eficiencia de detección de electrones (ϵ). Las vidas medias de desintegración β, se obtienen a partir de los cocientes de los espectros de correlaciones temporales, 'hacia adelante' y 'hacia atrás', medidos y simulados, aplicando el método de mínimos cuadrados.

La figura F.6, muestra la comparación entre los resultados experimentales, correspondientes a las vidas medias de 8 isótopos ricos en neutrones

del Iridio, Osmio y Renio, sintetizados en el presente trabajo, y tres cálculos teóricos disponibles en la literatura, para núcleos pesados ricos en neutrones, cercanos a la capa cerrada N=126 y $Z > 70$, a saber: el cálculo paramétrico *Gross Theory* [144] desarrollado por Tachibana y colaboradores, el modelo microscópico de P. Möller y colaboradores [145] basado en RPA para el cálculo de las transiciones Gamow-Teller y Gross Theory para el cálculo de las transiciones prohibidas (*first-forbidden*), y el modelo de I. N. Borzov [147, 148], basado en la aproximación de funcional de densidad y QRPA, incluyendo las transiciones Gamow-Teller y las transiciones prohibidas en forma auto-consistente. En general, se observa que el modelo de I. N. Borzov ofrece una mejor descripción de los datos experimentales, que el resto de los modelos disponibles, y que la introducción de las transiciones prohibidas, es un punto clave, para la correcta descripción de la desintegración β cerca de la capa cerrada N = 126.

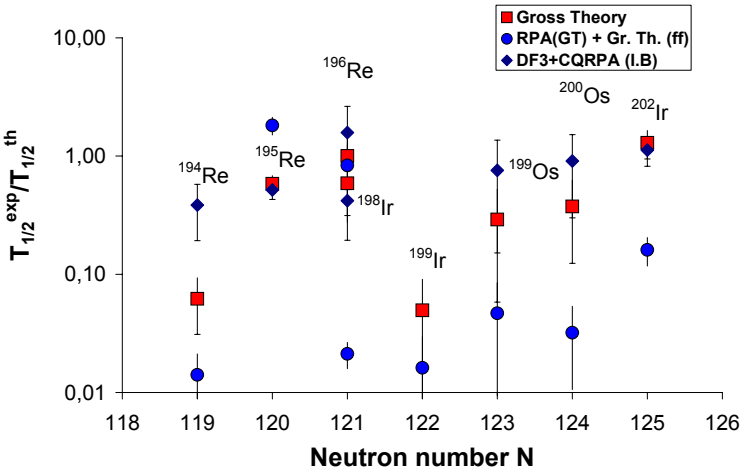

Figure F.6: Cocientes entre las vidas medias experimentales y cálculos teóricos correspondientes a la Gross Theory de Tachibana, el modelo microscópico de Möller y cálculo auto-consistente QRPA de Borzov.

4. Conclusiones

Los resultados mostrados en este trabajo, representan un primer paso, en el estudio de núcleos pesados ricos en neutrones, próximos al punto de espera del proceso-r entorno a A =195.

A partir de este estudio, se han podido extraer importantes conclusiones, acerca de la producción de núcleos pesados ricos en neutrones, habiéndose sintetizado por vez primera 25 isótopos ricos en neutrones, en la región $N \approx 126$.

Se han determinado las secciones eficaces de producción, de más de 190 núcleos pesados ricos en neutrones, en la reacción de framentación $^{208}Pb + Be$ a una energía de 1 $A \cdot GeV$. Se ha observado que la parametrización EPAX, no describe adecuadamente los datos experimentales, correspondientes a los núcleos más ricos en neutrones. Sin embargo, cálculos basados en el modelo de abrasión-ablación, presentan un poder predictivo mucho mayor. Estos cálculos confirman, que la producción de núcleos ricos en neutrones, en reacciones de fragmentación del proyectil, son debidas a grandes fluctuaciones tanto en N/Z, como en la energía de excitación, en la primera etapa de la colisión.

Se ha desarrollado una nueva técnica, para medir vidas medias de desintegración β, en condiciones de fondo muy complejas, que ha permitido obtener la vida media de 8 isótopos ricos en neutrones, entorno a la capa cerrada N =126.

Al comparar los resultados experimentales del presente trabajo, con los cálculos macroscópicos de Gross Theory y cálculos microscópicos realizados por P. Möller y I.N. Borzov, se observa, que el cálculo desarrollado por este último, en general, está en mejor acuerdo con nuestros resultados experimentales, ya que las vidas medias, calculadas en este modelo, son considerablemente más cortas, que las del resto de predicciones disponibles en la literatura, para esta región de la carta de núcleos.

El acortamiento de las vidas medias, para núcleos cercanos a N =126, observado en el presente trabajo de tesis doctoral, implica una aceleración del flujo de materia en el punto de espera A =195, lo cual puede modificar la visión actual del proceso-r, tanto en el escenario canónico [167], como en el de viento de neutrinos [30], abriendo una puerta para investigaciones futuras.

Próximamente se realizarán nuevos experimentos, incluyendo coincidencias $\beta-\gamma$ dentro de la colaboración RISING [158], que permitirán obterner información espectroscópica, de los núcleos cercanos a la capa cerrada N=126. En los próximos años, el nuevo complejo de aceleradores FAIR [41], ofrecerá un enorme potencial para investigar los núcleos involucrados en

el proceso-r de nucleosíntesis estelar, en la región de núcleos pesados, en torno al punto de espera A =195.

Resumen en Gallego

Esta tese de doutoramento, representa un primeiro paso, no estudo de núcleos pesados ricos en neutróns, próximos ao punto de espera do proceso-r de nucleosíntese estelar, arredor de A =195. O gran exceso de neutróns dos núcleos implicados, constitúe a principal dificultade do seu estudo. Estes núcleos son inestables, e polo tanto hai que producilos no laboratorio, utilizando reaccións nucleares entre ións pesados. Ademais, para medir a súa vida media, debemos recorrer a unha técnica experimental inxeniosa, capaz de producir e identificar en voo estes núcleos, e estudar a súa desintegración. A complexidade destes experimentos fai necesaria a participación de varios grupos de investigación. En concreto, este estudo experimental realizouse en colaboración con diferentes institutos europeos: GSI, Alemania, IPN-Orsay, GANIL, CENBG-Bordeaux, Francia e a Universidade de Santiago de Compostela, España. A partires deste estudo, poidéronse extraer importantes conclusións, sobre a produción de núcleos pesados ricos en neutróns, téndose sintetizado por primeira vez 25 isótopos ricos en neutróns, na rexión N 126. Determináronse as seccións eficaces de produción, de máis de 190 núcleos pesados ricos en neutróns, na reacción de framentación 208Pb + Be a unha enerxía de 1 A GeV. Desenvolveuse unha nova técnica para medir vidas medias de desintegración, en condicións de fondo moi complexas, que permitiron obter a vida media de 8 isótopos ricos en neutróns, arredor da capa pechada N =126. Ao comparar os resultados experimentais deste traballo, cos cálculos macroscópicos de Gross Theory e cálculos microscópicos RPA (GT)+ff(gr.th) e DF3+CQRPA, obsérvase, que o cálculo DF3+CQRPA, en xeral, está en mellor acordo cos nosos resultados experimentais, xa que as vidas medias, calculadas neste modelo, son considerablemente máis curtas, que as do resto de predicións dispoñibles na literatura, para esta rexión da carta de núcleos. O acurtamento das vidas medias, para núcleos próximos a N =126, observado neste traballo de tese de doutoramento, implica unha aceleración do fluxo de materia no punto de espera A =195, o cal pode modificar a visión actual do proceso-r,

tanto no escenario canónico, como no de vento de neutrinos, abrindo unha porta para investigacións futuras. Proximamente realizaranse novos experimentos, incluíndo coincidencias beta-gamma que permitirán obter información espectroscópica, dos núcleos próximos á capa pechada N=126. Nos vindeiros anos, o novo complexo de aceleradores FAIR, en Darmstadt, Alemania, ofrecerá un enorme potencial para investigar os núcleos implicados no proceso-r de nucleosíntese estelar, na rexión de núcleos pesados, arredor do punto de espera A =195.

Bibliography

[1] E. M. Burbidge, G. R. Burbidge, W. A. Fowler and F. Hoyle. Rev. Mod. Phys. **29** (1957) 547

[2] A. G. W. Cameron. Atomic Energy of Canada, Ltd., CRL-41 (1957)

[3] S. E. Woosley and R. D. Hoffman. Astrophys. J. **395** (1992) 202

[4] B. S. Meyer et al. Astrophys. J. **399** (1992) 656

[5] K. Takahashi et al. Astrom. Astrophys. **286** (1994) 857

[6] S. E. Woosley et al. Astrophys. J. **433** (1994) 229

[7] Y.-Z. Qian. Astrophys. J. **534** (2000) L67

[8] E. Symbalisty and D. N. Schramm. Astrophys. Lett. **22** (1982) 143

[9] C. Freiburghaus, S. Rosswog and F.-K. Thielemann. ApJ **525** (1999) L121

[10] K. Langanke and G. Martinez Pinedo, Rev. Mod. Phys. **75** (2003) 819.

[11] E. Lund et al. Phys. Scr. **34** (1986) 614

[12] R. L. Gill et al. Phys. Rev. Lett. **56** (1986) 1874

[13] K.-L Kratz et al., Z. Phys. A **325** (1986) 489

[14] F. K. Thielemann et al. Nucl. Phys. A **570** (1994) 329c

[15] B. Pfeiffer et al., Nucl. Phys. A **693** (2001) 282

[16] J. Benlliure et al., Nucl. Phys. A **660** (1999) 87

[17] H. Geissel *et al*; Nucl. Instr. Meth. B **70** (1992) 286

[18] K.-H. Schmidt, E. Hanelt, H. Geissel, G. Münzenberg, J.-P. Dufour Nucl. Instr. Meth. A **260** (1987) 287

[19] K. Blasche, SIS beam development, 1989-91, GSI report GSI-INT-/86-2

[20] H. E. Suess and H. C. Urey. Rev. Mod. Phys. **28** (1956) 53

[21] J. J. Cowan and C. Sneden, Nature, **440** (2006) 1151

[22] F. Käppeler et al. Rep. Prog. Phys. **52** (1989) 945

[23] J. J. Cowan, C. Sneden. Proceedings of the 3rd International Conference on Fission and Properties of Neturon-Rich Nuclei. eprint arXiv:astro-ph/0212149)

[24] K.-L. Kratz et al. Astrophys. J. **403** (1993) 216

[25] J. J. Cowan and F.-H. Thielemann, R-process nucleosynthesis in supernovae. Phys. Today 57,(2004) 47

[26] J. M. Pearson et al. Phys. Lett. B **387** (1996) 455

[27] Y. Aboussir et al., At. Data Nucl. Data Tables **61** (1995) 127

[28] J. J. Cowan and C. Sneden, in Carnegie Observatories Astrophysics Series, Vol. 4: Origin and Evolution of the Elements (ed. McWilliam, A. and Rauch, M.), 2742 (Cambridge Univ. Press,2004).

[29] C. Freiburghaus et al. Astrophys. J. **516** (1999) 381

[30] R. C. Duncan, S. L. Shapiro, and I. Wasserman, Astrophys. J. **309** (1986) 141

[31] Y.-Z. Qian et al. Phys. Rev. C **55** (1997) 1532

[32] S. Goriely et al. Nucl. Phys. A **758** (2005) 587c

[33] S. Goriely et al. Nucl. Phys. A **718** (2003) 287

[34] J. J. Cowan, F. -K. Thielemann and J. W. Truran. Phys. Rep. **208** (1991) 267

[35] F.-K. Thielemann et al. Proc. of the First Argone MSU/JINA/INT RIA workshop: The r-process: the astrophysical origen of the heavy elements and related rare isotope accelerator physics. World Scientific (2004). P. 1

[36] A. McWilliam et al. Astrom. J. **109** (1995) 2757

[37] A. McWilliam et al. Annu. Rev. Astrom. Astrophys. **35** (1997) 503

[38] C. Sneden el al. Astrophys. J. **533** (2000) L139

[39] J. W. Truran et al. in: A. Weiss et al (Eds.) First Stars, Springer, 2000, p. 142

[40] http://www.orau.org/ria/

[41] http://www.gsi.de/fair/index.html

[42] http://www.eurisol.org/

[43] J. Benlliure, K. Helariutta, K.-H. Schmidt and M.V.Ricciardi. Proceedings of the Third International Conference on Fission and Properties of Neutron-Rich Nuclei November 3-9, 2002, Sanibel Island, Florida, USA

[44] H. L. Rav Phil. Trans. R. Soc. Lond. A **356** (1998) 1955

[45] D. J. Morrisey and B. M. Sherrill. Phil. Trans. R. Soc. Lond. A **356** (1998) 1985

[46] R. Serber. Phys. Rev. **72** (1947) 1114

[47] K. Sümmerer and B. Blank. Phys. Rev. C **61** (2000) 034607

[48] J.-J. Gaimard, K.-H. Schmidt, Nucl. Phys. A 531 (1991) 709

[49] K. Sümmerer et al. Phys. Rev. C **42** (1990) 2546

[50] J. Benecke, T. T. Chou, C. N. Yang, and E. Yen. Phys. Rev. **188** (1969) 2159

[51] J. Hüfner, et al. Phys. Rev. C **12** (1975) 1888

[52] K. Helariutta, J. Benlliure, M. V. Ricciardi, K.-H. Schmidt. Eur. Phys. J. A **17** (2003) 181

[53] E. Fermi. Z. Phys. **88** (1934) 161

[54] K.S. Krane, Introductory Nuclear Physics. John Wiley and Sons, New York, 1988

[55] M. A. Preston. "Physics of the Nucleus". Addison-Wesley, 1962

[56] N. B. Gove and M. J. Martin. Nuc. Data Tables **10** (1971) 205

[57] C. L. Duke et al. Nucl. Phys. A **151** (1970) 609

[58] J. Damgaard, R. Broglia and C. Riedel. Nucl. Phys. A **135** (1969) 310

[59] P. Ring and P. Schuck. *The Nuclear Many-Bofy Problem*. Springer-Verlag (1980)

[60] K. Grotz and H. Klapdor. *The Weak Interaction in Nuclear Particle and Astrophysocs*. Bristol,Hilger (1990)

[61] B. Pfeiffer, K.-L. Kratz, and P. Möller. Progr. Nucl. Energ. **41** (2002) 39

[62] J. Engel. *The r-process: The Astrophysical Origin of the Heavy Elements*. Eds. Y.-Z. Quian et al. Proc. Inst. of Nucl. Theory, vol 13, Wold Scientific (2004)

[63] I. N. Borzov. Nucl. Phys. A **777** (2006) 645

[64] A. C. Graves and R. L. Walker. Phys. Rev. **71** (1947) 1

[65] S. W. Kitwanga et al. Phys. Rev. C **40** (1989) 35

[66] H. Geissel et al., Phys. Rev. Lett. **68** (1992) 3412

[67] M. Jung et al., Phys. Rev. Lett. **69** (1992) 2164

[68] F. Bosch et al., Phys.Rev. Lett. **77** (1996) 5190

[69] F. Attallah et al. Nucl. Phys. A **701** (2002) 561c

[70] T. Radon et al. Nucl. Phys. A **677** (2000) 75

[71] M. Haussman et al. Nucl. Instr. Meth. A **446** (2000) 569

[72] M. Haussman et al. Hyp. Int. **132** (2001) 291

[73] O. Kavatsyuk et al. Eur. Phys. J. A **25** (2005) 211

[74] B. Blank et al. Phys. Rev. C **69** (2004) 015502

[75] R. Borcea et al. Nucl. Phys. A **695** (2001) 17.

[76] H. De Witte et al. Phys. Rev. C **69** (2004) 044305

[77] I. Dillmann, K. L. Kratz, A. Wohr et al. Phys. Rev. Lett **91** (2003) 162503

[78] M. Oinonen et al. Phys. Lett. B **511** (2001) 145

[79] S. Dean, M. Gorska et al. Eur. Phys. J. A **21** (2004) 243

[80] G. C. Ball et al. Phys. Rev. Lett. **86** (2001) 1454

[81] M. Bernas, P. Ambruster, et al. Z. Phys. A. **336** (1990) 41

[82] M. Bernas, P. Ambruster et al. Phys. Rev. Lett **67** (1991) 3661

[83] M. J. Murphy et al. Phys. Rev. Lett. **49** (1982) 455

[84] S. Czajkowski et al. Z. Phys. A **348** (1994) 267

[85] F. Ameil et al. Eur. Phys. J. A **1** (1998) 275

[86] T. Faestermann et al. Eur. Phys. J. A **15** (2002) 185

[87] C. Mazzocchi et al. Eur. Phys. J. A **17** (2003) 519

[88] F. Montes et al. Phys. Rev. C **73** (2006) 035801

[89] P. T. Hosmer et al. Phys. Rev. Lett. **94** (2005) 112501

[90] S. N. Liddick, P. F. Mantica et al. Phys. Rev. Lett **92** (2004) 072502

[91] P. Mantica et al. Phys. Rev. C **67** (2003) 014311

[92] S. Grevy et al. Phys. Lett. B **594** (2004) 252

[93] S. Grevy et al. Nucl. Phys. A **746** (2004) 145c

[94] O. Sorlin et al. Eur. Phys. J. A. **16** (2003) 55

[95] M. Sawicka et al. Phys. Rev. C **68** (2003) 044304

[96] O. Sorlin et al. Nucl. Phys. A **669** (2000) 351

[97] O. Sorlin et al. Phys. Rev. C **47** (1993) 2941

[98] P. L. Reeder et al. Phys. Rev. C **44** (1991) 1435

[99] K. Yoneda et al. Phys. Rev. C **67** (2003) 014316

[100] R. V. F. Janssens et al. Phys. Lett. B **546** (2002) 55

[101] E. Roeckl . Nucl. Phys. A **704** (2002) 200c

[102] O. Sohler et al. Phys. Rev. C. **66** (2002) 054302

[103] Zs. Podolyak et al. Phys. Lett. B **491** (2000) 225

[104] K. H. Schmidt Eur. Phys. J. A **8** (2000) 141

[105] P. Bevington and D. K. Robinson. Data Reduction and Error Analysis for the Physical Sciences. McGraw-Hill, 1992

[106] H. Bartsch, K. Huber, U. Kneissl and H. Sattler. Nucl. Instr. Meth. **121** (1974) 185

[107] K. H. Schmidt et al. Z. Phys. A **316** (1984) 19

[108] M. Steiner et al., Nucl. Instr. Meth. A **312** (1992) 420

[109] http://www-aix.gsi.de/∼wolle/EB_at_GSI/FRS-WORKING/ACCELERATOR/IMAGES/accel_overview.gif

[110] R. Anne et al., Developement of Beam-Profile Monitors with Gas Amplification and Current Readout for the SIS Projectile-Fragment Separator, GSI Scientific Report (1990) 257

[111] C. Ziegler. Diploma Thesis, Institut f"ur Kernphysik, TH Darmstadt (1992)

[112] $http://www-win.gsi.de/charms/seetraminfo/manual.htm$

[113] http://www-w2k.gsi.de/charms/amadeus.htm

[114] J. Pereira. PhD Thesis. Universidad de Santiago de Compostela (2004)

[115] C. Schaerf et al., Nucl. Instr. Meth. 30 (1964) 359

[116] E. Grorud et al., Rapport LNS/029 (1979)

[117] G. Münzenberg. Nucl. Instr. Meth. B **70** (1992) 265

[118] E. Hanelt. Doktorarbeit, TH Darmstadt, GSI 92-05 (1992)

[119] S. Czajkowski. These Universite Paris VII (1992)

[120] B. Voss Diploma Thesis, Institut für Kernphysik, TH Darmstadt (1995)

[121] M. Pfützner et al. Nucl. Instr. Meth. B **86** (1994) 213

[122] http://www-linux.gsi.de/∼weick/frs/mwpc.html

[123] http://www-w2k.gsi.de/daq/

[124] http://cern.ch/paw/

[125] http://www-w2k.gsi.de/charms/SATAN/GHELP/satanhelp.htm

[126] E. Casarejos et al. Phys. Rev. C **74** (2006) 044612

[127] C. Scheidenberger et al. Nucl. Inst. Meth. B **142** (1998) 441

[128] P. J. Karol, Phys. Rev. C **11** (1975) 1203

[129] A. Kelic et al. Phys. Rev. C **70** (2004) 064608

[130] T. Enqvist et al., Nucl. Phys. A **686** (2001) 481

[131] M. de Jong et al., Nucl. Phys. A **628** (1998) 479

[132] J. Benlliure et al., Nucl. Phys. A **628** (1998) 458

[133] http://www.micronsemiconductor.co.uk/

[134] http://www.ganil.fr/gip/electronique/elec256si/256chansi.html

[135] http://www.caen.it/nuclear/product.php?mod=N568B

[136] http://www.caen.it/nuclear/product.php?mod=V785

[137] http://www-linux.gsi.de/∼mbs/v43/manual/gm_vme_trig.pdf

[138] M. Fermandez . DEA Thesis (2003)

[139] The European Physical Journal, Review of Particle Physics, **15** 1-4 (2000)

[140] H.Geissel et al., Nucl. Inst. Meth. A **282** (1989) 247

[141] http://dnr080.jinr.ru/LISE/lise.html

[142] http://www-wnt.gsi.de/charms/software.htm
http://www-wnt.gsi.de/charms/Codes/Betacorr/BETACORR-SOURCE.zip

[143] $http://wwwndc.tokai-sc.jaea.go.jp/CN04/index.html$

[144] T.Tachibana, M.Yamada, Proc. Int. Conf on exotic nuclei and atomic masses, Arles, 1995, p.763

[145] P. Möller, B. Pfeiffer and K.-L. Kratz. Phys. Rev. C 67 (2003) 055802

[146] I.N.Borzov , S. Goriely PEPAN 34 (6) (2003) 1376

[147] I. N. Borzov. Phys. Rev. C **67** (2003) 025802

[148] I.N. Borzov, Private communication

[149] R. Peierls . Proc. R. Soc. (London) A **149** (1935) 467

[150] A. Szalay and S. Uray. *Radiochim.Radioanal.Lett.*, **14** (1973) 135

[151] F.J.Schweden, N.Kaffrell BMBW-FBK-72-15 (1972) p.88

[152] K. Takahashi et al. Atomic Data Nucl. Data Tables **12** (1973) 101

[153] T. Tachibana et at. Atomic Data Nucl. Data Tables **39** (1988) 251

[154] P. Möller et al. Atomic Data Nucl. Data Tables **59** (1995) 185

[155] I. N. Borzov et al. Z. Phys. A **355** (1996) 117

[156] I.N. Borzov, S. Goriely and J. M. Pearson. Nucl Phys. A **621** (1997) 307c

[157] I. N. Borzov. Phys. Atom. Nucl. **67** (2004) 1696

[158] http://www-aix.gsi.de/∼wolle/EB_at_GSI/RISING/rising.htm

[159] http://geant4.web.cern.ch/geant4/

[160] A. Algora. Private communication

[161] R. D. Evans, The Atomic Nucleus, McGraw-Hill Book Company, 1955, p.548

[162] N. Grevesse and A. J. Sauval, Space Sci. Rev. **85** (1998) 161

[163] D. D. Clayton. *Principles os Stellar Evolution and Nucleosynthesis.* McGraw-Hill, 1968

[164] M. Goeppert-Mayer and J. Jensen, Elementary Theory of Nuclear Shell Structure (Wiley, New York, 1955)

[165] *http* : *//www.orau.org/ria/images/landscape.JPG*

[166] M. Bernas et al., Phys. LettB. **415** (1997) 111

[167] P.A. Seeger, W. A. Fowler and D. D. Clayton. ApJS **11** (1965) 121